ABSTRACT

Title of Dissertation:	MORPHOLOGY OF UNCONFINED AND CONFINED SWIRLING FLOWS UNDER NON-REACTING AND COMBUSTION CONDITIONS
	Sean Stacey Archer, Doctor of Philosophy, 2005
Dissertation Directed By:	Professor Ashwani K. Gupta Department of Mechanical Engineering

Swirl is used in practically all types of combustion systems, including gas turbine combustion, furnaces and boilers. In combustion systems, the strong favorable effect of swirl to combustion air and/or fuel has been extensively used for flame stabilization, high heat release per unit volume, and clean efficient combustion. Flow and combustion characteristics of non-reacting and reacting swirl flowfields are characterized using a simulated Lean Direct Injection (LDI) method in a double concentric swirl burner. The LDI scheme had a large number of small size holes for fuel injection to provide rapid fuel mixing into the surrounding combustion air. The double concentric burner allowed examination of radial distribution of swirl in the burner (co- and counter-flow) under unconfined and confined conditions, both without and with combustion. The input thermal loading to the burner was held constant at 33 kW for all flames.

Particle image velocimetry (PIV), optical emission spectroscopy (OES), infrared (IR) thermometry, gas analysis and computer compensated micro-

thermocouple measurements, were used for diagnostics. These diagnostics provided information on spatial and temporal distribution of flowfield, flame generated radicals, mean gas species concentration, and mean and rms temperatures compensated to high frequencies as well as the associated integral- and micro-thermal time scales, respectively.

Unconfined co-swirl flows had generally wider (except non-reacting) and longer internal recirculation zones, slower velocity decay, smaller reverse flow velocity, lower intensity of flame generated radicals, higher temperatures, and longer integral- and micro-thermal time scales as compared to its counter part. Confinement altered the global flame structure dramatically by rapid radial expansion of the flame to the combustor walls. It increased length and decreased width of the internal recirculation zone, delayed the velocity decay, increased temperatures, amplified intensity of flame generated radicals over a greater region, and enlarged turbulence levels. The vortical structures associated with the instantaneous flow for all cases revealed significant dynamical behavior in the flow as compared to the mean flow case. Infrared thermometry results supported the micro-thermocouple data on mean temperatures. The trend for NOx emissions was higher for the confined case in both co- and counter-swirl cases.

MORPHOLOGY OF UNCONFINED AND CONFINED SWIRLING FLOWS UNDER NON-REACTING AND COMBUSTION CONDITIONS

By

Sean Stacey Archer

Dissertation submitted to the Faculty of the Graduate School of the
University of Maryland, College Park, in partial fulfillment
of the requirements for the degree of
Doctor of Philosophy
2005

Advisory Committee:
Dr. Ashwani K. Gupta, Professor, Chair
Dr. Ken Yu, Assoc. Professor, Dean’s Representative
Dr. Horace L. Russell
Dr. Michael Ohadi, Professor
Dr. Bao Yang, Asst. Professor

Dedication

To my mother and grandparents

Acknowledgements

I would like to thank Dr. Ashwani K. Gupta for affording me this research opportunity. His knowledge and assistance was inspirational and instrumental in helping me improve the quality of this research. I also offer my sincere gratitude to Dr. Horace L. Russell for inviting and introducing me to this fine university and having faith in my abilities to succeed. Special thanks are due to Professor Daryll Pines, Professor Andre Marshall and Mr. Bryan Hill for all their helpful advice and friendship. I would like to thank the NASA Glenn Research Center, the Sloan Foundation, and GAANN fellowship for their financial support. I also would like to extend my gratitude to the NASA Glenn Research Center for the research experience provided me during the summer months in 2001 and 2002. This time afforded me the opportunity to interact with eminent researchers and to grow as a researcher. I would also like to thank my family and friends for supporting me and encouraging me. I would like to give a special thanks to my mother whom I always know I can turn to in my time of need. I also would like to acknowledge the support of my fellow University of Maryland Combustion Laboratory peers, Martin Linck, Mohammad Ghaderi, and especially Vivek Gautam for his invaluable assistance with developing experimental techniques. Last but not least, I would like to thank my Lord and Savior for giving me the strength I needed to finish this endeavor.

Table of Contents

List of Tables

List of Figures

Nomenclature

2-D	two dimensional
3-D	three dimensional
α	swirl vane angle
ε	emissivity
ε_s	shear strain rate
ν	frequency
ρ	fluid density
ρ_{air}	density of the air
ρ_{fuel}	density of fuel
σ	Stephan-Boltzmann constant ($1.38066 \cdot 10^{-23}$ J·K^{-1})
$\tau_{chemical}$	chemical time
τ_{mixing}	mixing time
Φ	equivalence ratio
A	area of the annulus
A	transition probability for the spontaneous emission
A_{bead}	thermocouple bead surface area
CCD	charge-coupled device
CFD	computational fluid dynamics
CO	carbon monoxide
CO_2	carbon dioxide
c_p	specific heat
d	nozzle diameter
DC	direct current
d_{eff}	effective diameter
d_h	hub diameter
D_{sw}	swirler diameter
E	upper level energy
$\dot{E}_{in}$	heat loading
FLIR	forward looking infrared radiometer
FPA	focal plane array
g	statistical weight of the excitation level
h	convective heat transfer coefficient
h	Planck's constant
HWA	hot wire anemometry
ICCD	intensified charge-coupled device
IDL	iterative data language
IDT	Integrated Design Tools
JP-4	jet propulsion fuel, type 4
k	Boltzmann's constant
LDI	lean direct injection
LDV	laser Doppler velocimetry
LHV	lower heating value
LPP	lean premixed prevaporized
m	bead mass

M	momentum ratio
M_φ	angular momentum flux
m_e	entrained mass flow rate
m_{sw}	swirler mass flow rate
M_x	axial momentum flux
MCP	micro-channel plate
N	number density
NO_X	nitrogen oxides
O2	oxygen
OES	optical emission spectroscopy
p	pressure
PIV	particle image velocimetry
PLIF	Planar Laser Induced Fluorescence
PMT	photomultiplier tube
psi	pounds per square inch
q_{conv}	convection heat transfer
q_{rad}	radiation
Q(T)	partition function
Q_{fuel}	fuel flow rate
QWIP	quantum well infrared photodetector
r	radius
R_0	characteristic length
RQL	rich-burn/quick-mix/lean-burn
S	swirl number
scfm	standard cubic feet per minute
T_b	bead temperature
T_{final}	measured final temperature
T_g	real gas temperature
$T_{initial}$	measured initial temperature
TKE	turbulent kinetic energy
T_s	surrounding temperature
u	axial component of the velocity
U_{flame}	flame speed
UHC	unburned hydrocarbons
U_{rms}	radial root mean square velocity/Reynolds radial normal stress
U_{supply}	reactant supply speed
u_t	tangential velocity
UV	ultra-violet
UV-NIR	ultra-violet near infrared
V	volume flow rate
V_{air}	velocity of the air
VOC's	volatile organic compounds
V_{rms}	axial root mean square velocity/Reynolds axial normal stress
w	tangential component of the velocity

W_{rms}	tangential root mean square velocity/Reynolds tangential normal stress

Chapter 1: Introduction

Some key issues in the development of non-reacting and reacting flow structure for gas turbine combustors are identified and investigated in this study. The conversion of fuel energy into a useful form of power is the main function of gas turbine engines. Presently, gas turbines are used in abundance for many of the worlds' power needs. These requirements range from aero-propulsion, land based power generation, marine power and propulsion, and automotive engines. With its myriad of uses, evolving demands for efficient power and increasingly stringent pollution regulations, gas turbine engines are a renewed and fertile research area. The development and continued improvement of the gas turbine engine into a reliable and versatile engine with a high power to weight ratio is demanding and extensive. In this present study, investigation in the area of gas turbine combustor research is conducted.

Some of the most complex flows within a gas turbine engine can be found in the combustor. As a result, design methods have historically been based largely on empiricism. Presently there has been a push for designs to lean heavily on computer models/simulations and 3-D computational fluid dynamics (CFD). These computer based models and simulations from the standpoint of cost and time are very feasible. For the full power of such models and simulations to be utilized, experimental data is needed so that the predictions of these computer based design tools are accurate. To help with the development of models and 3-D-CFD, experimental insight into flow physics and chemistry is needed to provide a basis for model development, comparison and validation.

The emissions from combustion are an item of interest during an investigation of the complex flows within a combustor. Emission of pollutants caused by combustion includes smoke (soot and other particulates), various volatile organic compounds (VOC's), harmful chemical compounds such as unburned hydrocarbons (UHC) and carbon monoxide (CO), and oxides of nitrogen and sulfur. These components have been found to be environmentally detrimental in numerous ways. Carbon monoxide is a poisonous gas that can be harmful in very low quantities. Although considered more of a byproduct of combustion than a pollutant, carbon dioxide has been classed as a "Greenhouse Gas" and is considered to be at least partly responsible for global warming. Sulfur and nitrogen oxides cause an increase in the acidity of rain in regions downwind of the emission source. This "acid rain" damages vegetation and leaches into lakes and drinking water sources. Additionally, nitrogen oxides are believed to be responsible for visible smog and the depletion of the ozone layer. Gas turbines are a significant source of the production of NO_X because of their wide variety of applications. Over ninety percent of all man-made nitrogen oxides that enter the atmosphere are produced by combustion of various fuels [1]. Primarily, there are three different ways in which the major component of Nitric oxide can be formed. First, at high temperature zones found in flames, N_2 reacts with oxygen to form thermal NO (called thermal NO_x). Secondly, when the fuel has nitrogen-containing compounds, the nitrogen is released at comparatively low temperatures and forms NO_x (called fuel NO_x). And lastly, reactions of fuel-derived radicals with N_2 ultimately lead to NO (called Prompt NO_x)

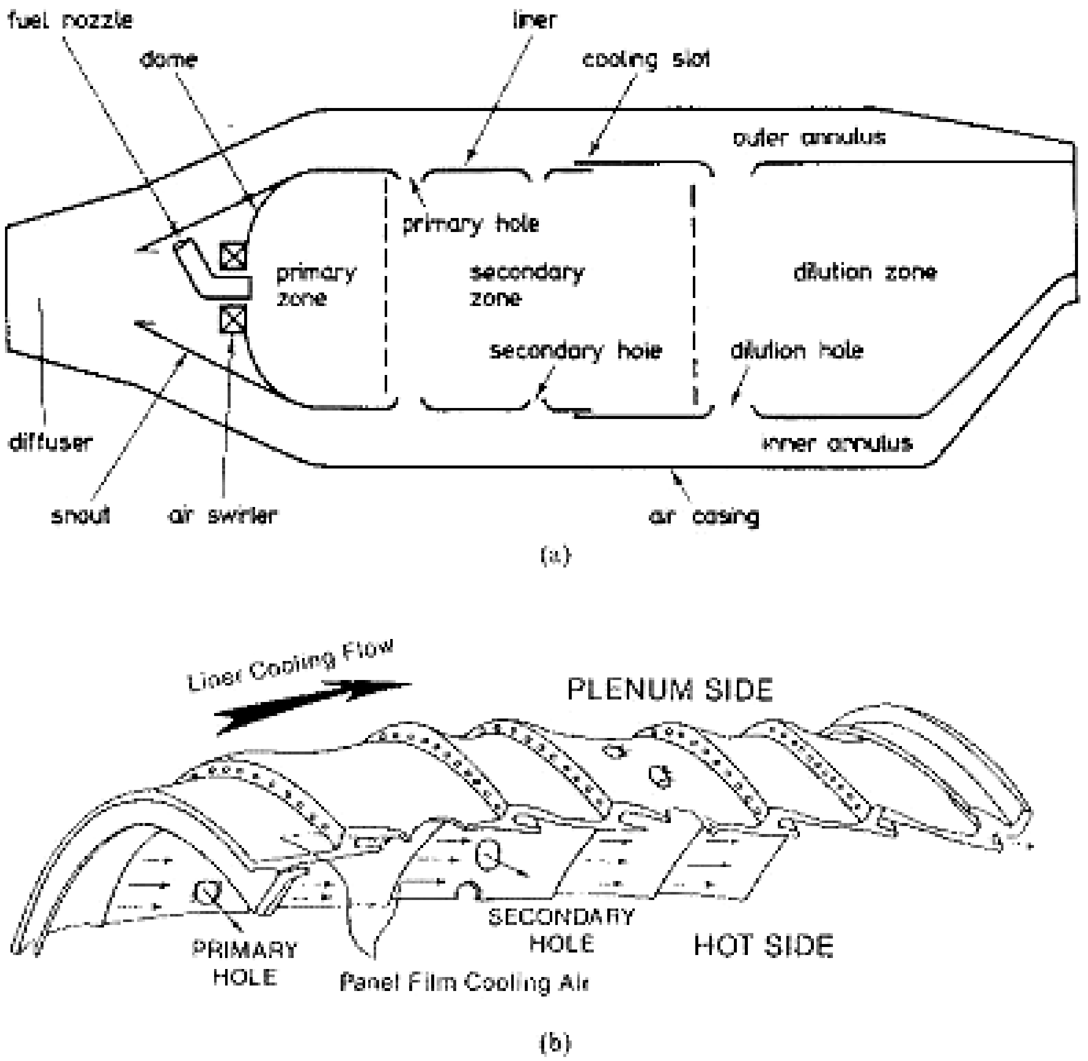

Figure 1.1 a) A schematic view of a typical combustor; b) A cutaway view of a combustor liner [2]

In gas turbine combustion devices, thermal NO_x is the dominant source of oxides of nitrogen [3]. Further, the accommodations, which minimize the NO_x formation, may decrease the flame stability and combustion efficiency. In order to obtain low NO_x emission the use of lean premixed combustion has been preferred over non-premixed combustion by gas turbine manufactures. Through mixing of the fuel and air in lean proportions, lean premixed combustion reduces the peak flame temperature obtained near the fuel-air interface in the traditional diffusion flame type of combustors. The degree of premixing determines the uniformity of the thermal field of the flame. In all premixed combustor configurations the fuel and air are mixed upstream to the combustor/flame stabilization device before being injected to the combustor and reacting. Although useful as a method of gas turbine combustion, there are drawbacks associated with lean premixed combustion. Therefore recently lean direct injection (LDI) combustion has moved to the forefront of gas turbine combustion strategies. The combustion strategy employed in this study is a simulated LDI combustion. This selected configuration is atypical because it does not make use of a premixing zone and relies totally on the flame stabilization device and the fuel injector to accomplish rapid mixing. Currently many gas turbine engines are being developed along with internal combustion engines relying on LDI.

The experimental burner used in this study is geometrically similar to injectors employed in practical gas turbine combustors. The form of a burner or a stabilizing device can influence the shape of a flame profoundly. The microstructure of flames can be influenced by many factors. Some of the obvious factors include, if the flame is of the diffusion or premixed type, characteristics of flow (approximately laminar or turbulent); also, whether or not the flame is transient or can be assumed to be steady state can affect the microstructure of a flame. Conditions of laminar flow and steady state are only approximations.

Future gas turbines will continue to have stringent requirements on low emissions, high efficiencies and low costs. Currently, many concepts are in use to comply with federal and state emission codes. The greatest combustion challenges have been and will continually be presented by low NOx gas turbines. It is desired for NOx and other pollutants to be reduced without compromising flame stability and combustion efficiency characteristics. LDI combustion is seen as an extremely viable combustion strategy to help meet the ever changing requirements of the world's power and propulsion needs.

To fully understand the morphology of swirling flows in gas turbine combustors, unconfined and confined non-reacting and reacting flows are investigated. A broad understanding of the complexities associated with these turbulent flows is gained with observations of their fluid dynamics, thermal signatures and chemical behavior. There is need to understand what dominates a flame's behavior relating to emission formation and structure and how that behavior affects the process of combustion. Also it is important to know how a combustor confinement influences swirling flow behavior. One can then use this information for the development of computer models to design future gas turbine combustors. The relationship between flowfield characteristics, intermediate species, temperature and emissions has been determined and shown to ultimately be influenced by a variety of features, from the confinement of the burner to the radial distribution of swirl and the process of combustion. This investigation furthers our knowledge of swirling non-reacting and reacting flows and provides a database of characteristics to help develop and validate computer models.

Specifically, 3-D flowfields are obtained for non-reacting and reacting co- and counter-swirl unconfined flows using PIV diagnostics. 2-D flowfields are obtained for confined flows under non-reacting and reacting co- and counter- swirl conditions. 2-D flowfields are acquired for the confined flows due to excessive reflections from the confinement thus making good quality images of particles in the flow with PIV difficult, with the result of distorting the 3-D flowfield images. Flowfield data is acquired using particle image velocimetry (PIV) that captures instantaneous image pairs and calculates for the mean velocity and rms values of turbulence. The mean velocity and rms values are then used to calculate strain, vorticity and turbulent kinetic energy values for the investigated flows. PIV provides one with a view of an area of the flowfield in which flowfield information is obtained. In this investigation that area is immediately downstream of the swirler exit plane. This allows the investigator to clearly see what effect the swirl distribution has on the internal recirculation zone formation, the turbulence properties, and strain and vorticity fields. The mean velocity fields give visual structure of the flow and velocity components along with velocity magnitudes that give insight into velocity distribution and velocity decay. The mean and temporal flowfields provide visual information on the magnitudes of velocity on the presence of internal recirculation zone as well as its formation. The rms velocity fields' aid in determining turbulence characteristics of the flow that shed light on the mixing achieved in the various flowfields. The strain and vorticity fields further provide information on mixing along with the location of reaction zones and areas of chemical processes within the flows.

In addition to the flowfield data chemical behavior is archived using optical emission spectroscopy (OES). This data provides information on the location and relative intensity of flame radicals such as CH and OH. The distribution of these flame radicals provides information on heat release in the case of the CH radical and a marker of the reaction zone in the case of the OH radical. They also help to substantiate conclusions on flame mixing determined from the flowfield data. In conjunction with the already mentioned flame generated species data, the C_2 species intensity captured at two narrow wavelengths provided the gas vibrational temperature fields. These temperature fields provide information on the thermal field uniformity (or its lack of uniformity) from within the flames.

The vibrational temperatures are contrasted with another non-intrusive temperature field diagnostic that is based on infrared (IR) radiation emitted from the unconfined flames. Confined infrared temperature distributions are not captured due to stronger transmittance of the infrared signal from the quartz windows (in the 8 to 9 microns wavelength) used for the flame confinement. The IR temperature distribution provides another source of planar temperature distribution for visual examination of temperature distribution and to draw conclusions about different aspects of the flowfield data results on the spatial distribution of temperatures.

The planar temperature distributions are followed up with compensated thermocouple temperature measurements carried out at downstream locations of the internal recirculation zones for unconfined flame cases only. The thermocouple measurements are taken because they allow for the determination of integral- and micro- time scales. These thermal time scales as well as the flowfield data have a direct impact on the emissions from the combustor.

Gas sampling is used to acquire emissions from the post combustion gases. The acquired emissions are of CO, CO_2, and NO. This data shows the end result of the observed flowfield and temperature field characteristics. Also the thermal time scales can be correlated with the obtained emissions data where the different time scales result in high emissions of various species. All of the above data works together to provide an insightful picture of non-reacting and reacting swirl flows. The data systematically shows how fluid dynamic processes affect chemical behavior and spatial distribution of radical species and temperature. The end result is ultimately how these upstream characteristics of fluid behavior, chemical behavior, and temperature distribution lead to emissions and show desirable characteristics of the investigated swirl flows and how these flows can be manipulated to better function in all of their practical applications.

Chapter 2: Background

2.1 Lean Direct Injection Combustion

There are several low NO_x combustion strategies that are in use today in a variety of engines and industrial processes. A few are lean premixed gaseous combustion; lean premixed prevaporized (LPP) injection, lean direct injection (LDI), and rich-burn/quick-mix/lean-burn (RQL). They each rely on the rapid and thorough mixing of air and fuel to minimize all pollutant emissions and maximize combustion efficiency. Gas turbine efficiency targets are moving towards higher turbine entry temperature. Currently today that temperature is approximately 1700 K. The future trend of higher turbine entry temperatures could lead to higher thermal NO_x. The LDI concept seems to be a viable method for obtaining those higher temperatures but also controlling thermal NO_x emissions. LDI is a partially premixed diffusion type combustion process. It relies on fuel injection into a highly turbulent area where turbulent/mixing timescales are targeted shorter than chemical timescales. The Damkohler number is less than unity.

$$\tau_{mixing} < \tau_{chemical} \Rightarrow Da = \frac{\tau_{mixing}}{\tau_{chemical}} < 1$$

The above equation indicates a short residence time, which is beneficial for reducing NO_x emissions.

LDI combustion avoids many of the potential drawbacks of lean premixed combustion, in both gaseous and liquid fuelled systems. These disadvantages are flame flashback, acoustic instabilities, lean blowout limits and oscillations, and low turndown ratios [4, 5]. LDI can also improve upon and provide a good pattern factor. It also encompasses many of the benefits of RQL. LDI combustion involves injection of the fuel prior to the combustion zone causing rapid and most probably partial premixing of the fuel and air.

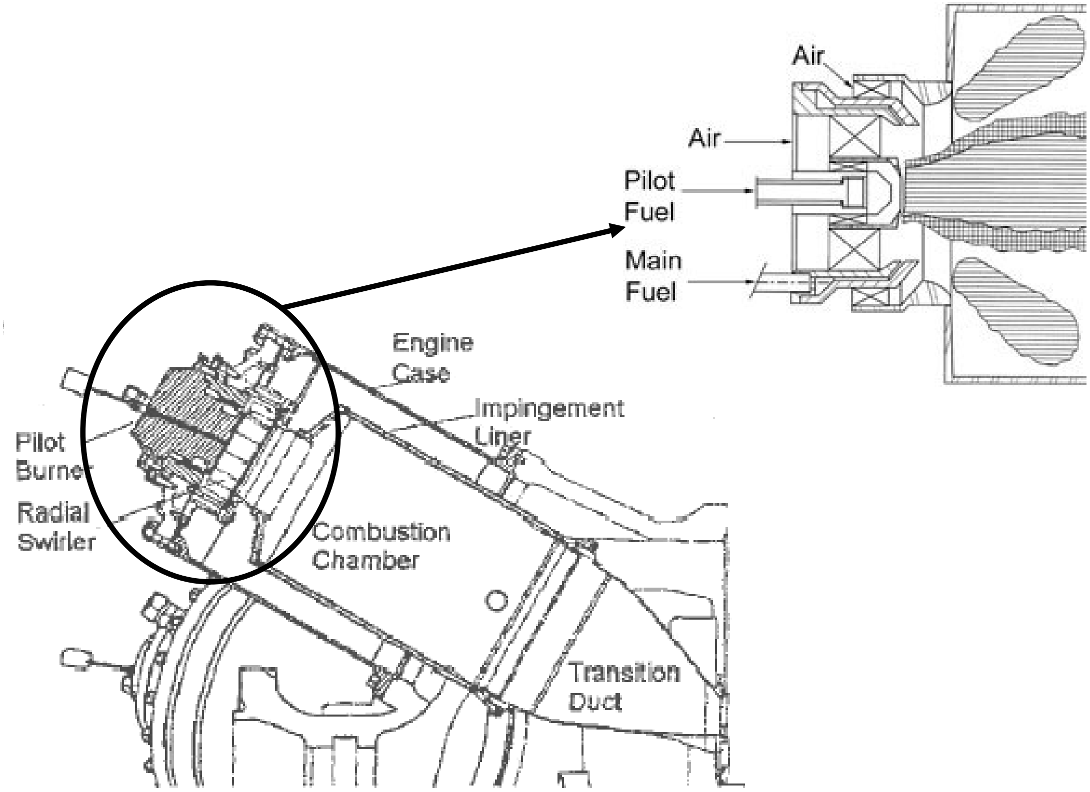

Figure 2.1 A Schematic diagram of LDI concept gas turbine combustor geometry [6, 7]

Injection of fuel into turbulent airflow at the combustor dome, that provides a homogeneous, lean fuel-air mixture, is a key concept of LDI combustion. For liquid fuels the dispersion of the fuel into smaller size droplets is also very important. This LDI concept allows for enhanced lean stability limits, better combustion efficiency and reduced emission of NO_x and other pollutants. It is currently the source of vast research for aero- and marine- propulsion. Its practical importance is paramount and therefore an integral part of this research.

2.2 Swirl Flows

Turbulent diffusion, premixed flames, and a combination of the two (partially premixed flames) are employed in a variety of combustion devices. Examples of these devices are: premixed and nozzle mixed gas burners for industrial or commercial applications, premixing/prevaporizing gas turbine combustors, lean direct injection gas turbine combustors, turbojet afterburners, and spark ignition engines.

In a practical device, such as a gas turbine, a stable flame is desired. This stabilized flame guards against flashback, liftoff, and blowoff over the devices' operating range. Methods used to stabilize flames are: low velocity by pass-ports, bluff body flame holders, refractory burner tiles, a rapid increase in flow area creating recirculating separated flow, and swirl or jet induced recirculating flows.

A flame is stabilized at the flame front. This important characteristic innovation of the flame symbolizes a separation zone between cold reactant mixture or unburned fuel and hot combustion products. At the flame front high temperature fluctuations occur because of a very powerful transportation mechanism.

The flame speed for a premixed or partially premixed flame is defined as the velocity of the unburned gases through the combustion wave in the direction normal to the wave surface. This flame speed is a function of the combustion reaction kinetics, temperature and pressure. The fresh reactant mixture, unburned fuel-air mixture, moves in the opposite direction of the flame. The speed of the flame and the speed of the supply (unburned fuel-air mixture) are equal and opposite, as presented in the sketch below.

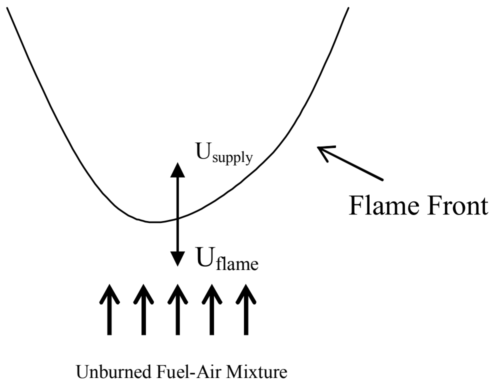

Figure 2.2 A sketch of velocity distribution for a stable premixed or partially premixed flame

In this investigation, the method of stabilization is by swirl to the reactants. In combustion systems, the strong favorable effects of applying swirl to injected air and fuel is extensively used as an aid to stabilization of the high intensity combustion process and efficient clean combustion [8]. The reactants in this study are propane and air supplied in quantities to provide a lean propane-air mixture. Propane was chosen as the fuel of choice because it has a resemblance with liquid hydrocarbon fuels (with respect to heavier than air and carbon to hydrogen ratio), its availability and use in previous research work on swirl stabilized premixed flames in the experimental burner used in this study. Propane is a more complex fuel than the other considered fuel of methane and most fuels in practical use have more carbons than methane. That makes a propane/air mixture more useful for this investigation. Stabilization by swirl is commonly used for many premixed and nonpremixed gas turbine combustion systems. This made it more attractive than another method of flame stabilization. A recirculation zone is created because of the swirl component introduced to the incoming gas flow. This well-known phenomenon in swirl flows is vortex breakdown, which creates the recirculation zone [8]. With high rotation imparted to the flow, it causes recirculation in the core region [8, 9]. Swirl components produce strong shear regions, high turbulence, and rapid mixing rates, which helps stabilization and mixing [8, 9]. Figure 2.3 shows an illustration of a swirling flow flame.

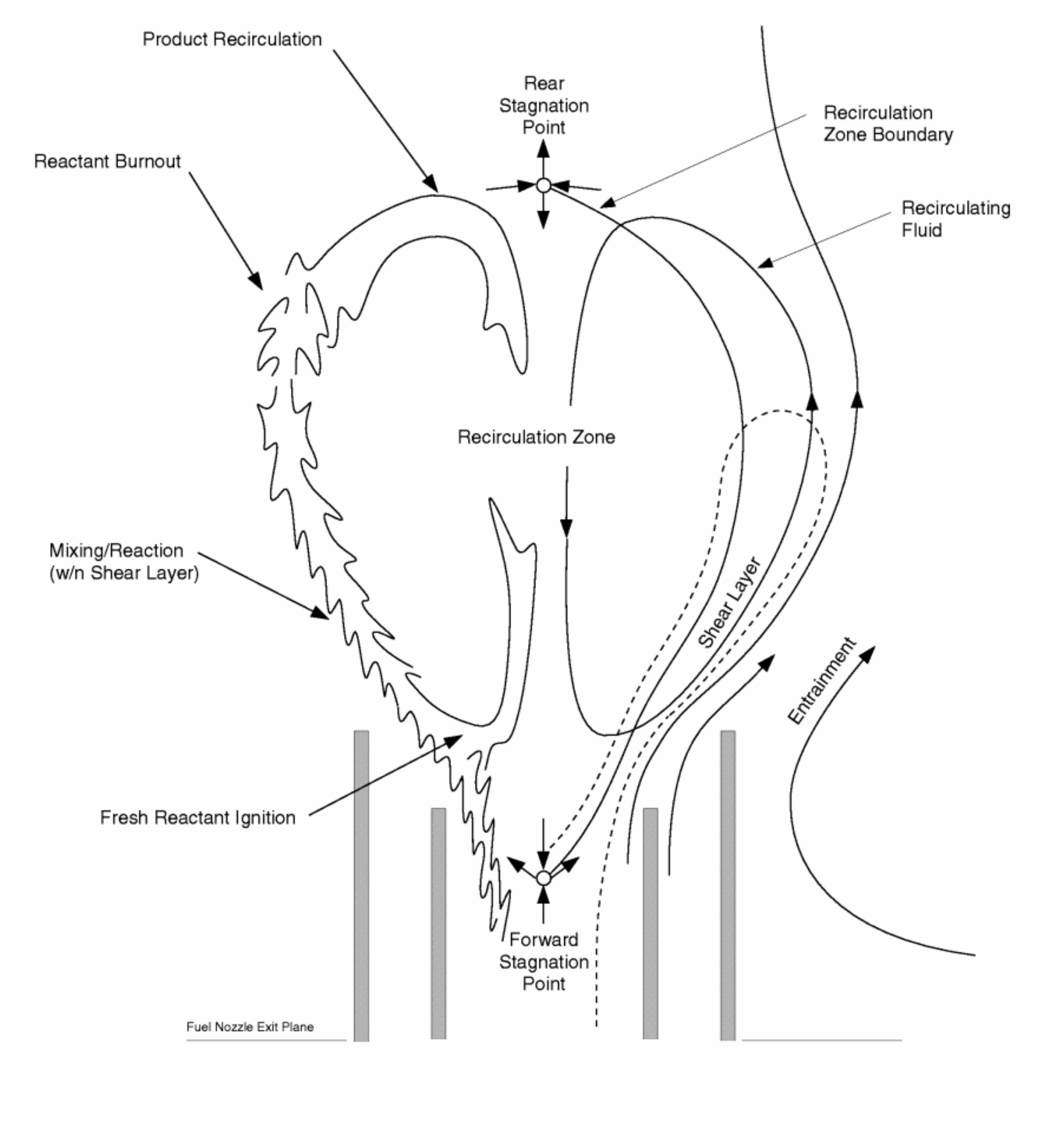

Figure 2.3 An Illustration of a Swirling Flow Flame [10]

In swirl flows, it is possible to control flame length with the amount of swirl imparted to the incoming flow. In work done by Gupta et al [8], Kilik [9] it can be seen that there are factors that govern the size of the recirculation zone. Recirculation zone size was reported to be increased with the following:

- Increasing the number of vanes, i.e., a decrease in the space chord ratio
- Increasing the swirl vane angle from the forward flow direction

- Changing from flat to curved swirler vanes

In this study, the effects of increasing the swirler vane angle are not further explored. Rather the effect of varying the shear strength or the radial swirl distribution is explored. This is done by looking at co- and counter- swirl arrangements made possible by varying the outer swirler of the double concentric swirl burner. The outer swirler is varied between 50° and -50°. The -50° imparts a counter-rotating motion to the supplied combustion air.

For the most part, many fundamental studies on swirl have been done in single swirl combustors. Most practical systems use multi-annular or double concentric swirl burners. This type of burner gives you the freedom to vary the distribution of axial and angular momentum of air or air/fuel jets. In this study a double concentric swirl burner is used because it gives a more practical view of swirl flows as seen in widely used technology. The employed double concentric swirl burner allows for air to flow through two annuli and fuel to flow through a central pipe. This arrangement allows for the implementation of the LDI strategy. Swirlers provide a key component in LDI combustion and are essential in the LDI concept and in this study. The burner is further described in Chapter 3.

2.3 Experimental Philosophy

In this study two possibilities of controlling thermal NO_X formation are combined in a single combustion process. These are the concepts of lean direct injection (LDI) combustion and controlled swirl stabilized combustion. The concept of LDI combustion is so designated, because the fuel and air are injected in lean proportion before they enter the combustor. This will keep the combustion temperature low, which avoids high thermal NO_x formation. NO_x reduction can also be enhanced by proper utilization of swirl, as it induces a phenomenon known as vortex breakdown, where a central recirculation zone is formed [11]. The central recirculation zone is the region of the flame that recirculates and burns hot volatile gases released from the fuel, in a low oxygen region, enabling the suppression of NO_x.

A normal gas turbine combustor consists of an array of injectors, which stabilize flames within the annular plenum. Fuel and air are injected into an annular combustor through a series of concentric jets for most gas turbine engines. This annular combustor is situated between the turbine and the compressor section. A magnification of this can be seen in figure 2.4. An experimental double concentric burner is used for this study. In the experimental LDI facility the neighboring injectors have been removed leaving a single injector or burner. Since there is only a single injector, the effects between different injectors (injector-injector interaction) will not be investigated. Multiple injectors do play a role in the combustion process. The influence of flame interactions (i.e., injector) plays typically a secondary role in determining combustion characteristics. In this study they are assumed to have a negligible effect on the aspects under study. The combustor walls are part of this experiment. The influence of confinement is a major variable in this investigation.

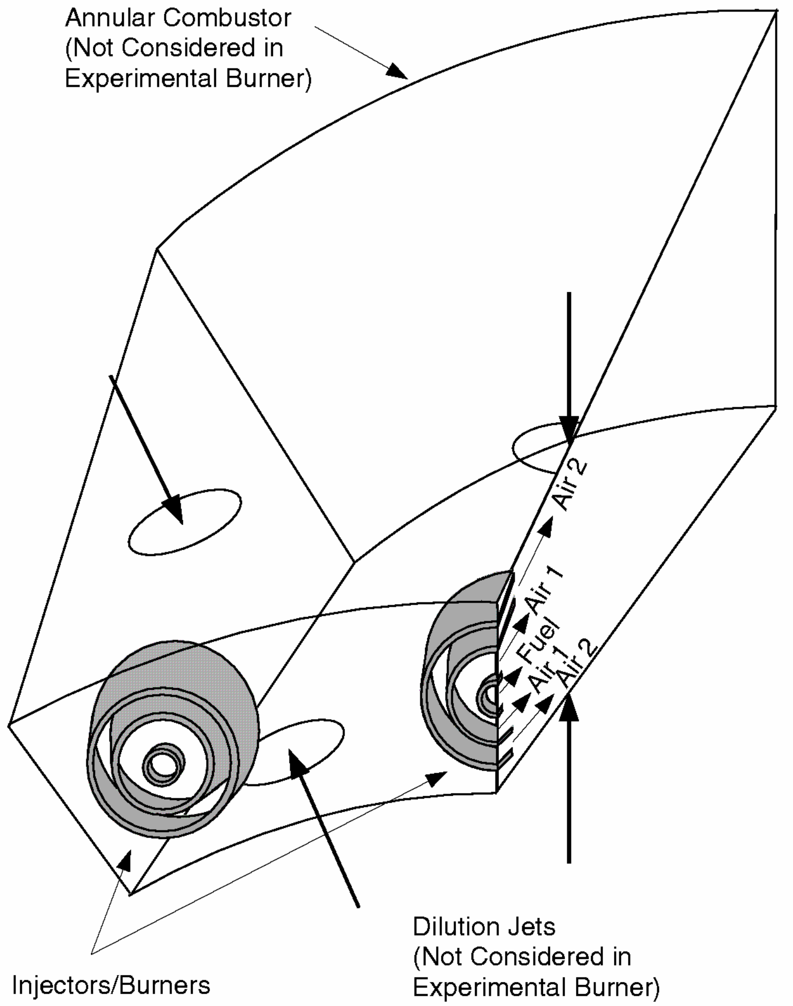

Figure 2.4 An Illustration of an Annular Combustor [12]

This single injector is used to create flames similar to those present in conventional gas turbine combustors. This type of single injector configuration can also be applied to other combustor configurations such as can or can-annular.

The test facility is supplied with propane from compressed gas bottles. Propane is very similar to liquid hydrocarbon fuels, which are more complex since they must undergo droplet atomization, vaporization and mixing prior to combustion.

Practical gas turbine engines may use either natural gas (consisting of 95% methane) or liquid fuel such as JP-4 (similar to kerosene) [12]. Natural gas flames are modeled very well in this facility. The advantages of propane over methane are that it has higher density and a higher boiling point. Therefore it can be easier to handle and take up less storage space than methane. It may also help in allowing the facility to simulate flame behavior of combustors using liquid fuel. There is a time delay associated with burning liquid fuels due to the fact that the liquid droplets must evaporate before they can burn. A difference in flame behavior might arise due to this time delay. Because propane has a high density and can be stored as a liquid at ambient temperatures by modest pressurization of the fuel tank, this difference may become negligible.

The radial dimensions of the facility are geometrically similar to those of a practical combustor configuration. With air at 25 psi the flowrates are 10.52 scfm (standard cubic feet per minute) and 21.88 scfm for annulus 1 and annulus 2 respectively. The fuel flow was supplied at a pressure of 15 psi at a flowrate of 0.8509 scfm for the central pipe. These flow conditions provided an equivalence ratio of 0.625, which is lean, and a momentum ratio of 0.693 (between annulus 1 and annulus 2), both of which are held constant.

The facility is designed to stabilize and control lean direct injection gaseous hydrocarbon (i.e., propane/air or methane/air) flames for use with advanced diagnostics. The facility consists of a double concentric burner with an in house designed fuel injector, axial flat vane swirlers, and removable combustor geometry for confinement of the flow. These items are discussed fully in Chapter 3.

2.4 The Present Contribution

Swirling flows with combustion have numerous practical applications. It is these practical applications that make this field of study a great interest too many investigators and the world. Many general trends are presented by earlier reviews of swirling flows with and without combustion [8, 11, 13, and 14]. From very fundamental isothermal flows as well as reacting flows to those formed in very complex swirl combustor geometries, numerous experiments in swirl flows has been carried out. Experimentation has successfully established many general characteristics of swirl flows. Swirl is important in promoting flame stability, increasing combustion efficiency and controlling emission of pollutants from combustion [8]. Swirl is of practical importance in combustion not only as a natural feature but mainly in its ability to induce vortex breakdown [8, 9, 15-17].

It is evident that a variety of research has been performed in swirl flow combustion systems. The need for additional fundamental research is apparent though from how much we still do not understand about these complex flows and the limited amount of data that is available in co-annular combustion systems. These injectors are employed almost exclusively in modern gas turbine combustors.

In order to understand the complex features associated with the non-burning and burning swirl flow conditions, detailed examination is made of the mean and turbulence characteristics of the flow under different swirl distribution conditions in an unconfined and confined burner-combustor configuration. Several previous studies have examined the flow structure associated with swirling flowfields using laser Doppler velocimetry (LDV), hot wire anemometry (HWA), and other methods

[18-22]. As an example, Syred et al. [18] provide information on three components of velocity and six components of turbulent stress tensor using HWA in an isothermal flow. The availability of particle image velocimetry (PIV) allows one to determine the flowfield instantaneously in 3-D under both non-burning and burning conditions. Recently PIV has been used in a variety of ways by several researchers. For example, PIV has been used to measure the velocity field of swirling flows from two co-rotating coal burners [23]. It has also been utilized to determine strain and stretch in flames [24]. PIV has been used to study the structure of turbulent premixed flames [25, 26]. It has been used to determine aerodynamic strain rate, rate of flame stretch, vorticity and strain rate during the flame vortex interaction [27]. PIV has enabled researchers to gather velocity measurements in laminar and turbulent premixed flames [28]. Most of these studies involved mostly 2-D planar PIV data and not stereoscopic 3-D data that is a part of this research.

In this study, particle image velocimetry (PIV) has been used to determine the flow characteristics under unconfined and confined environments. The PIV instrumentation employed has been developed to allow measurements under combustion conditions [29] that are often associated with high background radiation. This diagnostic tool is instrumental for determining the instantaneous and mean velocity, turbulence characteristics, strain and vorticity associated with the flow. These flowfield quantities and data can provide information on the local residence time distribution in the combustor. These parameters influence the emission of pollutants, including NO_x. The NO_x reduction can be enhanced by proper utilization of swirl, as it induces the previously mentioned phenomenon known as vortex breakdown, where a central recirculation zone is formed [8, 11]. The internal or central recirculation zone is the region of the flame that recirculates and burns hot volatile gases released from the fuel, in a low oxygen concentration regime, thus enabling the suppression of NO_x.

Utilized in this study is a complete facility that was designed and constructed for simulating and conducting gas turbine combustor research in practical geometries. The facility consists of a double concentric swirl burner with fuel injector, axial flat vane swirlers, and removable combustor geometry for confinement of the flow. Facilities and procedures for global flame properties visualization, 3-D and 2-D PIV, optical emission spectroscopy (OES), infrared thermometry, temperature measurement using micro-thermocouples, and emissions gas sampling have been established and used in this investigation. The diagnostics were employed to ascertain and examine the effect of confinement, combustion, and radial swirl distribution on the formation of the internal recirculation zone, overall flow characteristics, chemical behavior and temperature of non-reacting and reacting swirling flow. Co-swirl and counter-swirl flow, both without and with combustion, are examined to gain an understanding of the flow dynamics associated with complex swirling flowfields in unconfined and confined burner geometries. This study examines the differences in morphology, along with flow characteristics, and chemical behavior of unconfined and confined swirling flowfields with varying radial swirl distribution. Great care was taken to ensure that other governing inlet parameters did not affect those of interest.

The study examines at two swirl distributions, a co- and counter- swirl configuration, under both non-reacting and reacting conditions. The effect of both unconfined and confined combustor geometry is conducted to compile an initial database of swirling flow characteristics to further knowledge of these practical flows. This detailed database assists in the development of computer modeling and quantifies desired effects and characteristics of swirling flows and LDI combustion.

Chapter 3: Experimental Facility, Diagnostics, and Techniques

3.1 Experimental Facility

The facility used in this investigation consists of several sections. These sections are a burner, a flow control system, and a combustion chamber or enclosure. Each part combines to assemble the needed test facility. They are described in detail below.

3.1.1 Experimental Burner and Lean Direct Injection Geometry

Figure 3.1 shows a schematic of the experimental burner used in this study. The burner itself is contained within a fixed rack. The burner rack enables the flame to burn without disturbance. As seen in figure 3.1, the burner can be described in two sections. The sections are the flow conditioning section and the flame stabilization/LDI geometry section.

Three pipes that are placed inside each other construct the flow distribution system to vary the radial distribution of air flow into the burner. The three pipes are the two annuli and the central pipe. Directly injected into the central pipe is the desired gaseous fuel that is metered by an upstream flow meter. The fuel for the central pipe passes through its flow meter and into more tubing. The tubing carrying this fuel is isolated from the tubing carrying combustion air to the annuli. The two annuli receive air that first enters into flow distributors where they are split into four streams. These flow distributors are situated at the sides of the burner. Each of the two annuli receives an injection of four streams. This distribution upstream from the injection point achieves a high grade of mixing and turbulence.

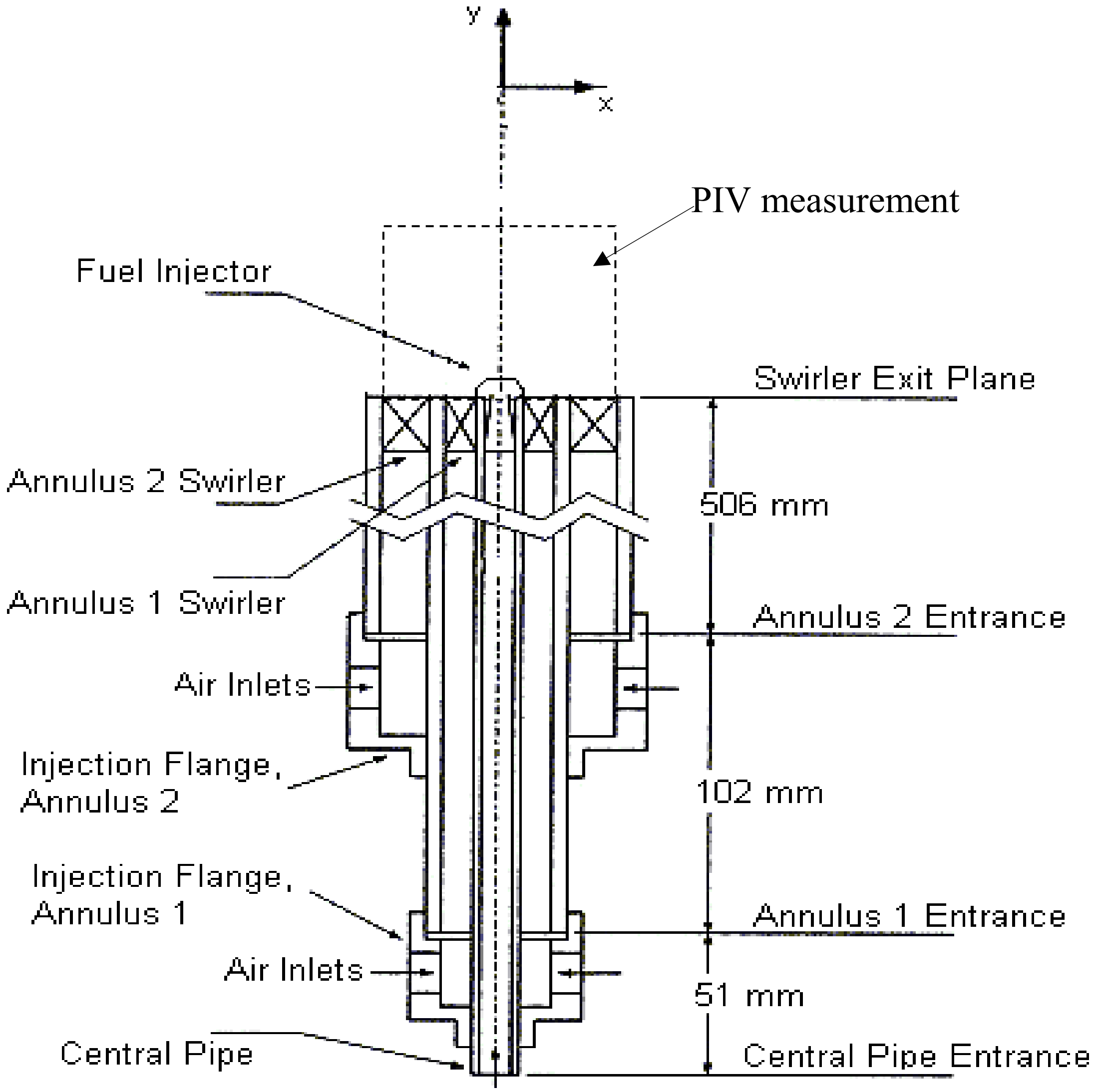

Figure 3.1 Experimental Burner and the measurement region for Particle Image Velocimetry

The LDI geometry/flame stabilization section, figure 3.2, consists of two swirlers for the two annulus air jets and a fuel injector via the central pipe jet. The swirlers are constructed of an inner ring and an outer ring with eighteen flat vanes fixed between each ring. These swirlers are used to provide a swirl flow as described in chapter 2, the Background chapter. Fuel is allowed to flow only through the central fuel injector located on longitudinal central axis of the burner.

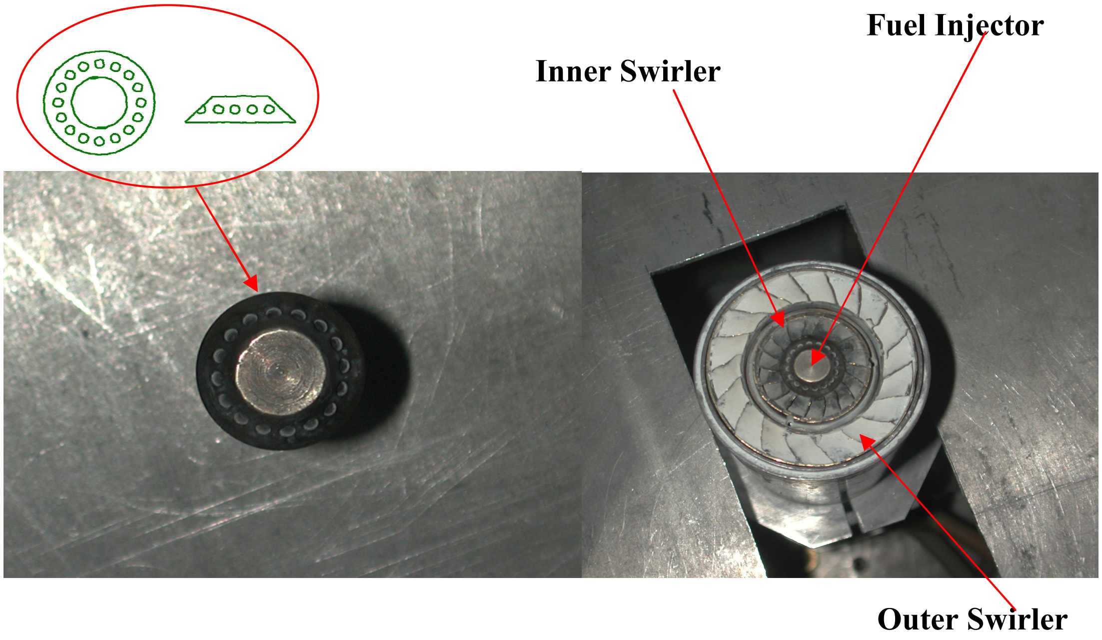

Fuel Injector **LDI Geometry**

Figure 3.2 Photographs of Fuel Injector (left image) and Lean Direct Injection Geometry (right image) showing fuel injector, inner swirler, and outer swirler

The fuel nozzle allows direct injection of fuel radially outwards into the surrounding combustion air via 16 holes, each of 1/16 inch diameters. The radial holes of the injector sitting at a 45° angle allow small amounts of fuel to be injected into the swirling air to insure lean conditions and rapid mixing. The setup provides simulation of LDI configuration and is examined here in detail using advanced diagnostics. This particular LDI geometry provides for a well-defined symmetric interface between the central pipe stream and the surrounding annulus 1 stream at the nozzle exit.

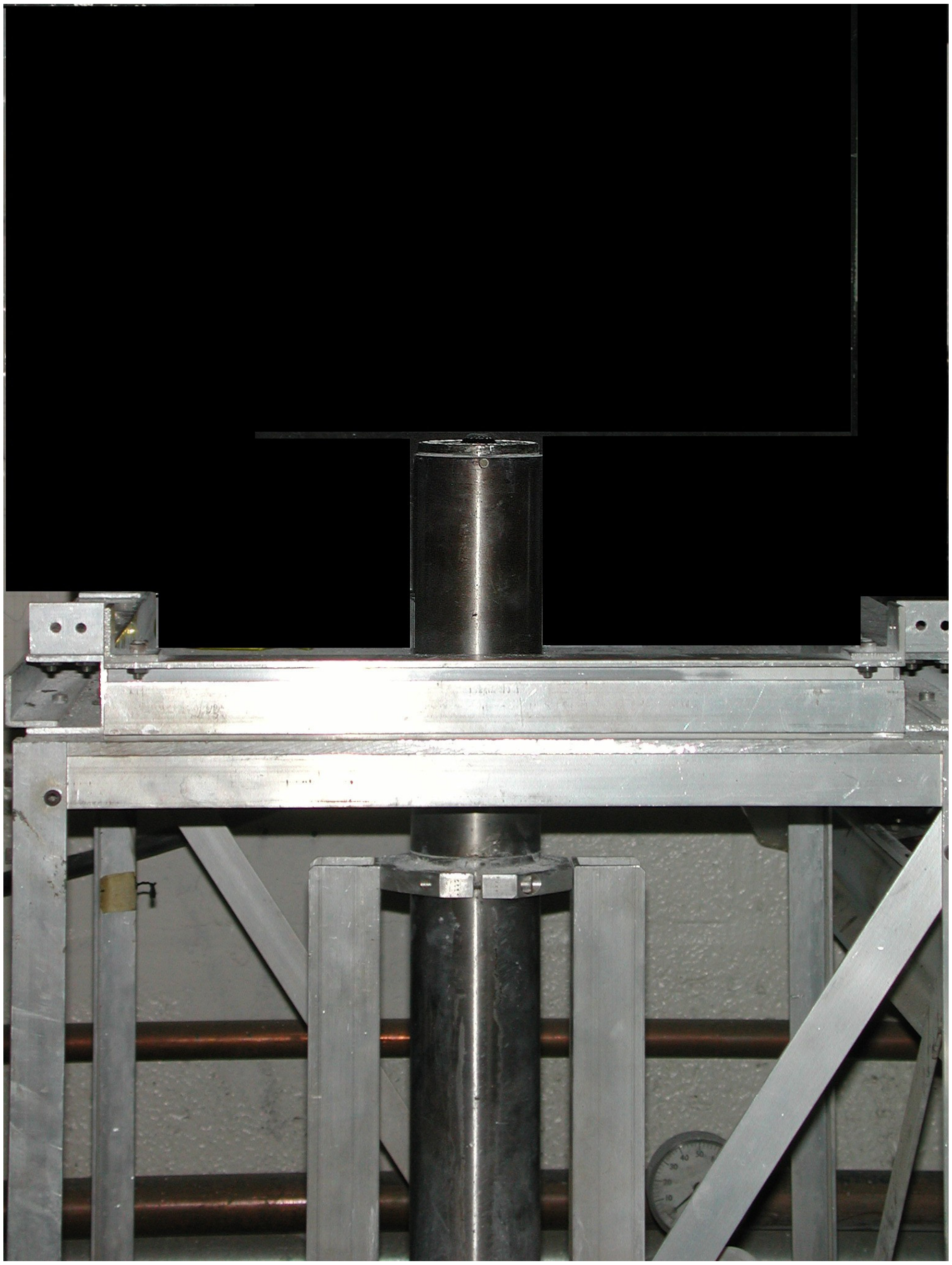

Figure 3.3 Photograph of Experimental Burner in test stand.

3.1.2 Flow Control System

In this investigation, a compressor (Ingersoll Rand 100 hp) that delivers a 125-psi of air, with a 4000-liter air tank supplies high-pressure air to the burner facility. This air is supplied continuously and constantly. This air is dried and cleaned by an air filter, Deltech 810 Series filter**.** 100 pound pressurized propane bottles supply the fuel. The fuel delivery pressure is controlled at 15-psi with a pressure regulator.

The compressor facility and the propane fuel bottles are connected to a control panel. Brass constructions are used to connect these three components together with fitted pressure gauges and regulators. A table of the experimental settings with flow readings and pressures is given in Chapter 4 -- Investigative Methodology. The control panel contains inlets for the air and propane supply along with outlets for the air and propane. Incoming air and propane branch out into three pipes, each containing a valve, a pressure gauge and a flowmeter.

In the fuel flowmeter there are two floats of different materials, a glass float and a steel float. For metering of the fuel flow the glass float is used in this study. The two air flowmeters contain single steel floats. The flow meters have accuracy of ± 5% of full scale. The flow meters used, are a Matheson 605 for the fuel and two Omega dry air flowmeters for the air (for the inner and outer annuli), model FL4513 and FL4514, respectively**.** The flow meters are calibrated for air at standard temperature and pressure. Additional corrections for different pressures and densities are made with an in-house developed excel spreadsheet, given as appendix B.

Flexible Teflon tubes**,** 11/16th inches in diameter are used to connect the pipes downstream of the flowmeters to the burner. The flow and composition entering the three tubes of the burner can be controlled and monitored independently.

3.1.3 Combustor Section

For examination of the confined swirling flowfields, an enclosure constructed of an aluminum and steel frame and quartz glass is fabricated and positioned at the burner exit. The enclosure has a top and bottom plate separated by a rectangular arrangement of quartz glass with dimensions 140mm x 120mm. The square section for visible examination of the swirling flowfields has a circular diameter of 134mm, which allows for a 2 to 1 ratio of chamber diameter to burner diameter. The area reduction from enclosure diameter to chamber exit diameter is about 25%. This area reduction is characteristic of almost gas turbine combustors. Congruent with typical gas turbine engine combustion chamber requirements, it is desired that the chemical energy release take place in the smallest possible volume (length and diameter). Figure 3.4 shows top and side views of the chamber used. A sketch of the burner and the combustor together is given in figure 3.5.

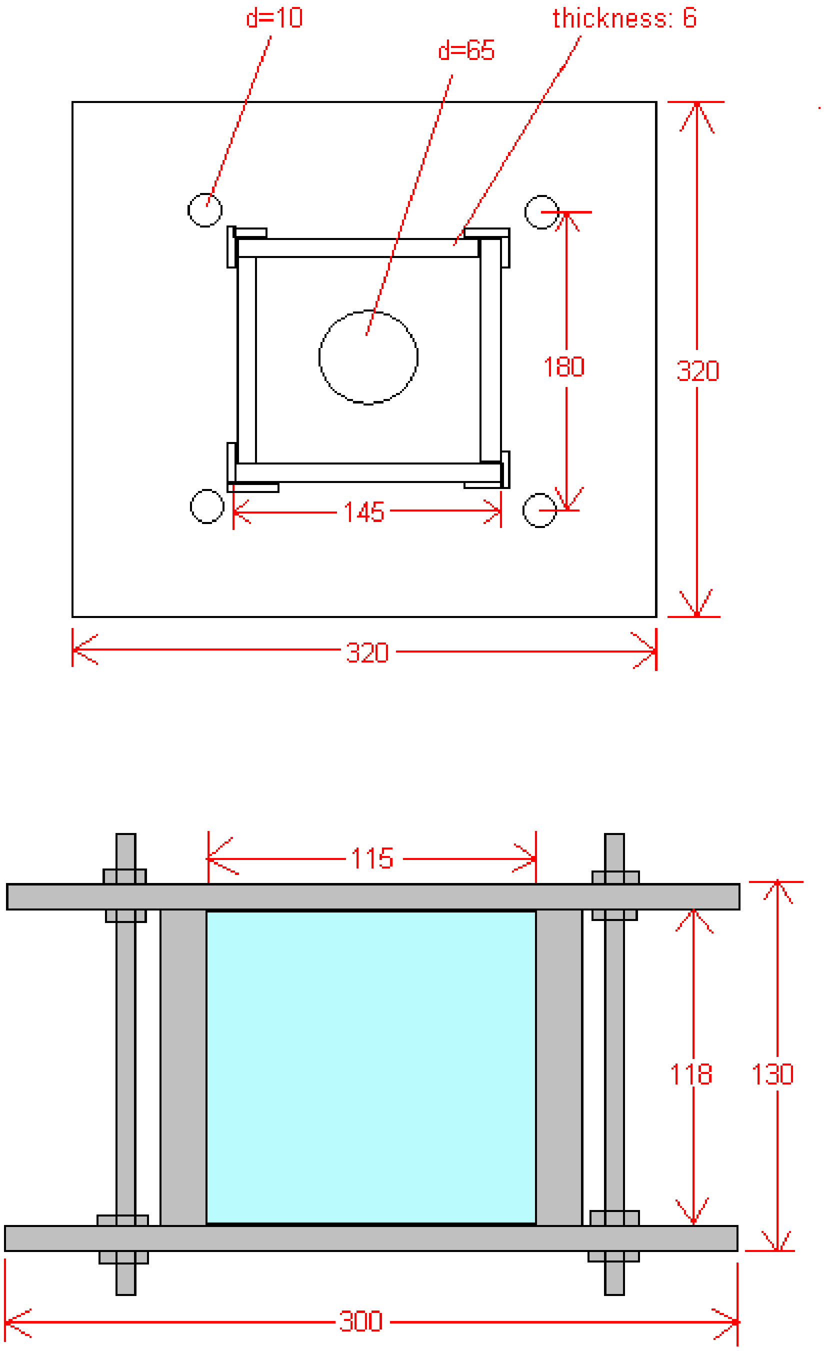

Figure 3.4 Sketches of Top and Front/Side views of Combustor Section

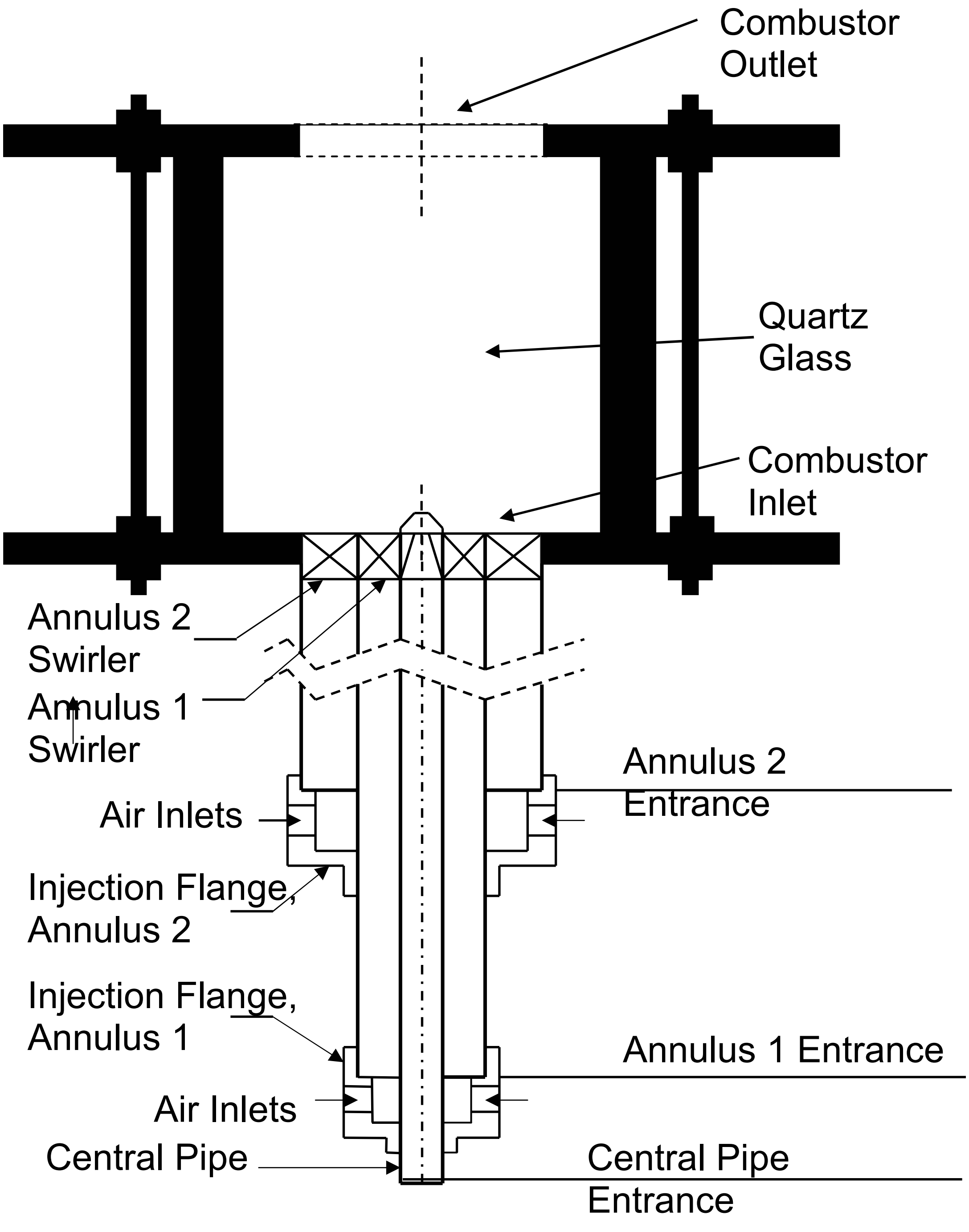

Figure 3.5 A Sketch of Experimental Burner with Combustor Section

3.1.4 Exhaust System

The experimental burner and combustor section is placed under a large stainless steel hood. The exhaust system removes combustion products and/or seeding particles from the laboratory.

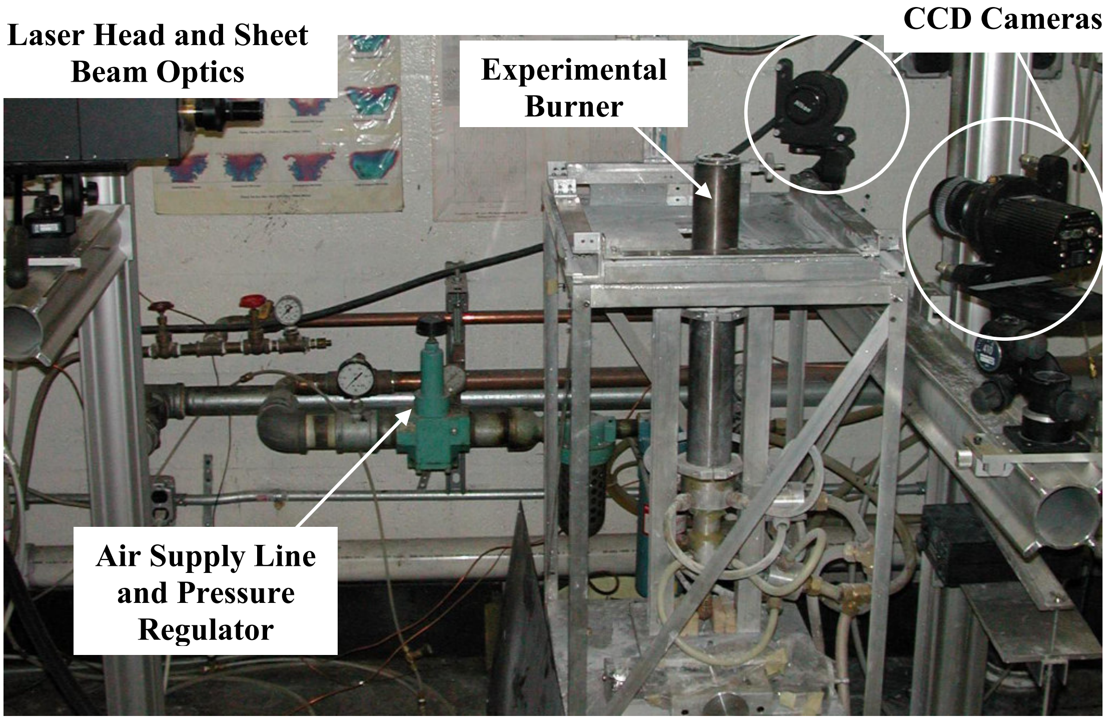

Figure 3.6 A Photograph of Experimental Facility and 3-D PIV Diagnostics

3.2 Experimental Diagnostics and Techniques

In this investigation, a combination of experimental diagnostics is used to investigate the structure and characteristics of the non-reacting and reacting unconfined and confined flows. The diagnostics used each provide another dimension of data to be correlated with the other diagnostic data. There are diagnostics for flow visualization and velocity, thermometry, and chemical behavior. The specific diagnostics employed are direct flame photography, particle image velocimetry (PIV), optical emission spectroscopy (OES), infrared thermometry and gas analysis. Abel Inversion and vibrational temperature calculations are applied to provide further information [35-40]. Each of these diagnostics is further described below.

3.2.1 Direct Flame Photography

Direct flame photography is used to document the characteristic features of flames. These attributes are the light intensities, dimensions, structures and shapes of the different flames. Flame photographs also provide the opportunity to contrast the flames under miscellaneous combustion conditions.

A Nikon COOLPIX 990 digital camera is used to take the flame photographs. The camera has 3.1 million effective pixels. The major adjustable parameters of the camera are the exposure time and the aperture stop. In this study, an aperture of 3.6 is used for each photograph. The exposure time used for these photographs is 1/4th of a second to obtain global information on the average flame image.

The aperture stop on the camera governs the depth of focus of the recorded image field. The depth of focus is the distance an image plane can be shifted without a change in detectable image quality. The large aperture stop of 3.6 provided a good level of illumination of the object on to the image.

The exposure time regulates the length of time that light passes through the lens. Depending on the exposure time, the pictures provide different information about the flame. Long exposure times provide information on the more global structure of the flame. These pictures are more of an averaged photograph of a set of instantaneous photographs. Short exposure time photographs give information pertaining to flame stability.

In this investigation the camera is mounted on a tripod (model Manfrotto 3021PRO) to ensure stable camera positioning. The height of the tripod was fixed at 128 cm from the floor of the lab. The distance from the test section was set with the legs fully spread and the front leg touching the base of the burner stand. The distance between the camera and the fuel nozzle exit is approximately 66 cm. The lens is positioned in line with the top of the burner exit plane injector. Black painted aluminum sheets are placed behind the flame and on top of the test section bottom plate. This is done to eliminate reflections of the flame in the photographic image.

3.2.2 Particle Image Velocimetry

Particle image velocimetry (PIV) has been used to determine the flow characteristics. The system used for the particular measurements was an Integrated Design Tools (IDT) PIV system for 3-D data acquisition. IDT-1000 and an IDT-2000 control module were used to operate the camera for image acquisition. The whole system was operated with proVISION^{TM} software provided by the manufacturer. A SoloPIV Nd: YAG laser was used as the illuminating light source. Gupta et al [29] gives a detailed description of the PIV system that has been successfully developed for use in combustion conditions.

A CCD camera with pixel size of 4.65 μm x 4.65 μm and a sensor area of 7.6 mm x 6.2 mm is used (sharpVISION^{TM} 1400-DE, model Sony ICX205AL CCD). The camera's sensor is a micro-lens interline transfer CCD, equipped with a narrow bandpass filter (0.87nm) at center wavelength of 532nm to allow for maximum transmission and thus alleviating any stray light entering the detectors. The active pixel array of the CCD camera is 1360 x 1024. In addition a mechanical shutter is located in front of each camera to eliminate background radiation entering the camera. In order to trace the motion of flow, Zeeosphere ceramic particles were introduced into the airflow. Zeeospheres are a product of 3M specifically designed to be used as trace particles in fluid flows. The dispersion of small size particles uniformly into the flow is a challenge so that care must be exercised to seed the particles into the flow. A particle seeder is used to sufficiently seed the air streams in both the inner and outer annuli of the burner.

A thin laser sheet beam was used to illuminate the seeded particles in the flow. In the experiments the laser frequency was set at 5 Hz, which was also synchronized with the camera frequency. The particles present in the flow scattered the incident laser sheet light. Two cameras were used to capture stereo images of the scattered light, which allowed one to obtain 3-D stereo data on flowfield. The images are processed with the proVISION^{TM} software to determine the motion of the flow field and the associated turbulence characteristics [30-34]. Tecplot^{TM} software was used to present the graphical data. The basic PIV experimental steps followed in this study are presented in our paper evolved from this study [33].

3.2.3 Optical Emission Spectroscopy

Flame generated species examined from within the flames are studied using an intensified CCD camera, which uses an image intensifier to regulate and adjust the amount of light entering the detector from the flame in the camera. This type of detector is ideal for applications involving ultra low light measurements, or measurement of transient effects. ICCD cameras/detectors use an image intensifier both to gate light on and off and to greatly increase the brightness of the image. In these detectors the image intensifier detects and amplifies the light, and the CCD is used for readout. The ICCD in use utilizes a proximity-focused microchannel plate (MCP) image intensifier fiber-optically coupled to the CCD array. The proximity – focused MCP has PMT-like UV-NIR response, linear geometric accuracy and can be gated in less than 5 nsec with an exceptionally high on/off shutter ratio. The camera is cooled by a Peltier effect thermoelectric cooler [53]. Water is used to carry away the heat generated by the thermoelectric cooler. While the detector is being cooled it is continuously flushed with nitrogen delivered at 10psi with a flowrate of 4.75 scfh.

In conjunction with the ICCD detector, narrow bandpass filters are used to observe selected flame radicals that emit radiation due to the heat generated by the combustion process. These radicals or intermediate species require low energy to be excited and their bands lie in the visible or near ultraviolet regions. They can be excited strongly by the limited temperatures of flames. The species OH, CH and C2 are responsible for the strongest band systems.

These filters installed in the front of the camera/detector allow only a specific wavelength of light to pass. The free radicals or band systems of OH, CH, and C_2, are observed using interference filters with 10 nm bandwidths centered at 307 nm, 430 nm, 470nm and 515 nm. WinView software was used to determine the spatial intensity distribution of these radicals. The software is set to record 30 sequential images with an exposure time of 3 ms. The ICCD camera is operated in shutter mode, which allows for exposure times of milliseconds or longer. The UV Nikkor lens used with the ICCD camera is operated at an aperture of 11 for all data.

3.2.4 Infrared Thermometry

The camera or thermal imager used is a ThermaCAM SC 3000 with cooled quantum well infrared photodetector (QWIP) manufactured by FLIR. The detector is 320 x 240 pixels that detect an infrared signal in the 8-9 μm range. It is stirling cooled down to 70K and has a cooling down time of less than 6 minutes [54]. The basic operation of the camera is to detect the electromagnetic energy radiated in the IR spectral band from the flames. It then converts the radiated energy into an electronic video signal. The IR energy is first radiated through a medium (typically the atmosphere). It then enters the sensing system, passing through a lens, a filter, and finally incidents on a single IR detector or a focal plane array (FPA) sensor, which transforms the radiation into an electrical signal. The radiance captured by an infrared camera depends mainly on the object temperature, background temperature and emissivity of the source object. Mathematically the radiance of an object can be represented by the following equation,

$$L = \varepsilon L_o(T) + (1-\varepsilon) L_b(T_b) \tag{3.1}$$

In the above equation, L is the total radiance captured by the camera in Watt/m^{2}sr. The radiance emitted by the source and is $\varepsilon L_o(T)$. Finally, the term $(1-\varepsilon)L_b(T_b)$, represents the radiance reflected off the source because of background emissions.

The signal and images are obtained, archived, and stored with ThermaCAM Researcher 2001 software. Several factors that can affect the radiance captured are ambient temperature, relative humidity, and external optics transmission. The camera software, ThermCAM Researcher 2001, has inbuilt correction functions for these factors. With the known net radiance emitted by the source object, the camera software calculates corresponding temperature for the radiance value calculated from a digitally stored calibration look-up table. The software incorporates a supplied emissivity that was calculated using a theoretical adiabatic flame temperature and assumed complete combustion with CO_2 and H_2O accounting for the sources of infrared radiation to determine the gas emissivity.

The confined thermal images could not be recorded due to non-transmittance of the quartz glass.

3.2.5 Emissions Measurement

Invaluable information is provided by emissions measurements. Although, only mean data is available, this information allows for the evaluation of pollutant formation characteristics and combustion efficiency. When correlated with temperature measurements, emissions data gives greater insight into the combustion process. One can hypothesize about the formation of these product gases with this type of analysis.

Gas samples are obtained with a water-cooled gas-sampling probe. The probe is cooled to alleviate further reaction of the sample during its transit time in the sample. Downstream of the probe, the samples pass through a desiccant dryer, a gas filter, and a non-lubricated pump to avoid sample contamination. From the pump the samples flow through several valves and flow meters and finally to the analyzers.

The probe itself is made out of stainless steel. It has dimensions of 0.15 cm for inner diameter, 0.94 cm for the outer diameter, and 87 cm long.

The cooling water flow is assumed to be sufficient as no bubbling is witnessed on the outside of the probe. A pressure of approximately 3 bars (≈ 44 psi) to the cooling water is supplied to the probe. The flowrate is approximately 4 l/min.

The dessicant dryer is a tube filled with Indicating Drierite, manufactured by W. A. Hammond Drierite company. It changes color from blue to pink as it absorbs moisture.

The filter is a 2.5 micron particle filter. It is used to remove particulate matter from the gas stream. It is an inline filter manufactured by Swagelok.

The pump used is a Cole Parmer Masterflex pump model #7015-20. Its drive is a Cole Parmer model 302-FM B with a forward and reverse direction

Emissions are taken at a downstream location that corresponds to a distance of twice the outer diameter of the burner. The outer diameter is 65 mm. This position is chosen because it was assumed it was sufficient distance for plug flow conditions to be achieved and also at this distance the combustion is essentially complete. Measurements are not taken upstream of the flame because a plug flow cannot be obtained and the presence of a probe would disturb the flowfield of the flame so that obtaining accurate results will be questionable.

The sample gas is passed to a portable Horiba Gas Analyzer, a PG-250, which contains detectors for carbon monoxide (CO), carbon dioxide (CO_2), nitrogen oxides (NO_x), and oxygen (O_2). The analyzer displays the concentrations of CO and NO_x in ppm and the concentrations of CO and O_2 in volume percent.

Before the sample gas is passed to the analyzer and the various detectors, calibration gases of know quantities are flowed to calibrate the used detectors to ensure reporting of accurate values. Each detector is calibrated independently.

All instruments are calibrated with a zero gas and an upscale/calibration gas. Nitrogen is used as the zero gas, since it does not contain nitric oxides, carbon oxides and it is not magnetic. With this gas the zero point of each analyzer scale is set.

For setting a second point, the upscale, of each analyzer scale, different calibration gases are used. In case of the NO/NO_x analyzer a mixture of 151 ppm nitric oxide in nitrogen, for the carbon monoxide (CO) analyzer a mixture of 899 ppm carbon monoxide in nitrogen, and for the carbon dioxide (CO2) analyzer a mixture of 5.06% carbon dioxide in nitrogen. The calibration gases and the zero gas are obtained from gas cylinders provided by Air Products.

3.2.6 Abel Inversion

Abel's integral equation is frequently used for the inversion of experimental data in various areas of physics, mainly in flame and plasma diagnostics. If the source (intensity distribution) is optically thin, and if the symmetry is known, then the true distribution can be calculated from the projected intensity profiles. We have used this method to reconstruct a cylindrically symmetric source from its two dimensional profiles and then apply the Abel integral equation to our data to obtain the true 3-D distribution. The Abel inversion methodology employed in this study is described and adapted from work done by Gupta [35].

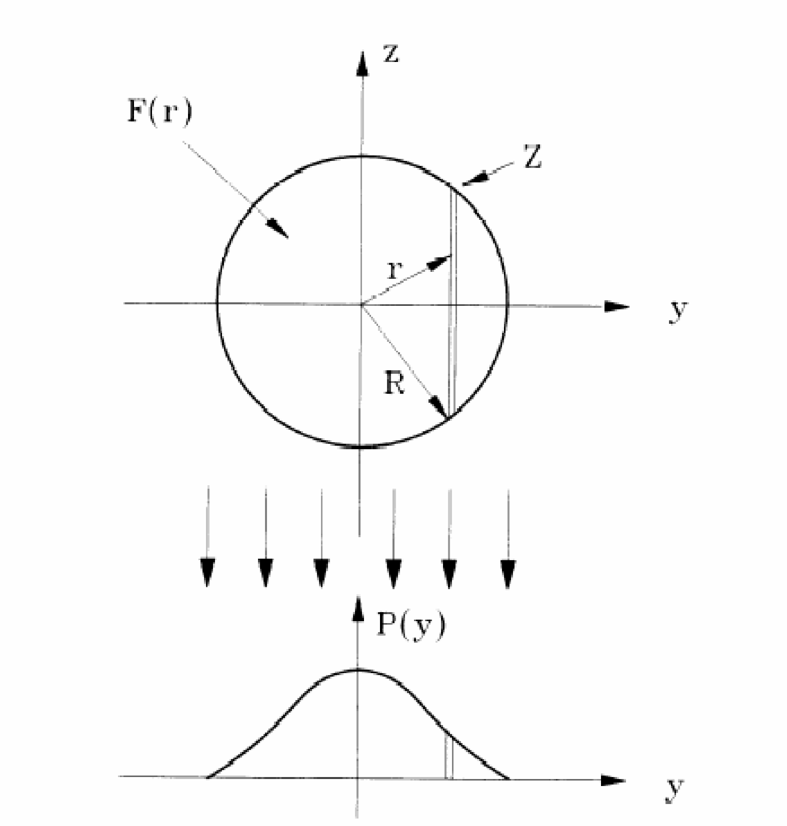

Figure 3.7 Illustration of the geometrical relationships between variables in the Abel Inversion Technique [35]

For a source with a cylindrically symmetric distribution, *F(r)*, as shown in figure 3.7 above, an infinitesimally narrow slice is projected onto the screen below. The projection profile *P(y)* is given by

$$P(y) = 2\int_{0}^{Z} F(r).dz \tag{3.2}$$

where *F(r).dz* is the part of the source located at a radial distance *r* from the axis. In equation 3.2 the integral is taken along a strip at constant *z*, and the variables have the relationship $y^2 + z^2 = r^2$, $Z^2 = R^2 - y^2$, and *R* is the radius beyond which *F(r)* is zero. Since we have a large intensity data array (360×360), on which we need to perform this inversion integral, an efficient numerical algorithm is required. We have chosen an algorithm introduced by Cameron J. Dasch [36].

This Abel inversion technique is not restricted to a specific source distribution. It assumes that the line of sight integrated projection data are taken at equally spaced intervals Δy. The inversion can be represented by a linear operator. Data $P(y_j)$ at spacing Δy can be inverted to give the source distribution $F(r_i)$ by

$$F(r_i) = \frac{1}{\Delta x}\sum_{j=0}^{\infty} D_{ij} P(y_j) \tag{3.3}$$

where $y_i = i\Delta y$ is the distance from the centre of the object. The linear operator coefficient D_{ij} is independent of the data spacing Δy. Once the D_{ij} coefficients are calculated, they can be applied to any form of the projection data.

There are a number of methods to obtain D_{ij}; we chose a method called “Three point Abel” [36]. After performing the integrals analytically and doing some algebra we can see that the Abel inversion operator is dominated by the diagonal terms and the just above diagonal terms, that have opposite signs. This indicates that D_{ij} acts as a differential operator on the $P(y_i)$, which is localized in the region of y_j. Finally we used a (5×5) Gaussian filter to remove noise from the output data.

3.2.7 Vibrational Temperature Calculation

The spectral intensity for an electronic transition, or the integrated intensity because of related rotational and vibrational transitions depends highly on the flame temperature T and the number of combustion radicals N, and can be expressed as,

$$I = h\nu NgA \exp^{\frac{\left(\frac{-E}{kT}\right)}{Q(T)}} \qquad (3.4)$$

h	Plank's constant
v	frequency
N	number density
g	statistical weight of the excitation level
A	transition probability for the spontaneous emission
E	upper level energy
k	Boltzmann's constant
$Q(T)$	partition function

In addition to infrared thermography and thermocouples the flame temperature in this study is determined by taking the ratio of C2 emission intensities obtained at two wavelengths, 470 and 515 nm. The intensity ratio I_1/I_2 of the two vibrational bands is given by equation 3.5. The instrument constant, p, was determined by the calibration based on the temperatures measured at two spatial points in the flame by means of a Pt/Pt-13% Rh R-type thermocouple.

$$\frac{I_1}{I_2} p = \frac{\sum_i v_i A_i \exp(-E_i / kT)}{\sum_j v_j A_j \exp(-E_j / kT)} \tag{3.5}$$

The properties of the C_2 vibrational bands are shown in Table 3.1. In this table λ is wavelength, *v'* and *v''* are vibrational quantum numbers, E designates the energy associated with the vibration and A is the relative transition probability.

Table 3.1 Physical properties of the C_2 vibrational bands [37]

λ (nm)	*v', v''*	*E* (erg)	*A*
468.48	4, 3	7.67×10^{-13}	0.358
469.76	3, 2	6.02×10	0.477
471.52	2, 1	4.34×10	0.318
473.71	1, 0	2.63×10	0.637
509.77	2, 2	4.34×10	1.000
512.93	1, 1	2.63×10	1.000
516.52	0, 0	0.88×10	1.000

The intensity ratio, I_{515}/I_{470}, of the two vibrational bands of C_2 at 515 and 470 nm respectively can be expressed as,

$$\frac{I_{515}}{I_{470}} p = K \exp(E_{470} - E_{515}) / kT \tag{3.6}$$

Where, *K* is the ratio of the term *vgA/Q(T)* (this ratio is almost constant at temperatures below 2500K) [38-40].

3.2.8 Thermocouple Temperature Measurement

Also part of this study is the measurement of the mean temperatures, fluctuating temperatures, and probability density distribution of temperatures. These temperature signatures influence NO_x formation, emissions of CO and UHC, and smoke.

Measuring local temperatures in the flame and processing the data is how temperature measurements are performed. The resulting temperature is an indicator for the occurrence of the reaction. By measuring the temperature one can produce mean and fluctuating temperature maps provided the data are obtained and recorded at high frequency. In the present study the frequency response was extended to about 1kHz using computer compensation technique [12]. The temperature plots show the regularity of the thermal flow field, and the chemical actions at different areas. Therefore it is very important to have exact knowledge about the occurring temperature in a combustion process.

The temperature setup has three major components. They are a micro-thermocouple, an amplifier to boosts the thermocouple signal, and a personal computer that stores and preprocesses the temperature data as it is being taken. Final data processing takes place on a workstation using a program written in IDL (Interactive Data Language) that works out the characteristic mean temperatures, thermal stratification characteristics, and turbulent time scales within the flame.

Previous studies have shown that in a high swirling flame temperature, fluctuations can arise up to 5-kHz. The thermocouple in use, in this study for local flame temperature, is able to resolve a wide range of temperature fluctuations. The temperature measurements recorded with a thermocouple show only average temperatures instead of the more desired maximum temperatures. Therefore, the raw temperature data has to be compensated for thermal inertia effects of the used thermocouple.

Kunugi and Jino [41] first conducted compensated temperature measurements. Since then, this technique has been successfully used and refined by various researchers, Gupta et al [42], Heitor et al [43], and Miles et al [44] are a few. The method described below is adapted from work done by Marshall [12]. The basic nature of this method is the suitable correction for the thermal inertia of the thermocouple. All implementations of the compensation technique attempt to correct for the thermal inertia effect in some manner. Not all measurement techniques and correction methods of this effect are the same. The condition and the response limitations of the thermocouple can be demonstrated by carrying out an energy balance on the thermocouple bead as shown in figure 3.5:

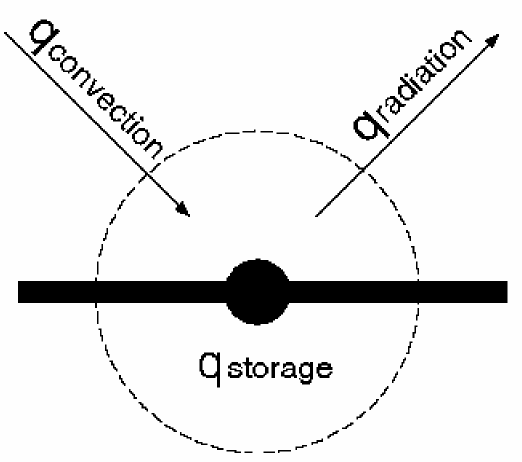

Figure 3.8 Energy Balance of the Thermocouple

There are three types of heat transfer present in this balance. The means by which the transfer of heat takes place between the probe and the environment are radiation, convection and conduction. Under the assumption that the conduction heat loss of the wire is insignificant [45] the balance can be written as:

$$q_{st} + q_{conv} - q_{rad} = 0 \tag{3.7}$$

q_{st}	heat storage
q_{conv}	convection heat transfer
q_{rad}	radiation

The heat storage is given by the term:

$$q_{st} = m \cdot c_P \cdot \frac{dT_b}{dt} \tag{3.8}$$

m	bead mass
c_p	specific heat
T_b	bead temperature

The convection heat transfer can be expressed as:

$$q_{conv} = h \cdot A_{bead} \cdot \left(T_g - T_b\right) \tag{3.9}$$

h	convective heat transfer coefficient
A_{bead}	thermocouple bead surface area
T_g	real gas temperature

The radiation is defined as:

$$q_{rad} = A_{bead} \cdot \sigma \varepsilon \cdot \left(T_b^{\ 4} - T_s^{\ 4} \right) \tag{3.10}$$

σ	Stephan-Boltzmann constant ($1.38066 \cdot 10^{-23}$ J K^{-1})
ε	emissivity
T_s	surrounding temperature

Formation of the equation after substitution of all the energies can be found in work done by Archer [46]. As a consequence of the radioactive outflow and the thermocouples restricted response time the gas temperature T_g varies from the bead temperature T_b. To describe the complete thermocouple system now just the time constant τ is required, which can be determined from a measured temperature decay curve.

This curve could be categorized by the function:

$$T(t) = T_{initial} + \Delta T \cdot e^{-\frac{t}{\tau}} \tag{3.11}$$

$$\Delta T = T_{final} - T_{initial} \tag{3.12}$$

T_{final}	measured final temperature
$T_{initial}$	measured initial temperature
t	time

Equation 3.11 shows the time constant as the period of time held to decline the temperature by 1/e on the decay curve.

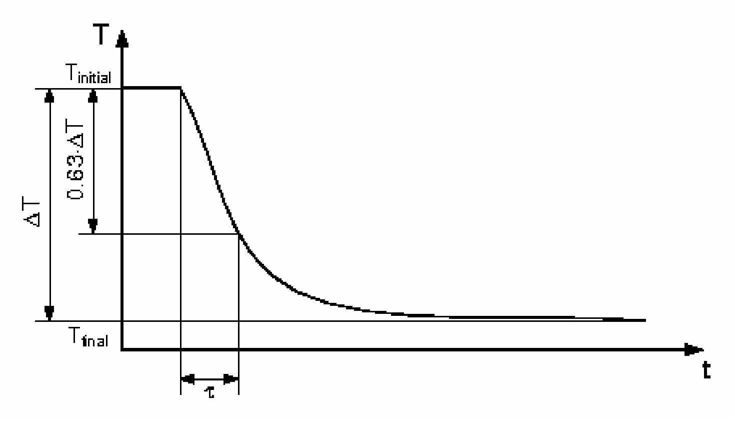

Figure 3.9 Temperature Decay Curve

As stated earlier the temperature setup has many components. It is comprised of a thermocouple probe, a high frequency amplifier (Analog Devices 5B40, band width = 10-kHz, amplification = 100) with an independent power supply model #025-15651 (5V, 1.2A) and a personal computer (Pentium II, 233-MHz, 96-MB RAM, 8.4-GB HD) with a data acquisition board, (Data Translation DT2801).

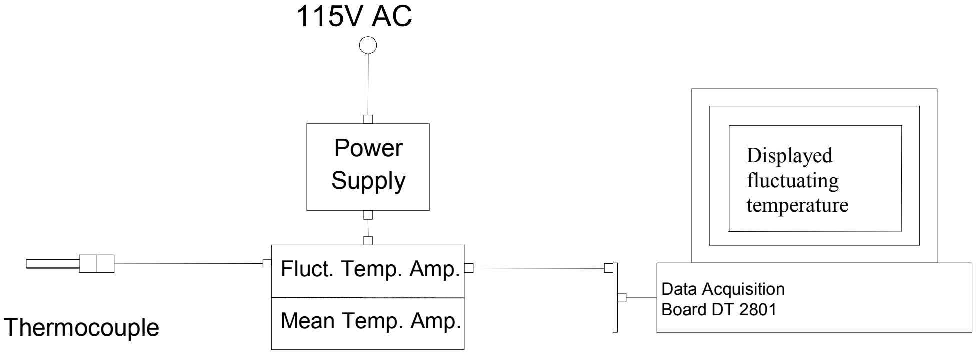

Figure 3.10 Sketch of the Temperature Measurement Setup

An incomparable temperature measurement method is used to earn detailed turbulent temperature information of the flame. In use with this technique is a micro-thermocouple probe. The thermocouple wire has a diameter of 50μm or .002". This wire size was chosen because of its ability to withstand the flow drag within the flame while minimizing flow disturbances. This probe has a low response time to turbulent temperature fluctuations within the flame. Frequency compensation is used to further reduce this response time. The determination of the time constant assists in compensation of the thermocouple frequency and the effects of thermal inertia. Since there is a high pulsating temperature signal, as mentioned earlier one can obtain characteristic mean temperatures, power spectra stratification characteristics and turbulent time scales inside the flame. The information expressed by this data is substantial for ascertaining the combustion process in these extremely turbulent flames. The high frequency temperature measurements are obtained with a type R micro- thermocouple probe (OMEGA P13R-002-8), as shown in figure 3.11:

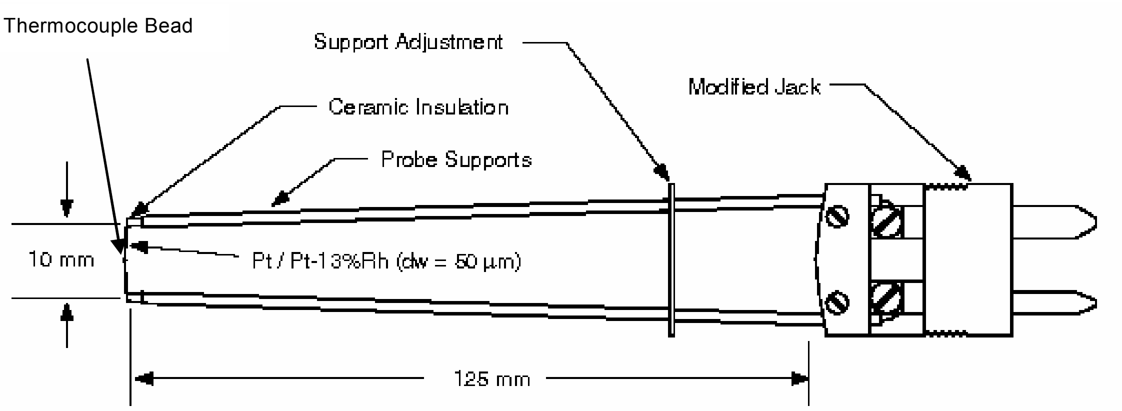

Figure 3.11 An Illustration of the Thermocouple Probe [12]

The probe operates with a Pt/Pt-13% Rh R-type thermocouple with a wire diameter of 50-µm, model P13R-002, the beaded junction of the thermocouple is suspended between two 1.6-mm diameter steel supports. They are ceramic tubes placed inside the steel supports between the thermocouple wire and the supports. The spacing between these supports is adjusted and fixed in place by a modified thermocouple jack. This jack is described in Burner Geometry Effects on the Emissions of a Variable Geometry Swirl Combustor [47].

The R-type thermocouples, manufactured by Omega Engineering Inc., can be used up to a maximum temperature of around 1750 °C. The diameter of the bead is about three times (about 150-µm) that of the wire diameter (about 50-µm).

The fluctuating temperature amplifier is an Analog Device 5B40, which boost the thermocouple signal by the factor of 100. The bandwidth is 10-kHz, which permits resolving small turbulent time scales in the flame.

The mean temperature amplifier is situated in a metal box together with the fluctuating temperature amplifier. This one is an Analog Device 5B37 (amplification = 100) with a bandwidth of just 3-Hz and is only needed for the calibration of the thermocouple.

The two amplifiers are powered by independent power supply model 025-15651 with 5 volt and 1.2 ampere in order to decrease the electronic noise level in the system.

In order to achieve dependable experimental results, calibration of the thermocouple is essential. The calibration discussed below is actually only a DC offset adjustment, which is mathematically described as a fourth order polynomial with special roots for three different ranges of the signal. Only the DC offset of the thermocouple signal needs to be calibrated.

One way to perform this calibration is to arrange a reference measurement at the ice point of water with a similar thermocouple.

Another way is to use an amplifier that utilizes a so-called electronic ice point. This is an electronic device, which provides all the essential compensations with no need of a reference thermocouple or ice water.

The calibration setup is comparable to the fluctuating temperature setup except for the reference thermocouple. A second thermocouple is connected to the mean temperature amplifier, which utilizes an electronic ice point in contrast to the fluctuating temperature signal conditioner. The output of the amplifier is coupled with another analog input channel of the data acquisition board.

The two thermocouples are positioned together (with the ends of each probe approximately two centimeters apart) to guarantee that they measure the same temperature. The computer acquires the analog voltage outputs of the thermocouple amplifiers and transforms the voltages into temperatures using the given calibration function of the used thermocouples.

In this experiment the adjustment of the DC offset is made with the Visual Basic Program, which is also used to archive and process the experimental data. A copy of this program can be found in Appendix C.

The program keeps on subtracting from the acquired voltage of the fluctuating temperature amplifier until the two transformed temperatures are equal. Once the temperatures are equal one obtains the DC offset. One can therefore determine if recalibration is necessary based on the size of the DC offset. One calibrates until it, the DC offset, reaches the point with an acceptable (very small) divergence. The DC offset (ΔDC) is stored to a variable, which will be subtracted from the temperature, calculated out of the output signal of the fluctuating temperature amplifier. For the measurement of the DC offset, the calibration setup as shown in figure 3.12 is used:

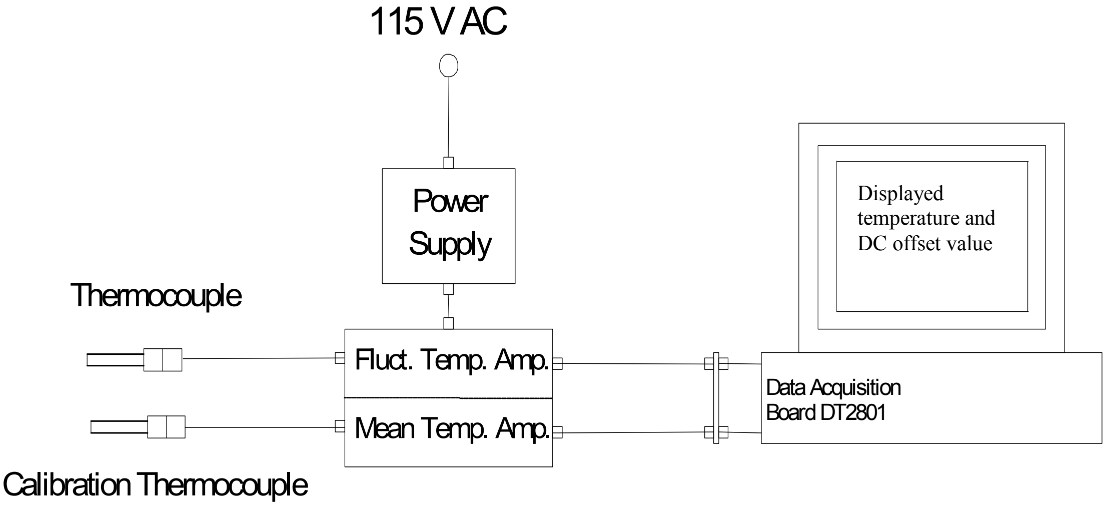

Figure 3.12 Sketch of the Calibration Setup

3.2.9 Thermocouple Time Constant Measurement

The time constant measurement is designed for analyzing the reaction attributes of the thermocouple. A schematic diagram of the time constant setup is illustrated in figure 3.13.

The time constant measurement setup is comprised of the mentioned temperature setup, a signal generator, a heating power source and a special planned circuit for carrying out an abrupt switching between heating and measuring of the thermocouple. The circuit shown in figure 3.14 executes the existent switching.

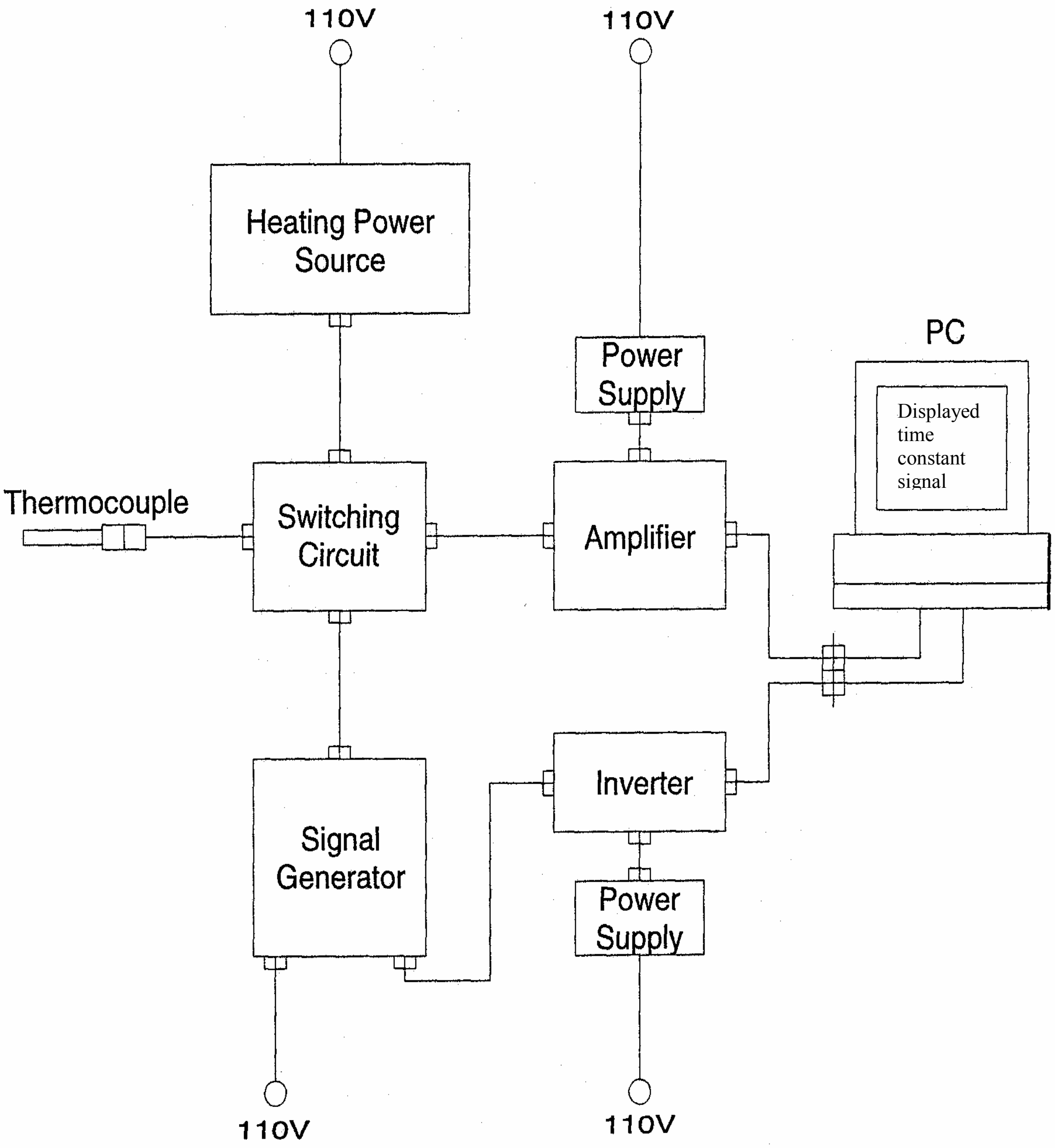

Figure 3.13 Sketch of the Time Constant Measurement Setup

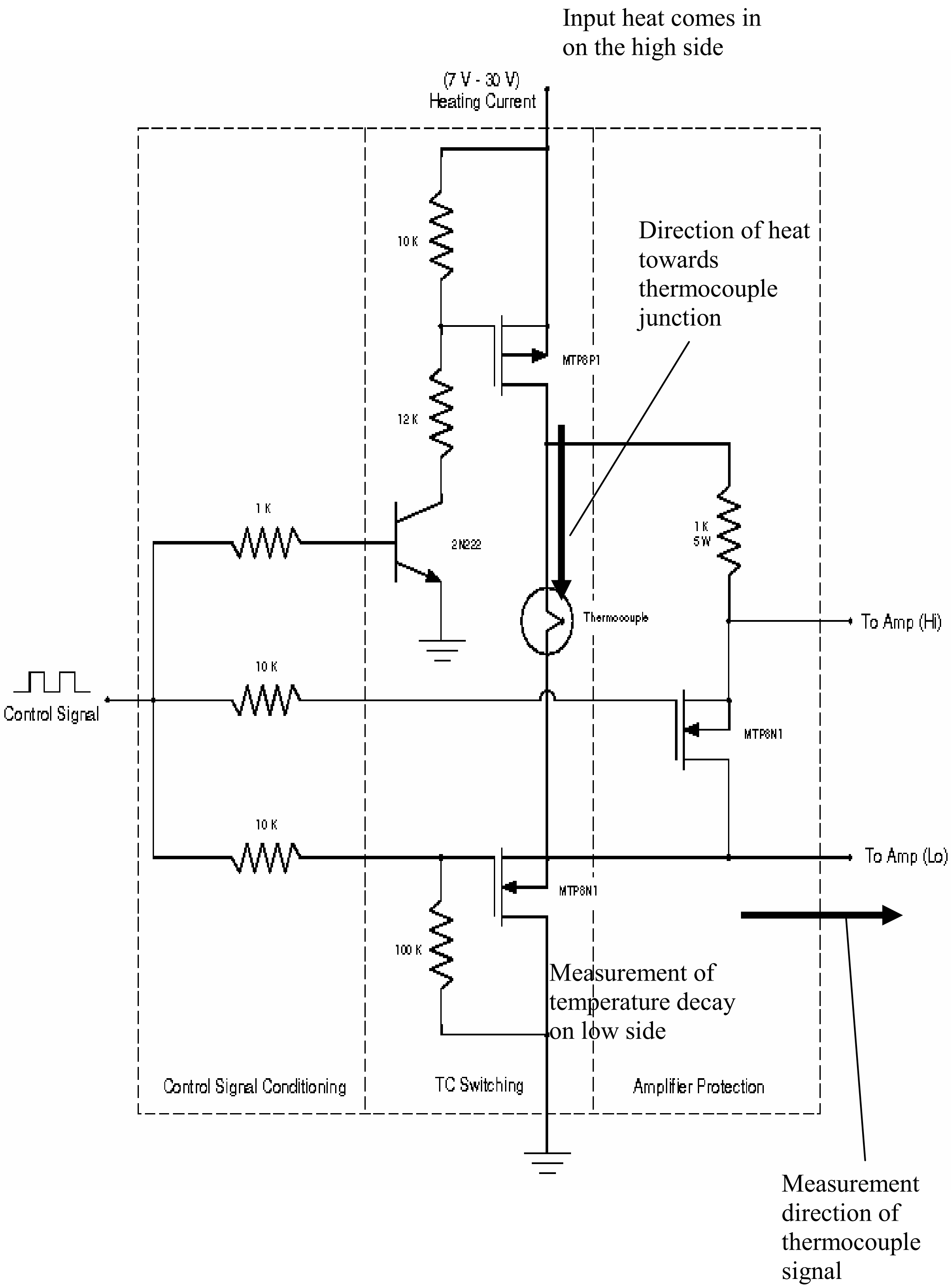

Input heat comes in on the high side

Direction of heat towards thermocouple junction

Measurement of temperature decay on low side

Measurement direction of thermocouple signal

Figure 3.14 A schematic diagram of the switching circuit for heating and measuring of the thermocouple [12]

During the heating period the square wave is high and all the transistors overfill causing the heating stream to flow and demanding a 20-mV signal departing out of the amplifier. During cooling the additional trigger swaps from high to low and causes the PC data acquisition board to register the temperature decay sample. The square wave signal is low during this period and all of the transistors are held open. The thermocouple is separated from the heating circuit and the actual voltage corresponding to the thermocouple junction temperature is recorded. Detailed information is available in Marshall [12].

The switching of the circuit is controlled by a square wave of the signal generator (3025 Sweep/Function Generator, Dynascan Corporation). It also triggers the DT2801 data acquisition board.

The signal generator is a Dynascan Corporation Model 3025 Sweep/Function generator. The high output at the front plate is connected to the switching circuit. This voltage is set to 10-volt (±0.2V) during the experiment. The SYNC-output at the backside is utilized to trigger the data acquisition board with a voltage of 3.8V.

The calibration procedure is completely different for the time constant measurement because it has to be guided under normal experiment conditions. That means the switching circuit must work and the thermocouple has to be connected in cycles with the amplifier and the heating power source. Therefore the output frequency of the signal generator has to be decreased down to 0.05-Hz. In this case the time that the thermocouple is coupled to the amplifier is long enough to manage an ordinary calibration.

It is absolutely necessary that the time constant be recorded at exactly the same position as the raw temperature sample. The number measured points for the time constant are less than the number of measured temperature points. This is true because the sampling of τ is required at every other location of the r and z direction because of the small changes of the time constant values at adjoining positions. The time constant at each point is obtained by interpolating the captured data with a program named ‘tc.pro’, written in IDL.

When the voltage of the square wave from the heating current is zero, the samples of the decay have to be taken. At this moment the thermocouple is connected to the amplifier. For the triggering of the data acquisition board a supplementary inverter has to be connected in order to invert the square wave signal for the board.

With the signal generator the heating period has to be adjusted to 250 ms (because of the resolution of the data acquisition board) and so the time constant is calculated from the middle of 300 sweepings. This long period allows the measurement to archive a smoother curve for the time constant. This was found necessary due to fluctuations in the flame.

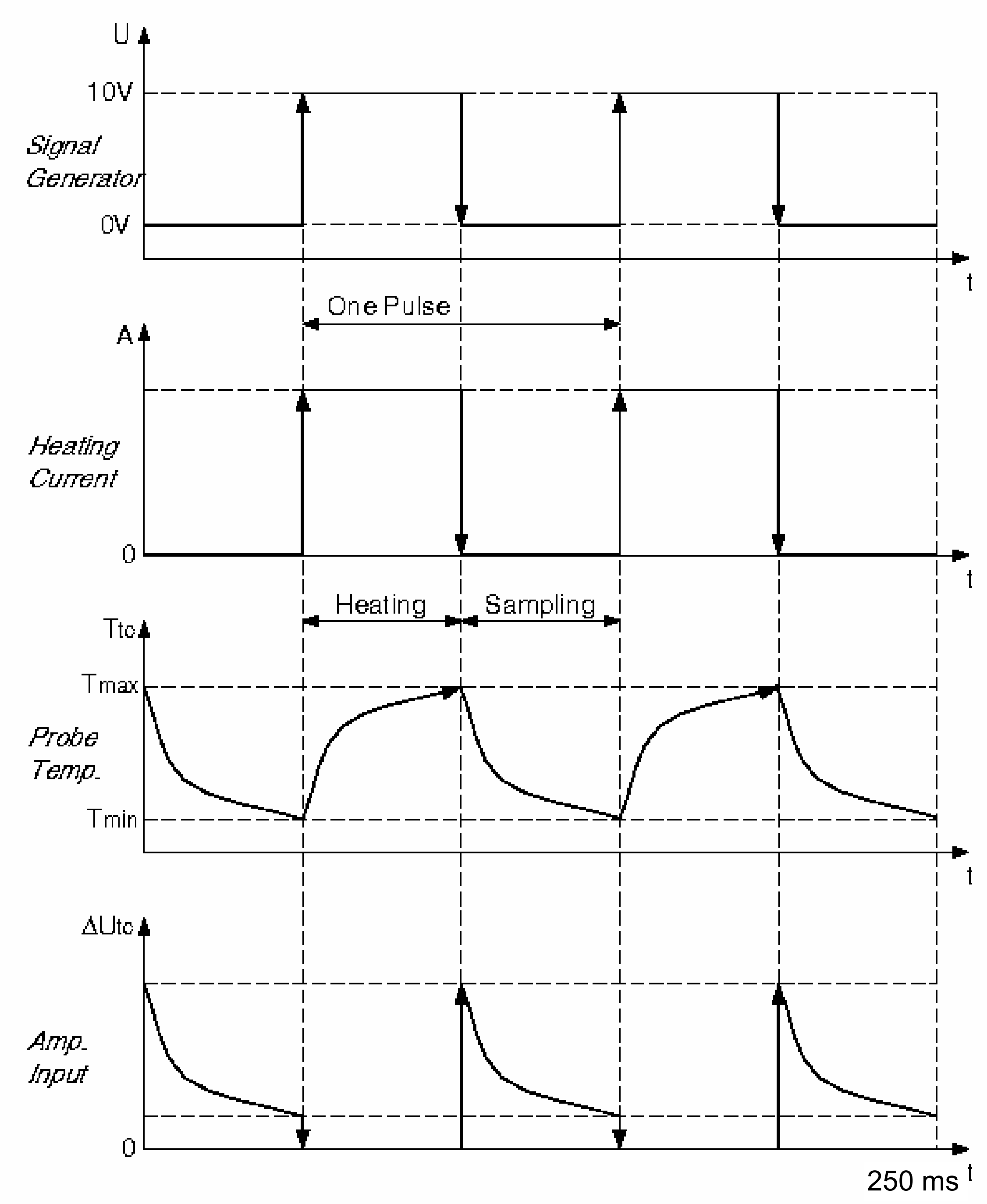

Figure 3.15 Operation of the Time Constant Measurement

The heat burst and the data acquisition is managed by the square wave of the signal generator. The thermocouple is connected sequentially with the amplifier and the power supply. One oscillation contains the heating of the thermocouple, detaching it from the power supply, adjoining it with the data acquisition system and the cooling period. The average of each decay curve is finally saved on the hard drive for further calculation. An example file name is 1tc0000.txt. The first number stands for the case, with tc designating time constant, and the four digits standing for the position.

3.3 Experimental Diagnostics and Techniques Error Estimation

3.3.1 Error Estimation in Particle Image Velocimetry

The most common sources of error in the PIV results that should be considered can be divided into the generic error originating from the experiment itself, such as, particle lag or thermophoresis, and image-processing errors. The sampling frequency for the PIV system is 5 Hz and the camera is able to expose two consecutive images within 5 μs.

PIV methods measure the Lagrangian velocities of particles and therefore, are based upon the assumption that the particles follow the surrounding fluid motion. According to the analysis of Raffel [48], the relaxation time of a particle to a step change in the fluid velocity is given as

$$\tau_s = d_p^2 \frac{\rho_p}{18\mu} \tag{3.13}$$

τ_s relaxation time

d_p	particle diameter
ρ_p	particle density
μ	dynamic viscosity

Using the mean particle size of 5 μm, a particle density of 2500 kg/m^3, and fluid (air) dynamic viscosity of 184.6e7 kg/m-s and 611.0e7 kg/m-s for temperatures of 300 K (non-reacting) and 1700 K (reacting) respectively the relaxation time can be calculated. The non-reacting relaxation time is 188 μs and the reacting relaxation time is 56 μs. The calculated relaxation times illustrate adequate fast particle response to gas velocity changes.

A cross-correlation function is used to process the captured particle images. The interrogation window size is 24 x 24 pixels with a 50% overlap in each direction. The resulting spatial resolution is approximately 1.6 x 1.6 mm. The uncertainty in the velocity computations from the cross-correlation algorithm is less than 2% and uncertainty for the derived strain and vorticity fields is less than 2.4% [49]. Geometrical calibration introduces an uncertainty of less than 0.6%. This gives you a final velocity uncertainty of less than 2.4% and an uncertainty for the derived quantities of less than 3.6%. The thermophoretic forces that the particles experience are in a direction opposite to the temperature gradients in the flame. The effects of thermophoresis can be quantitatively estimated with instantaneous temperature field data. However, the thermophoresis effects on the particle motions are negligible in high speed and turbulent flows [50], such as the strongly swirling flows in the present study. This is verified by the instantaneous particle images showing adequate particle density in the measured flow region.

3.3.2 Error Estimation in Optical Emission Spectroscopy

The initial 2-D images of flame radicals are integrated images and not cross-sections. Therefore the effect of integration can distort the comparison of relative intensity for the 2-D images. This is due to the line of sight not being thin for the investigated co-axial flames with cylindrical shape. The captured intensity is approximated to be within 5% of the actual intensity.

3.3.3 Error Estimation in Infrared Thermometry

The foci for sources of error with the infrared camera measurement technique are the value of the supplied emissivity and the fact that the detected infrared signal is long wave range. The supplied emissivity is based on simplified analysis for flame temperature that assumes complete combustion. Also only two compounds CO_2 and H_2O are taken into account when partial pressures are determined so the emissivity can be calculated. The long wave range of detection acquires a lot of background radiation which can lead to an over valued net radiance. The averaged images are integrated images of a cylindrical shape, which distorts relative comparison. The captured intensity is approximated to be within ±2% of the actual intensity according to camera specifications.

3.3.4 Error Estimation in Thermocouple Temperature Measurement

The error associated with the compensated thermocouple measurements were first discussed by Marshall [12]. The errors are due to flame asymmetries, mechanical limitations of the probe, electrical noise, and assumptions associated with the time constant measurement and compensation. In this study the flame asymmetries are not a source of error because temperature sampling points are not restricted to one-half of the flame. Probe disturbances are considered negligible due to no visual evidence of flame anchoring with the used probes. Catalytic effects are also considered negligible due to the adverse of effects that can be created with attempts to correct for this source of error.

Errors associated with the electronic noise, quantization, and polynomial relationships between junction voltage and temperatures are easily quantified. These errors are determined to be less than ±3 K in the temperature range of interest.

The largest source of error results from the measurement and approximation of the local time constant. This is detailed in Marshall [12]. Even with the associated errors, simplicity of implementation and utility of results make the thermocouple temperature measurement and attractive diagnostic.

3.3.5 Error Estimation in Gas Sampling Emissions Measurement

Sample collection is the source of error associated with gas sampling emissions measurement. The inability of the probe to extract gas from the exact location at which it is positioned compromises the accuracy of the measurements. It is not appropriate to think of gas sampling as a point measurement but more of an average measurement over a region. In this study it was decided that the emissions would be sampled at an area, which would represent the centerline of the flames.

Reactions could also continue within the probe if inadequate water flow is present at the probe tip. This would cause the sampling of product gas concentrations, which are not reflective of those present in the flame. The analyzer used in the study is quite accurate. It has margins of error less than ±5 % given by its specifications . Reasonable conclusions concerning the relative characteristics of the flames studied can be made due to the systematic nature of the associated errors. The measured values are within 10% of the actual values.

Chapter 4: Investigative Methodology

To properly study flames a method for investigating them needs to be devised. A set of thoughtfully designed experiments is conducted to examine the differences in morphology and characteristics of unconfined and confined swirling flowfields with varying radial distribution.

Before experimentation takes place, the governing parameters need to be established. To fully understand the effects that confinement and radial swirl distribution has on a lean direct injection (LDI) flame these governing parameters need to be manipulated. Once a set of constant and variable conditions is conceived, a way to evaluate performance is necessary.

4.1 Experimental Methods and Conditions

The governing parameters can be placed into two categories. The categories are aerodynamic and geometric inlet parameters. In this investigation the geometric parameters are not taken into consideration. The aerodynamic parameters in question are given in table 4.1.

Table 4.1 Aerodynamic Governing Inlet Parameters

Inlet Parameter	Symbol	Description
Equivalence Ratio	ϕ	Normalized measure of the fuel/air ratio
Momentum Ratio	M	Measure of the relative jet strength in the axial direction between the annulus 1 and 2 jets
Swirl Number	S	Measure of the proportion of tangential to axial momentum in the annulus 1 or 2 jet

Aerodynamic parameters have an advantage over geometric parameters. Aerodynamic parameters are easier to apply to practical applications because they affect gas flows. Therefore they are easier to change and adjust.

The equivalence ratio is a substantial aerodynamic parameter. It is defined as the ratio between actual fuel/air ratio to the stoichiometric fuel/air ratio. It can be expressed by the following equation:

$$\Phi = \frac{\left(\frac{\dot{m}_{fuel}}{\dot{m}_{air}}\right)_{actual}}{\left(\frac{\dot{m}_{fuel}}{\dot{m}_{air}}\right)_{stoichiometric}} \tag{4.1}$$

$$\dot{m} = \rho \cdot \dot{V} \tag{4.2}$$

$\dot{m}$	mass flow rate
ρ	fluid density
$\dot{V}$	volume flow rate

The equivalence ratio is also used to denote the type of combustion taking place. The distinct forms are lean combustion ($\phi < 1$), rich combustion ($\phi > 1$), and stoichiometric combustion ($\phi = 1$).

During this study the equivalence ratio is kept constant. The chosen flow conditions dictate an inlet equivalence ratio of 0.625.

The relative jet strength is controlled by the flow distribution between annulus 1 and annulus 2. The momentum ratio, M, is used to quantify this relative jet strength. The momentum ratio can be defined by the following equation:

$$M = \frac{\left[\left(\rho_{air} \cdot V_{air}^{2}\right) \cdot A\right]_{an1}}{\left[\left(\rho_{air} \cdot V_{air}^{2}\right) \cdot A\right]_{an2}} \tag{4.3}$$

ρ_{air}	density of the air
V_{air}	velocity of the air
A	area of the annulus

It is obvious that the measurement of the volume flow in each annulus and the knowledge of the densities are substantial for the calculation of the momentum ratio. It is possible to change the equivalence ratio without making significant changes to the momentum ratio, which is one important parameter to describe the aerodynamic conditions. Also the momentum ratio is known for characterizing the global flame structure. The momentum ratio can be used to fundamentally change flame behavior, depending on the other governing parameters.

In this investigation the momentum distribution are governed by certain parameters. These parameters are the annulus 1 swirl number, the annulus 2 swirl number, and the momentum ratio. The momentum ratio between annulus 1 to annulus 2 is held constant throughout this study.

The swirl number is another important aerodynamic parameter. The distribution of axial and angular momentum (the combined/overall swirl number) can be adjusted by changing the swirler vane angle. It can also be adjusted by changing the flow rate in each annulus but as stated earlier this is held constant in this study. The swirl number has traditionally been used to quantify the relative proportions of angular and axial momentum. The combined swirl number does vary in this investigation. It is defined by the following equation [8].

$$S=\frac{M_{\varphi}}{R_0 \cdot M_X} \tag{4.4}$$

R_0	characteristic length (nozzle radius)
M_{φ}	angular momentum flux
M_x	axial momentum flux

In the above equation, equation 4.4, the two momentum fluxes are defined mathematically as

$$M\varphi=\int w \cdot r \cdot \rho \cdot u \cdot 2 \cdot \pi \cdot r \cdot dr \tag{4.5}$$

$$M_X=\int u \cdot \rho \cdot u \cdot 2 \cdot \pi \cdot r \cdot dr \tag{4.6}$$

w	tangential component of the velocity
u	axial component of the velocity
ρ	fluid density

Strong swirling flows are usually characterized with swirl numbers of 0.6 to 0.9. In this study, swirl numbers are initially calculated using the approximations given by Gupta, A.K. [8].

$$S=\frac{2}{3}\cdot\tan\left(\alpha\right) \tag{4.7}$$

S	swirl number
α	swirl vane angle

$$S=\frac{2}{3}\cdot\left[\frac{1-(d_h/d)^3}{1-(d_h/d)^2}\right]\tan\alpha \tag{4.8}$$

S	swirl number
α	swirl vane angle
d	nozzle diameter
d_h	hub diameter

Equations 4.7 and 4.8, both are equations that can be used to approximate the swirl number. Equation 4.8 is used for swirl number calculations reported in table 4.3 because the swirlers used are not hub less. Because the equation is only an

approximation and does not denote a difference between co- and counter- swirl, measures will be taken to further quantify the actual swirl number from obtained data.

The annulus 1 swirler predominately governs the local and global flame structure once the outer swirler stabilizes the flame. The annulus 1 swirler is held constant for this investigation. The annulus 2 swirler is varied so that the effects of co and counter swirl can be quantified and compared. The following tables give an overview of the conditions under which flames are studied. The common parameters and the varying parameters are shown for the different flame cases. Also shown are the flow meter conditions for annulus 1, annulus 2, and the central pipe.

Along with the above mentioned parameters the flames under investigation are subject to a fixed heat loading input, $\dot{E}_{in}$. The heat loading is fixed so that the thermal effects can be characterized by the varied variables. Heat loading is given by the following formula below [12]. For the experimental conditions of this study, the heat loading is approximately 33kW.

$$\dot{E}_{in} = \rho_{fuel} Q_{fuel} LHV \tag{4.9}$$

$\dot{E}_{in}$	heat loading
ρ_{fuel}	density of fuel
Q_{fuel}	flowrate of fuel
LHV	lower heating value (fuel)

Table 4.2 Experimental Parameters (held constant)

Common Parameters	
Axial Momentum Central Pipe	$M_{CP} = 300 \frac{\text{lbm} \cdot \text{ft}}{\text{min}^2}$
Axial Momentum Annulus 2	$M_{An1} = 1500 \frac{\text{lbm} \cdot \text{ft}}{\text{min}^2}$
Axial Momentum Annulus 1	$M_{An2} = 2163 \frac{\text{lbm} \cdot \text{ft}}{\text{min}^2}$
Momentum Ratio (M_{An1}/M_{An2})	M = 0.693
Equivalence Ratio	$\Phi = 0.625$
Fuel	Propane

Table 4.3 Experimental Parameters (varied)

Varied Parameters			
Flame	Swirlers	Swirl Numbers calculated from eqn. 4.8	Condition
1	Annulus 1 45^O Annulus 2 50^O	$S_{An1} = 0.78$ $S_{An2} = 1$	unconfined
2	Annulus 1 45^O Annulus 2 -50^O	$S_{An1} = 0.78$ $S_{An2} = 1$	unconfined
3	Annulus 1 45^O Annulus 2 50^O	$S_{An1} = 0.78$ $S_{An2} = 1$	confined
4	Annulus 1 45^O Annulus 2 -50^O	$S_{An1} = 0.78$ $S_{An2} = 1$	confined

S_{An1} Swirl Number in annulus 1
S_{An2} Swirl Number in annulus 2

Table 4.4 Experimental Matrix and Flow Conditions; the numbers in parenthesis show the percentage of total flow in annulus

Conditions	Inner Swirler Vane Angle (degree), An. 1	Outer Swirler Vane Angle (degree), An. 2	Air Flow (scfm), An. 1	Air Flow (scfm), An. 2	Fuel Flow (scfm), central pipe	Reynolds Number		Equivalence ratio
						An. 1	An. 2	
Non-Reacting/ Reacting, Unconfined	45	50	10.52 (32%)	21.88 (68%)	0.8509	8100	7950	0.625
Non-Reacting/ Reacting, Unconfined	45	-50	10.52 (32%)	21.88 (68%)	0.8509	8100	7950	0.625
Non-Reacting/ Reacting, Confined	45	50	10.52 (32%)	21.88 (68%)	0.8509	8100	7950	0.625
Non-Reacting/ Reacting, Confined	45	-50	10.52 (32%)	21.88 (68%)	0.8509	8100	7950	0.625

4.2 Data Analysis Methods

The flowfield, combustion, and flame characteristics of interest have been identified as flame symmetry, flame stability, pollutant formation, flowfield dynamics, chemical behavior and mixedness. These characteristics can all be evaluated and compared with the help of certain measured quantities. A strongly swirling flame consists of two principal regions. These regions are the shear layer and the recirculation zone.

Very often one cannot take local direct measurements of combustion characteristics in these regions. It is possible to gain insight into these combustion characteristics from more readily measured quantities.

Direct flame photography will be used to evaluate global characteristics of the investigated flames. Particle Image Velocimetry (PIV) will provide information on instantaneous and mean velocities, turbulence characteristics, and strain rates. PIV will also help with determination of recirculation zone mass flow entrainment and calculated swirl numbers. These numbers will help quantify the varied swirl distribution and the role of confinement. To support the flowfield data, information on chemical and thermal behaviors will be obtained. Spatial distribution of CH, OH, and C_2 radicals will be imaged. CH and OH spatial distributions will provide a visual measure of heat release rate and markers of reaction zone and reaction rate. This is possible because chemiluminescence can be related to specific chemical reaction rates. The ratio of two wavelengths of the C_2 radical will be taken to produce vibrational temperature images that further quantify flame mixedness based on thermal field uniformity. Pollution formation will be evaluated from the emissions data of NO, CO and CO_2. The emission data will be correlated with flowfield, chemical, and thermal data.

Chapter 5: Results and Discussion

5.1 Direct Flame Photography

Direct flame photographs have been taken, in order to acquire information about global flame structure, flame stability and flame intensity.

Figure 5.1 shows a direct comparison of the two reacting unconfined flows. The flame on the left is the co-swirl configuration of 45/50 and the flame on the right is the counter-swirl configuration of 45/-50. All conditions are constant except for the variation in swirl distribution. The global features depicted in these photographs are an initial look into the effect of varying swirl distribution and swirl strength. It is generally believed that the swirl number has an important effect in the combustion process and that increased swirl number produces enhanced tangential momentum, which provides a better mixing between the incoming hot chemical reactants and the fresh fuel air mixture. The rapid mixing decreases flame length. It is interesting to observe that the flame lengths are comparable between the two reacting flows with the counter-swirl flame being slightly shorter. It is not thought that the swirl number is increased but rather the turbulence is increased in the counter-swirl case. Large tangential velocity gradients are a result of increased turbulence. The large gradients are an effect of the counter shearing forces produced from counter rotating inner and outer swirlers. The counter-swirl flame does produce a wider flame, which for the given burner geometry could be the representation of positive radial stretch as a result of the large tangential velocity gradients. This consequently would be reflected in the flame stretch rate, $K=1/A(dA/dt)$, (where A is the flame surface area and t is the time). This positive stretch increases the volumetric burning rate and shortens the flame height.

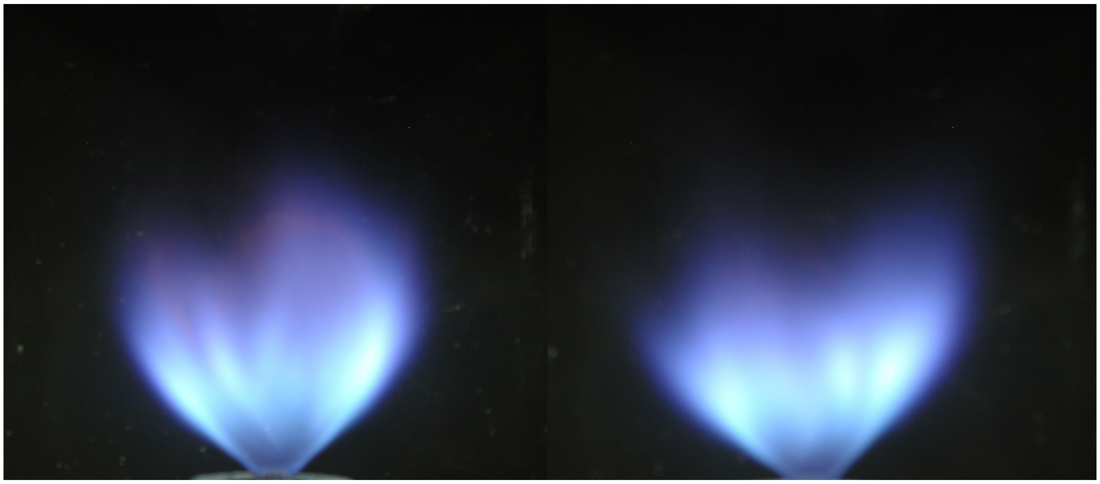

Co-swirl flame 45/50 Counter-swirl flame 45/-50

Figure 5.1 Flame photographs of co-swirl ($45^o/50^o$ case) and counter-swirl ($45^o/-50^o$ case) unconfined flames

Figure 5.2 is a photograph of co-swirl (45/50) confined flame. Confinement increased the overall luminosity of the flames. This increase in luminosity is attributed to the confined environment promoting richer burning of the fuel mixture.. With confinement air entrainment is reduced as compared to unconfined case to affect the local equivalence ratio throughout the flame environment. Also flame width is increased. This appearance of increased flame width shows the increased radial spreading attributed to confinement. The general trends and/or differences seen between co- and counter-swirl established in the unconfined direct flame photographs were also seen in the confined direct flame photographs.

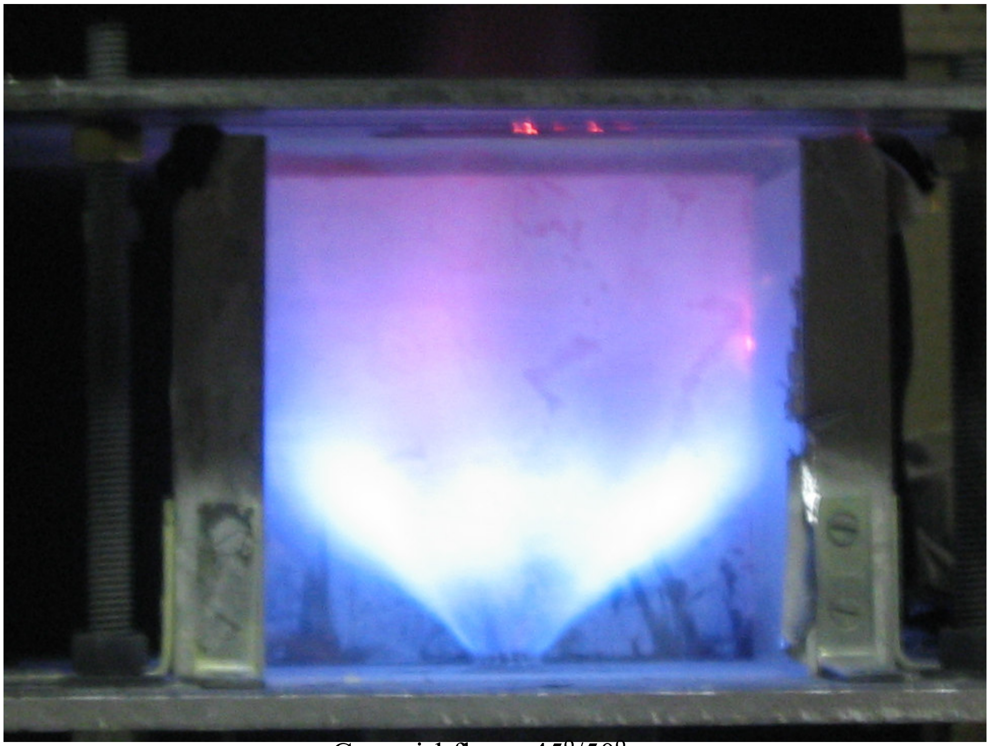

Co-swirl flame $45^o/50^o$

Figure 5.2 Flame photograph of co-swirl ($45^o/50^o$ case) confined flame

5.2 Particle Image Velocimetry

The mean velocity fields are determined from Particle Image Velocimetry (PIV) analysis of 250 instantaneous image pairs from two cameras for the unconfined flowfields. The two cameras allow for 3-D flowfields to be obtained which provides three components of velocity. The mean velocity fields for the confined flowfields are determined from Particle Image Velocimetry (PIV) analysis of instantaneous image pairs from one camera (2-D). The PIV data provided information on the mean and turbulence characteristics of the flow with varying shear flow conditions between inner and outer annuli of the burner. The horizontal bar above the figure shows the magnitude associated with the specific flowfield variable (i.e., axial, (v), radial, (u) or tangential velocity (w)). The unit of measure for the axes of the PIV images is millimeters. To provide a frame of reference for the images, it should be noted that the outer annulus swirler has an outer diameter of 62 mm and an inner diameter of 38 mm approximately. The inner annulus swirler has an outer diameter of 35 mm and an inner diameter of 18 mm approximately. The widest portion of the fuel injector has an approximate diameter of 19 mm. The base of the fuel injector head sits adjacent to the vanes of the inner annulus. The wall thickness of the hub of the inner annulus is 1 mm. The information and dimensions provided above help in relating the experimental burner and swirlers to the experimental flowfield data obtained here. The results are discussed below.

5.2.1 Unconfined Non-Reacting Flowfield Data

The results obtained show that the radial swirl distribution, co- or counter-swirl, influences the resulting unconfined non-reacting/isothermal flowfields. The co-swirl condition, figure 5.3 (45°/50°), provides a greater axial velocity for the outer annular flow or jet flow. The counter-swirl condition, figure 5.4 (45°/-50°), has lower jet flow velocity due to the counter shearing forces produced that destroy the momentum and velocity of the incoming jet flow at the boundary of interaction between the inner and outer annulus. Additionally, due to the differences of rotation imparted to the two fluid streams, the counter-swirl condition imposes a region of near zero velocity or stagnation between the inner and outer annulus flows. In the co-swirl condition, the two jet streams from the inner and outer annuli are rotating in the same direction and do not interfere to the as greatly with the fluids natural expansion and deceleration. The formed internal recirculation zones also vary with radial swirl distribution. Each swirl condition produces an internal recirculation zone that extends upstream to the top of the injector. The upstream origin of the internal recirculation zone does not seem to be a function of the swirl distribution in this study.. Since the observed flowfields are unconfined, the surrounding air plays a role in the internal recirculation zone formation. The counter swirl condition produces a wider internal recirculation zone with a greater reverse flow magnitude. Swirler interaction takes place at a distance downstream, which may enable for two separate tangential velocity decays to exist for a short time. This could account for the increased reverse flow velocity and wider internal recirculation zone. This does bear further study and closer examination of the raw data obtained for the counter-swirl flow. The impact of the co-swirl condition on the internal recirculation zone is observed to be the formation of a thinner zone with a smaller region of maximum reverse flow. The internal recirculation zone also has a more oval or circular shape for the co-swirl flow. The shape of the internal recirculation zone is the result of greater axial stretch (stretch along the direction of the flow) for the co-swirl flow.

The mean velocities are used to determine values of strain, axial , radial and shear. The axial strain is defined by the equation 5.1.

$$\varepsilon_y = \frac{dv}{dy} \tag{5.1}$$

ε_y	axial strain
v	axial velocity
y	axial direction

Figure 5.5 shows the axial strain contour plot for the non-reacting unconfined co-swirl case. The greater stretch or acceleration is seen in more elongated and greater area of positive high strain regions associated with the jet outflow. Also the co-swirl condition has a smaller area of high positive axial strain at the far downstream region of the internal recirculation zone. This contributes to the co-swirl internal recirculation zone being slightly thinner and having a more oval shape. In comparison, the counter-rotating swirl produces a wider internal recirculation zone with a larger region of maximum reverse flow. It is seen that the axial strain, figure 5.6 for the counter-swirl non-reacting unconfined case explains the wider internal recirculation zone and greater reverse flow magnitude. It has a larger area of positive high strain at the far downstream region of the internal recirculation zone, which explains its wider internal recirculation zone. It has a larger region of maximum negative axial strain within the internal recirculation zone which accounts for its greater reverse flow magnitude. Also seen in the axial strain contour plots are the reasons of quicker velocity decay for the counter-swirl case. Quicker velocity decay is the result of larger regions of negative axial strain, which indicate deceleration. In the jet outflow region the counter-swirl flow has smaller regions of positive axial strain. This also allows for quicker mixing between the annulus 1 and 2 flows and better diffusion of flow properties.

Looking at the beginning of the measurement region, where the inner and outer annulus air flow first start to merge and considering this point y_o , we can begin to examine why the counter-swirl condition enhances the internal recirculation zone. We can make the following assumptions in this plane: interaction of the air flows is negligible and the tangential velocity profiles emanating from the inner annulus swirler are identical for the co- and counter- swirl conditions. This is true because the inner swirler is kept constant. The radial profiles of tangential velocity generated by the outer annulus swirler are expected to be of the same shape, but have opposite sign. The tangential movement of fluid in axisymmetric flows induces centrifugal forces, which are balanced by a radial gradient of static pressure.

$$\frac{dp}{dr} = \rho * \frac{u_t^2}{r} \tag{5.2}$$

p	pressure
r	radius
ρ	density
u_t	tangential velocity (w)

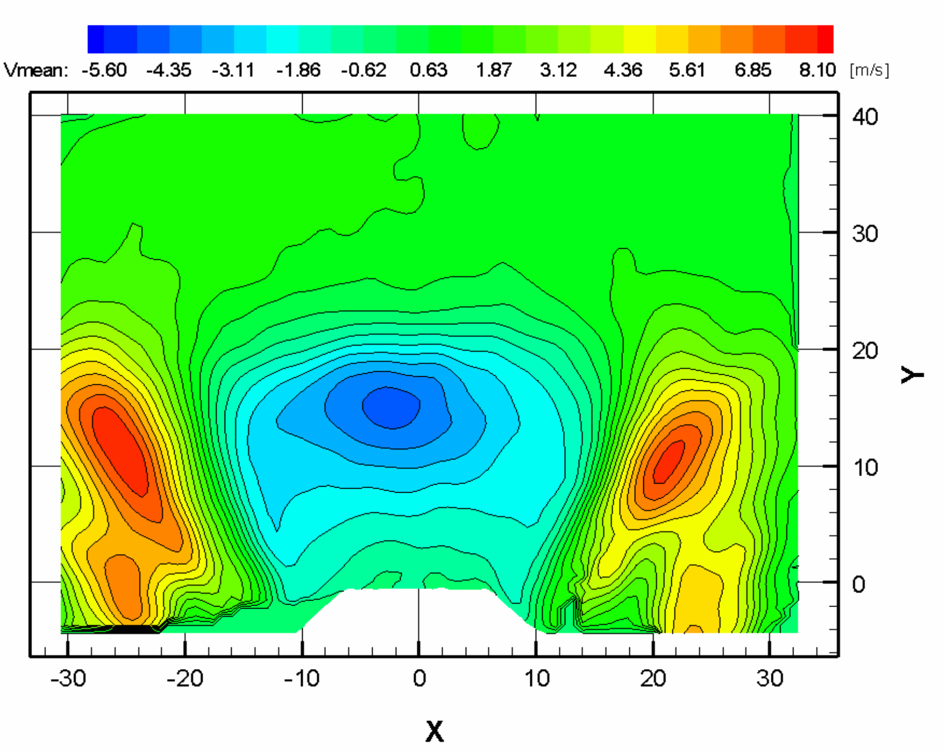

Figure 5.3 Axial Velocity contour plot, 45°/50° co-swirl case, non-reacting condition, unconfined

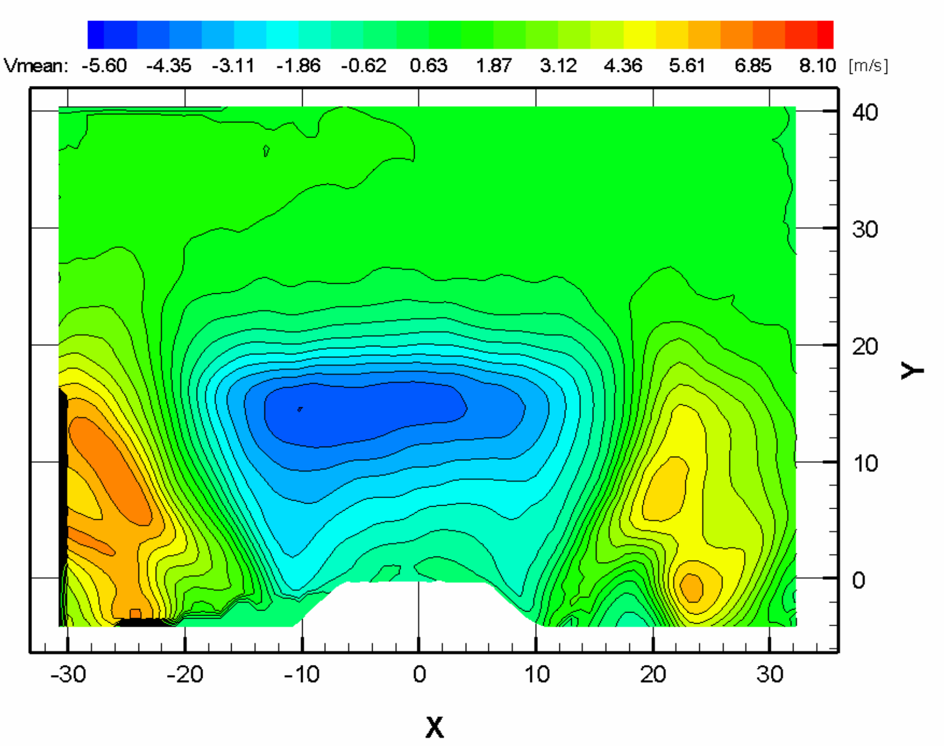

Figure 5.4 Axial Velocity contour plot, 45°/-50° counter-swirl case, non-reacting condition, unconfined

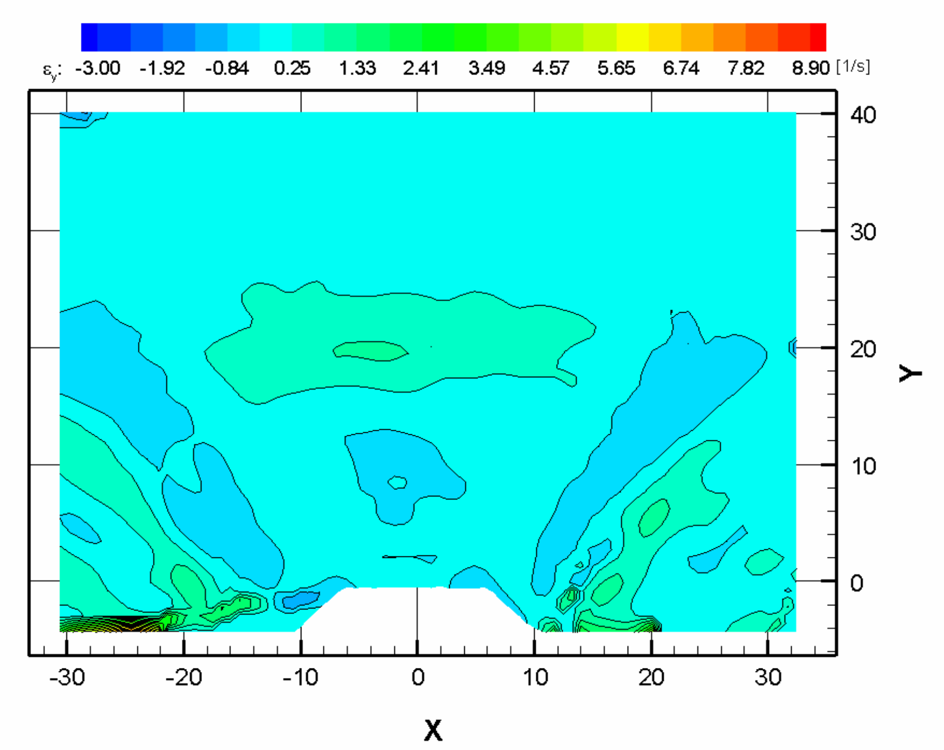

Figure 5.5 Axial Strain contour plot, 45°/50° co-swirl case, non-reacting condition, unconfined

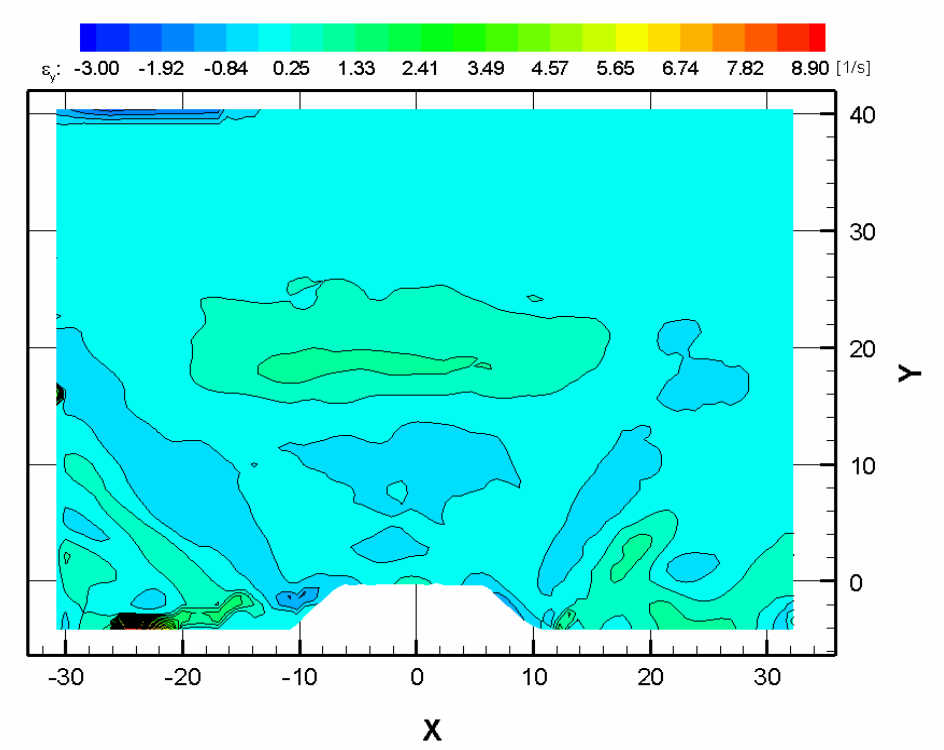

Figure 5.6 Axial Strain contour plot, 45°/-50° counter-swirl case, non-reacting condition, unconfined

At the axis of symmetry a minimum pressure is generated and towards the jet boundary a positive pressure gradient is generated. In the stated assumptions, the static pressure within the swirler exit plane at the location $y = y_o$, $r = 0$ ($x = 0$) is independent of the sense of rotation of the flows. Further downstream there is a decline of tangential velocity and the resulting centrifugal forces due to the divergence of the jet and conservation of angular momentum flux. This causes the static pressure to rise with increased distance from the swirler exit plane. A positive pressure gradient is generated along the axis. At a critical pressure a reversal of the flow velocity is achieved with negative axial velocities starting along the line of symmetry. The counter-swirl arrangement provides an additional decay of tangential velocity decay. This decay is superimposed on the effect of jet divergence as the inversely orientated fluxes of angular momentum from the inner and outer annulus partially compensate each other. The initial values of pressure at the center is zero in the plane of $y = y_o$ for both the co- and counter- swirl conditions so that the counter-swirl condition produces a stronger axial pressure gradient. This explains how the counter-swirl condition produces stronger reverse flow velocities. The result is not intuitive and needs further study.

The vortex center also is affected by the swirl distribution. The co-swirl condition based on the symmetry of the internal recirculation zone has a vortex center closer to the central longitudinal axis of the injector. The counter-swirl condition moves the vortex center further to the left of the central longitudinal axis of the injector. This movement of the vortex center is the result of hydrodynamic instabilities triggered by perturbations of the initial in-flow conditions and boundary conditions. Also, the condition of the swirlers helps to promote asymmetries in the data.

The shear strain distributions for the unconfined non-reacting flowfields are shown in figures 5.7 and 5.8. The equation used to derive the shear strain from the investigated flowfields is the following:

$$\varepsilon_S = \frac{du}{dy} + \frac{dv}{dx} \tag{5.3}$$

ε_S	shear strain rate
v	axial velocity (in the direction of the flow)
u	radial velocity
x	radial direction
y	axial direction

The shear strain is intimately tied to the turbulent mixing process. Regions of high shear strain magnitude (maximum shear strain rates) coincide with regions of zero maximum axial velocity. It is in the large shear strain regions where the majority of mixing of inner and outer annulus flows and entrainment of reverse flow occurs. The counter-swirl condition shows greater regions of maximal shear strain. The difference between the rates of or magnitude of shear strain is negligible for the co-swirl and counter-swirl conditions. The counter-swirl condition has peak shear strain magnitudes over a wider and shorter region. This suggests and supports stronger and faster mixing for the non-reacting flows. It should also be noted that the shear strain regions frame the internal recirculation zone as expected.

Figures 5.9 and 5.10 reveal the distribution of axial turbulence, V_{RMS} (Reynolds axial normal stress component) for the isothermal flowfields. There are two types of flows contributing to the turbulence created in the swirling flowfields. There is drag and separation along with spreading and mixing. The competing turbulence mechanisms result in very complex flowfields. Turbulence peaks in the shear region at the outer boundary of the internal recirculation zone and also inside the internal recirculation zone. Intense production of turbulence in these regions coincides with high values of velocity gradients dV/dy, dV/dx, dW/dx, and dU/dy. This trend is also seen in the Reynolds radial and tangential normal stress components shown in appendix C. Downstream of the internal recirculation zone the steep gradients of velocity are no longer present and the axial turbulence decays.

In the jet outflow region the high turbulence magnitude is convected radially as it moves downstream. Turbulence decays when the region of maximal shear flow terminates downstream.

The turbulent kinetic energy (TKE) is calculated from the PIV data by the following equation. These values are derived from mean quantities.

$$TKE = \frac{U_{rms}^2 + V_{rms}^2 + W_{rms}^2}{2} \tag{5.4}$$

TKE	turbulent kinetic energy
U_{rms}	radial root mean square velocity/Reynolds radial normal stress
V_{rms}	axial root mean square velocity/Reynolds axial normal stress
W_{rms}	tangential root mean square velocity/Reynolds tangential normal stress

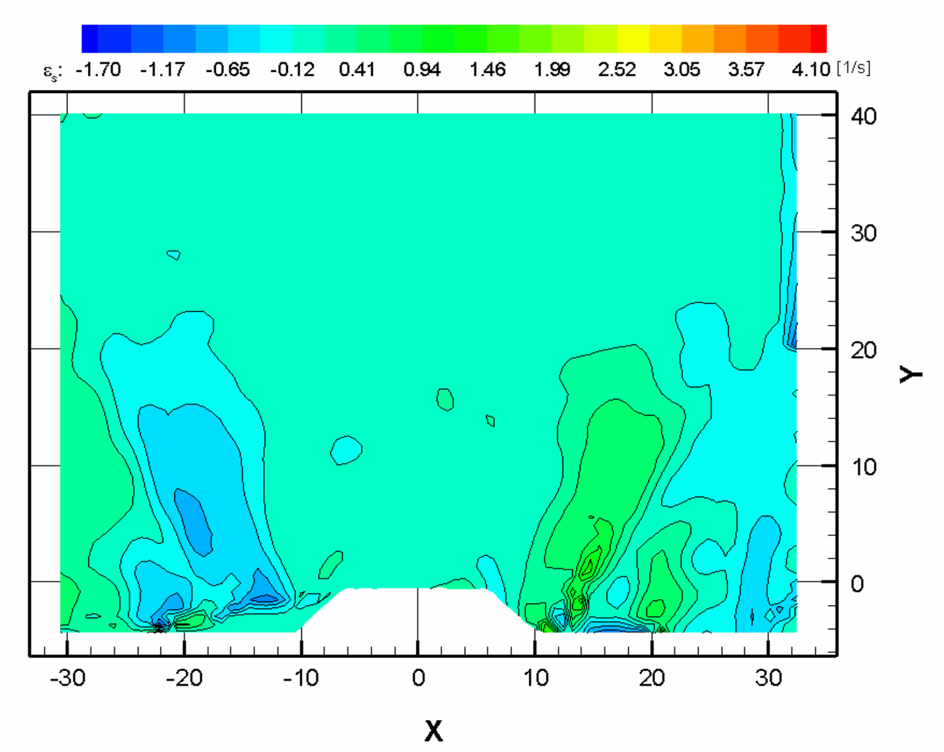

Figure 5.7 Shear Strain contour plot, 45°/50° co-swirl case, non-reacting condition, unconfined

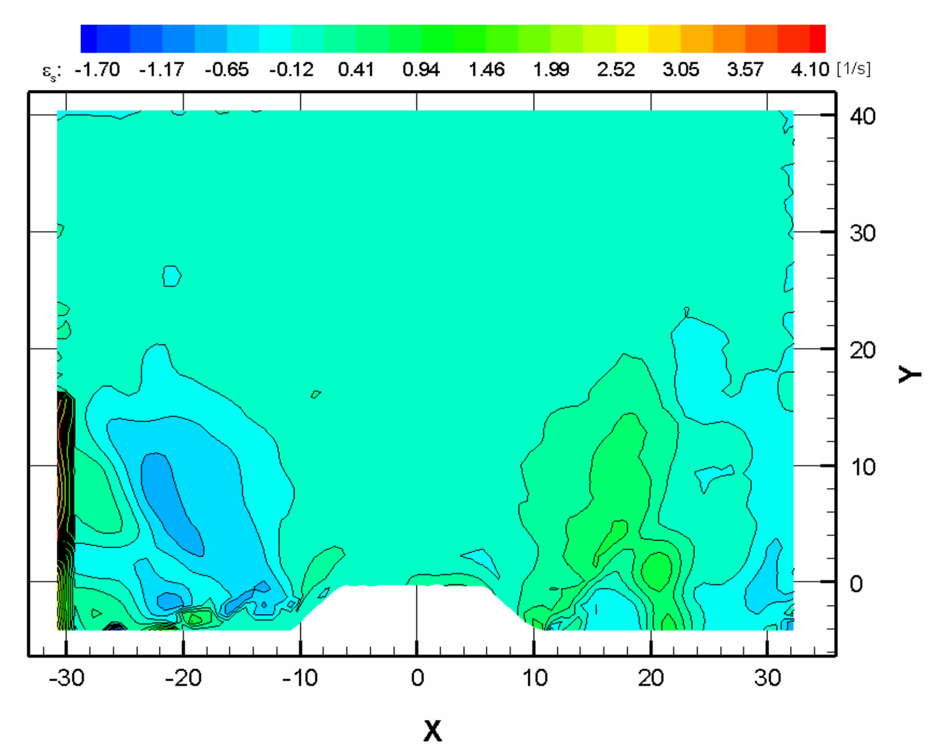

Figure 5.8 Shear Strain contour plot, 45°/-50° counter-swirl case, non-reacting condition, unconfined

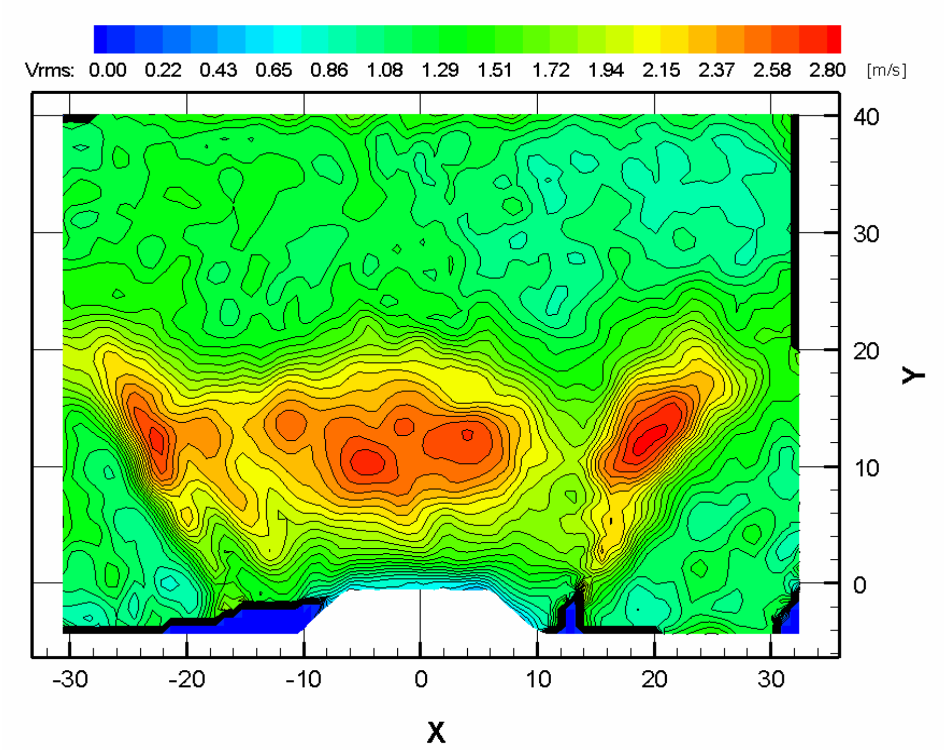

Figure 5.9 Axial RMS contour plot, 45°/50° co-swirl case, non-reacting condition, unconfined

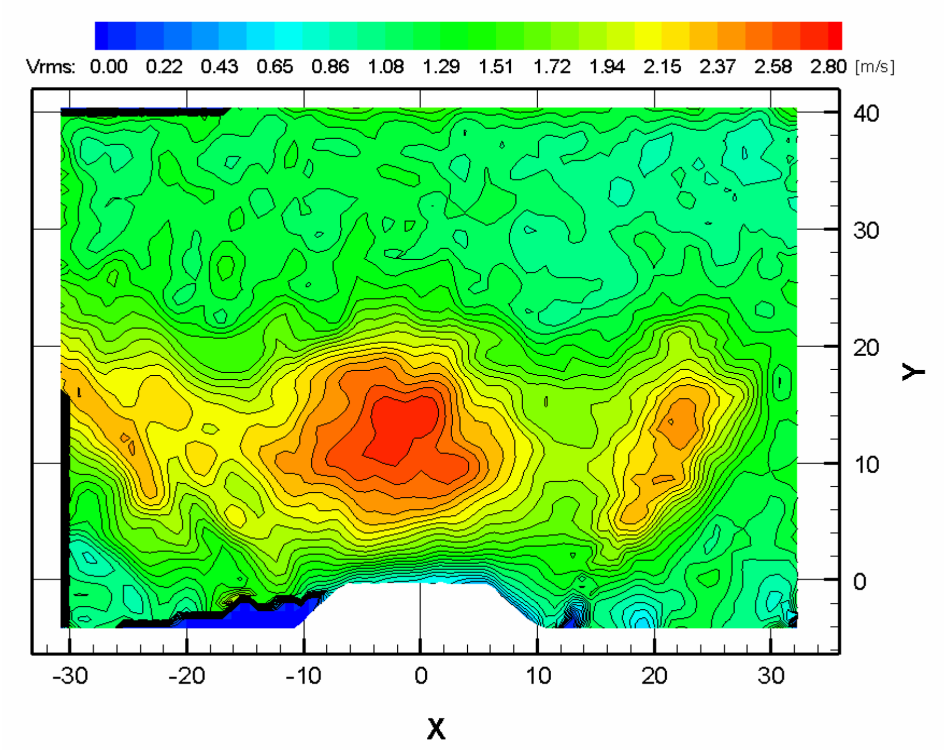

Figure 5.10 Axial RMS contour plot, 45°/-50° counter-swirl case, non-reacting condition, unconfined

The turbulent kinetic energy (TKE) distributions are presented in figures 5.11 (45°/50°) and 5.12 (45°/-50°). The co-swirl condition, figure 5.11, has discrete maxima of TKE in the shear layer region.. TKE also peaks to a higher value for the co-swirl condition than the counter-swirl condition. This is expected since the normal stress components magnitudes are higher for the co-swirl condition. Also the higher turbulence is a result of the larger vortical structures developed by the co-swirl condition. During convection, the vortices and vortex filaments are tilted and stretched by mean shear. Spin is enhanced due to the conservation law of angular momentum. Therefore the energy of the vortices increases at the expense of the mean flow energy. Specifically the co-swirl condition has larger turbulent structures (greater energy carrying eddies). The larger structures lead to slower convection of energy and momentum thus retarding the rates of reaction and the combustion process. The counter-swirl condition, figure 5.12, shows a peculiar peak in the internal recirculation zone. This could be due to greater reverse flow velocity and bears further study. Increased swirl strength promotes excess turbulence. The peak of TKE in the internal recirculation zone for the counter-swirl condition shows that the turbulence is increased by a counter-swirl flow distribution.

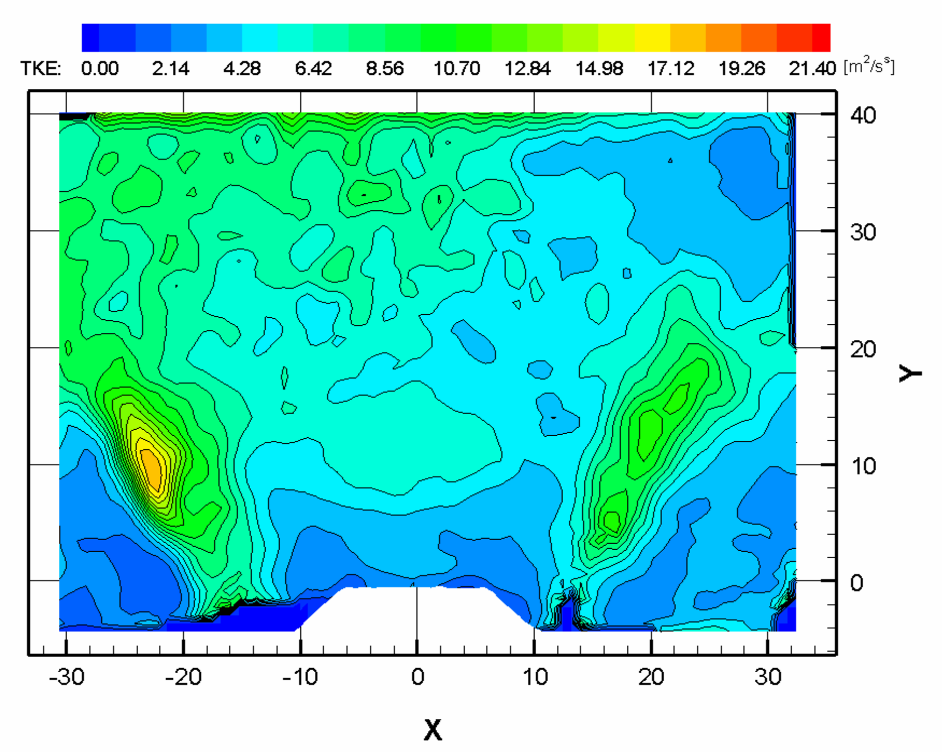

Figure 5.11 Turbulent Kinetic Energy contour plot, 45°/50° co-swirl case, non-reacting condition, unconfined

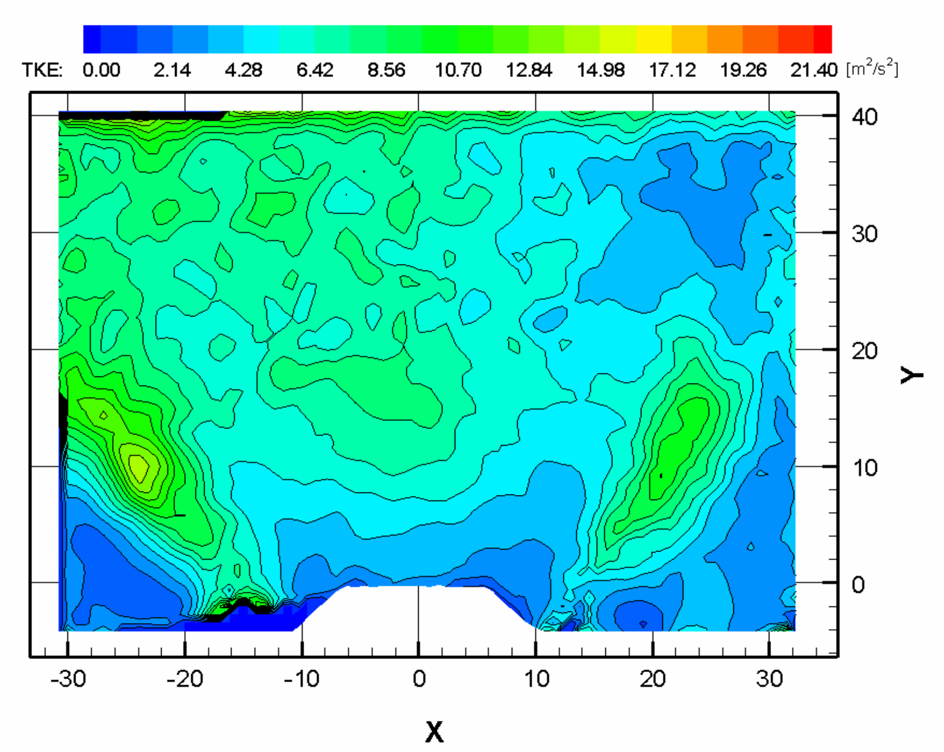

Figure 5.12 Turbulent Kinetic Energy contour plot, 45°/-50° counter-swirl case, non-reacting condition, unconfined

5.2.2 Unconfined Reacting Flowfield Data

The reacting/combusting unconfined contour plots show many of the same trends seen in the non-reacting unconfined flowfields. The axial velocity for the reacting flowfields is presented in figures 5.13 and 5.14. Combustion has enhanced the size of the internal recirculation zones and increased reverse flow magnitudes. Combustion affects the flowfield by expanding it radially; this increased radial growth is the result of thermal expansion caused by the heat release evolved in the combustion process. Also the increase in reverse flow velocity magnitude is due to heat release in the reacting flowfields. Exothermic reactions cause the hot gases created in the flame environment to travel faster than the corresponding fluid under non-combustion conditions. This is because the hotter gases have a lower density and thus the higher momentum gained at the reaction zone results in greater velocity of the flow. The greater reverse flow magnitudes and increase in width of the internal recirculation zones indicate that the swirl strength increases with combustion. Additionally, a stronger pressure gradient (increase in pressure difference) results from this increased velocity – a significant point since the pressure gradient balances tangential velocities and helps to determine recirculation zone size and strength.

With the increases in velocity magnitudes, one would expect the vorticity zones in the burning flowfields to increase in magnitude as well, which the results of this experiment supported; however they become thinner as a result of combustion since the vortex length scales are smaller in the burning flowfields than in the non-burning flowfields. The reason for this is twofold: heat release increases local acceleration and with the accelerated motions of combustion, the larger vortices collide and breakup. Subsequently, the expansion of the fluid that coincides with the heat release of the combustion process can reduce the vorticity by destroying the local vortices. Therefore, the size of the peak positive and negative vorticity concentration regions thins out with the addition of combustion. Generally, regions of concentrated vorticity are the only ones where all the molecular processes occur in the turbulent fluid – that is viscous dissipation of the turbulent energy, molecular mixing, molecular heat exchange and consequently, chemical reactions [51]. Although combustion does have a reducing effect on vorticity, the turbulence energy decay is not significant enough to laminarize the flow. This is true because the heat release in one portion of the system causes the flowfield to change so that the vorticity generation terms are larger. Subsequently, combustion in one region intensifies turbulence in other regions [51], which is reflected in the increase in the magnitude of vorticity. A comparison of vorticity for unconfined isothermal and reacting flows can be seen in figure 5.15. Main vorticity regions are highlighted by red boxes.

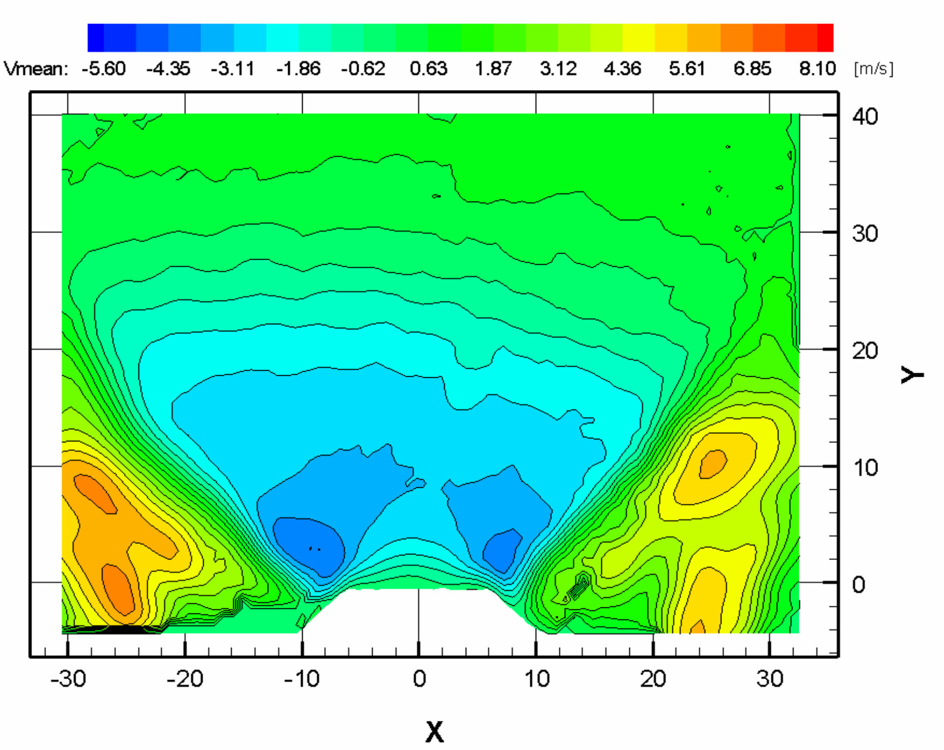

Figure 5.13 **Axial Velocity contour plot, 45°/50° co-swirl case, reacting condition, unconfined**

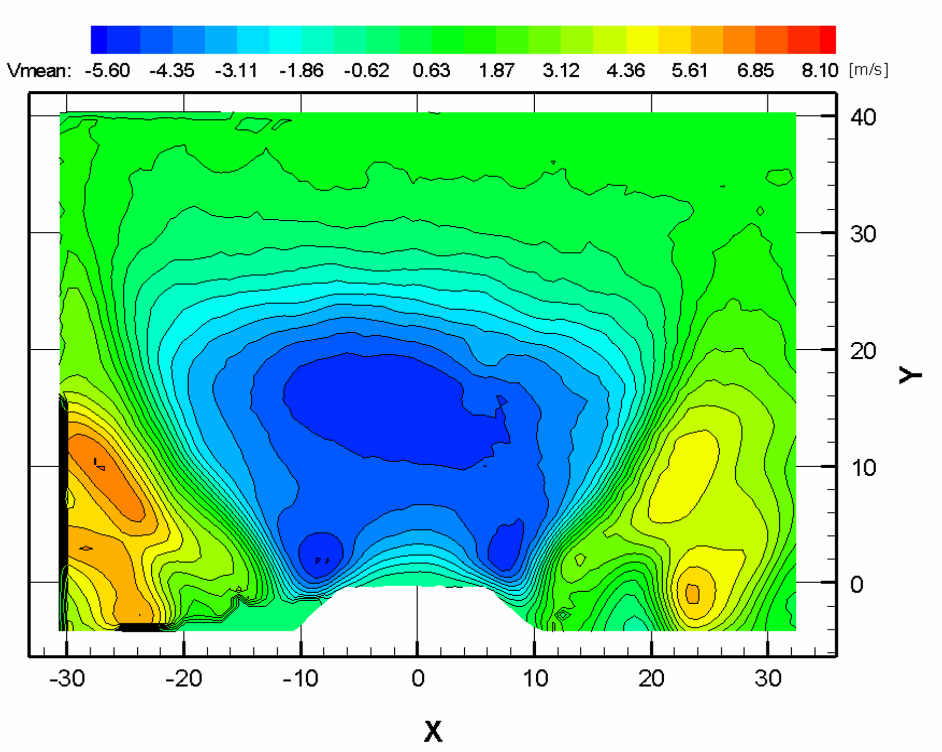

Figure 5.14 **Axial Velocity contour plot, 45°/-50° counter-swirl case, reacting condition, unconfined**

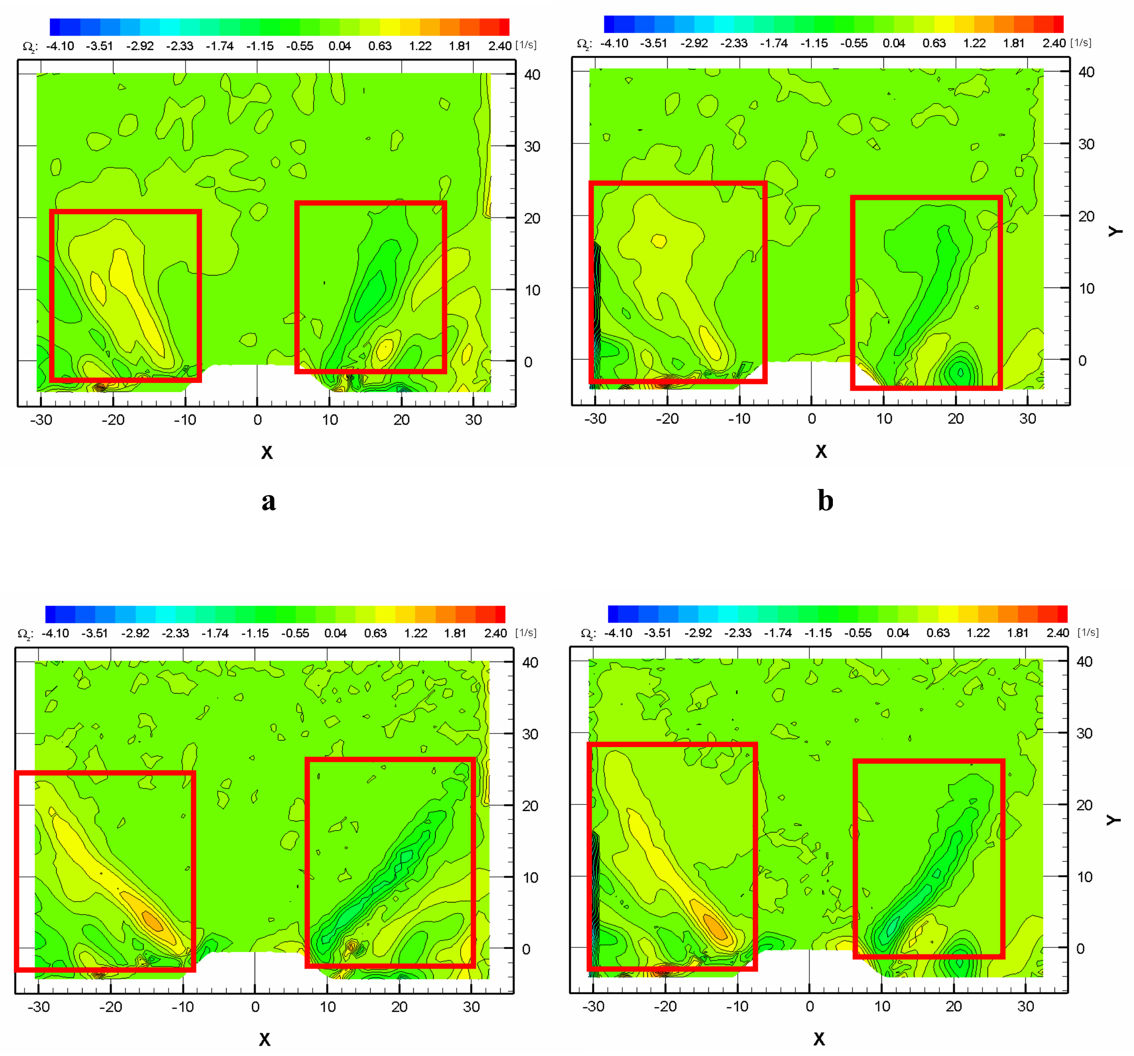

a

b

c

d

Figure 5.15 Comparison of Vorticity contour plots, 45°/50° co-swirl case and 45°/-50° counter-swirl case, non-reacting and reacting condition, unconfined

a) 45°/50° co-swirl case, non-reacting

b) 45°/-50° counter-swirl case, non-reacting

c) 45°/50° co-swirl case, reacting

d) 45°/-50° counter-swirl case, reacting

It is expected that mixing increases with combustion. The shear strain regions are a good indicator of mixing and areas of reaction in the flows. In the non-reacting flows the shear strain regions were wider for the counter-swirl condition. Figures 5.16 and 5.17 show the shear strain regions for the reacting unconfined flow conditions. Combustion increases the size of peak shear strain regions and also increases the distance between the peak shear strain regions as expected since the regions continue to frame the internal recirculation zone. Since the peak shear strain regions due increase in size it is surmised that combustion increases mixing. It is also seen that the counter-swirl case has the larger regions of shear strain and larger areas of peak shear strain. This suggests that the counter-swirl condition promotes rapid mixing and increased chemical reactions. This should influence the dispersion of flame radicals, temperature, and thermal uniformity.

Other important observations from the study are related to peak axial turbulence and turbulent kinetic energy. Peak axial turbulence regions in the reacting co-swirl case are smaller in size than those of the counter-swirl case. This is because the destruction of vorticity (or the reduction in vorticity) is greater for the co-swirl case due to less mixing and greater regions of positive axial strain, which increases the velocity magnitude and reduces the size of the peak turbulence regions. The reduction in vorticity is the result of a greater flame temperature in the co-swirl case. Greater peak flame temperatures can be a result of less air entrainment and recirculation of air and combustion products represented by the smaller reverse flow magnitude. Because of these features of the co-swirl case, one can see smaller size regions of axial turbulence. Axial turbulence contour plots are shown in figures 5.18 and 5.19.

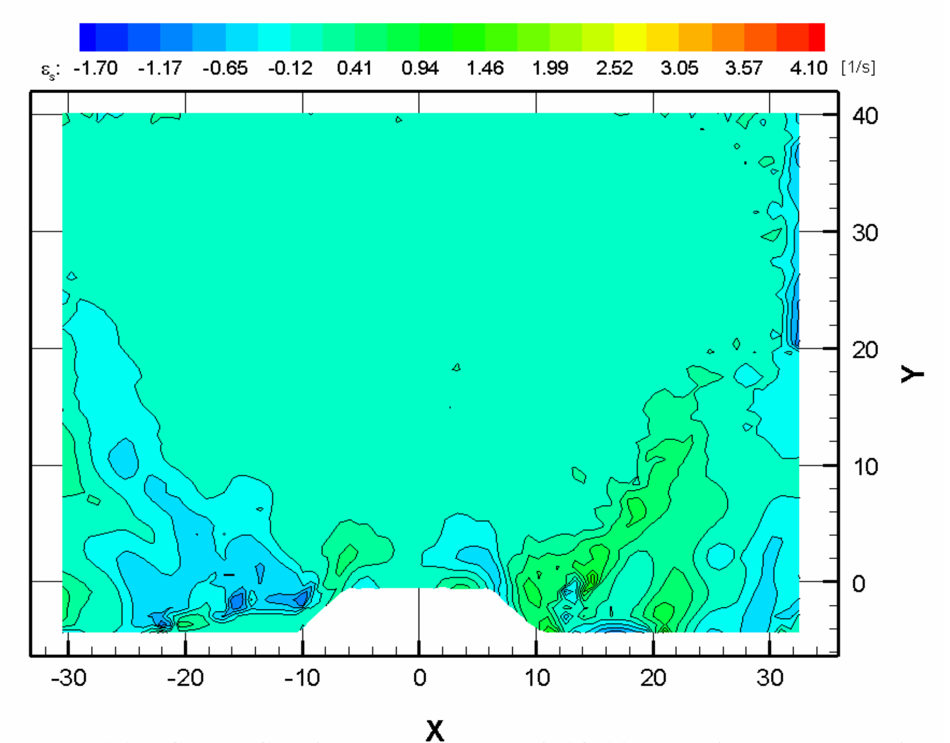

Figure 5.16 Shear Strain contour plot, 45°/50° co-swirl case, reacting condition, unconfined

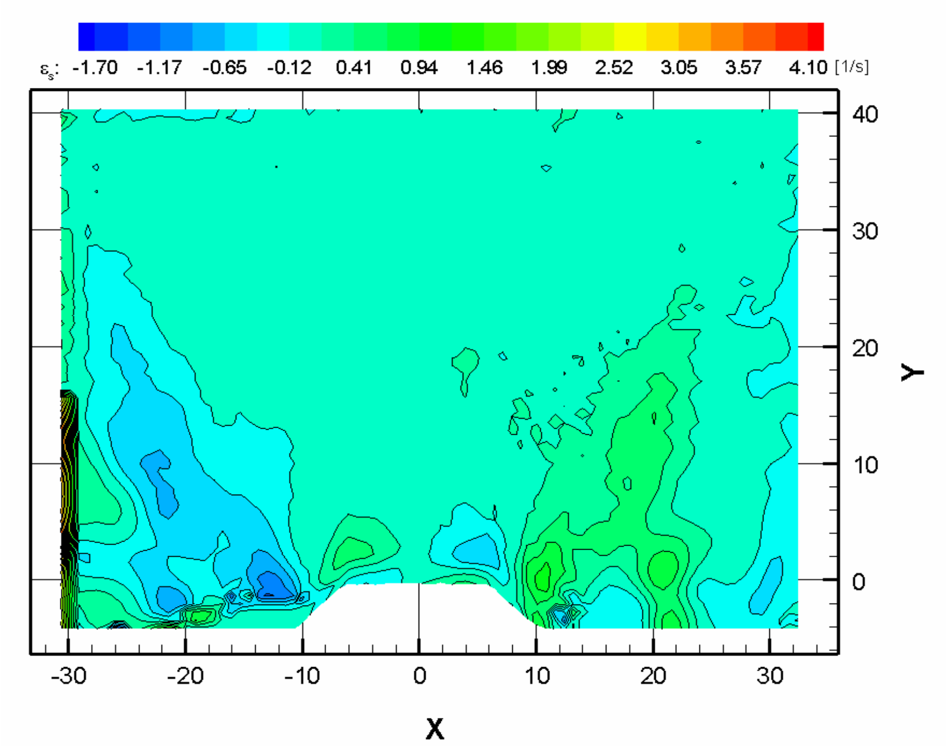

Figure 5.17 Shear Strain contour plot, 45°/-50° counter-swirl case, reacting condition, unconfined

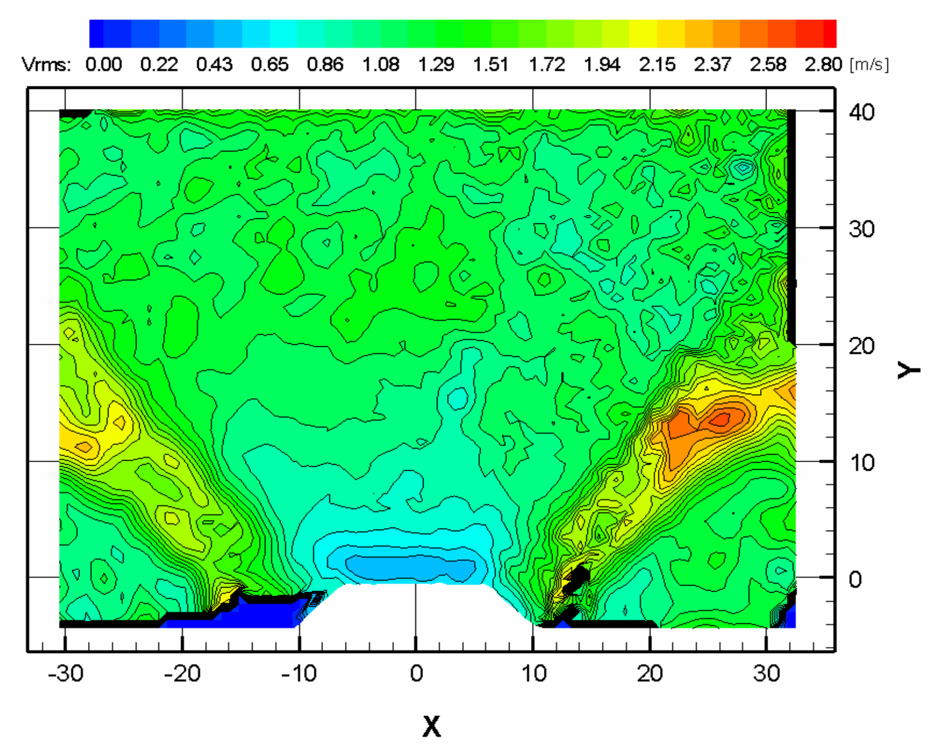

Figure 5.18 Axial RMS contour plot, 45°/50° co-swirl case, reacting condition, unconfined

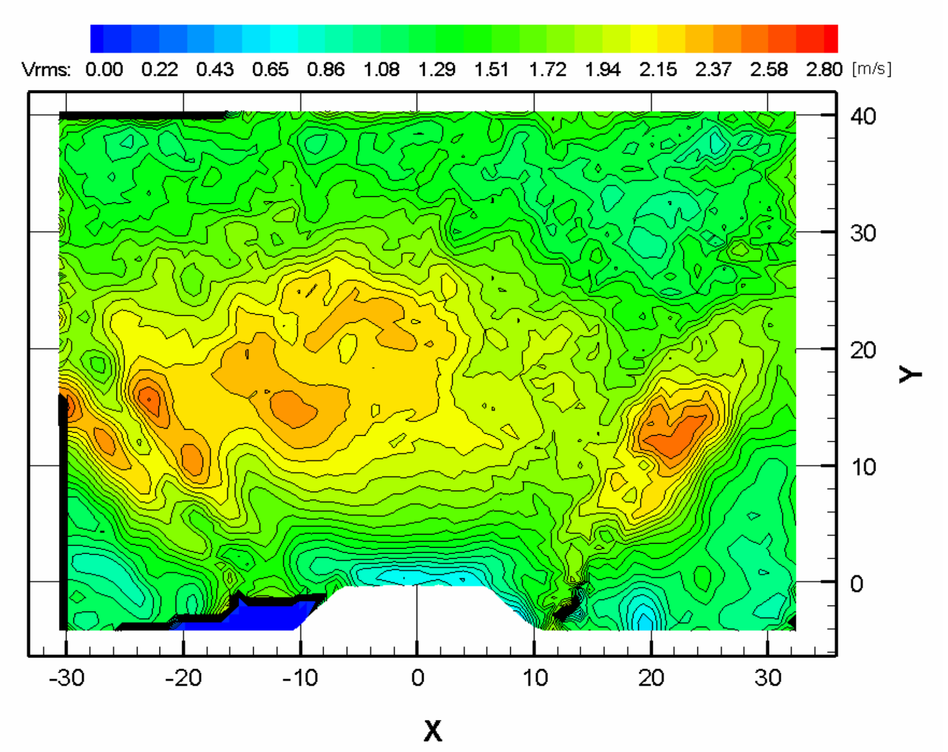

Figure 5.19 Axial RMS contour plot, 45°/-50° counter-swirl case, reacting condition, unconfined

Figures 5.20 and 5.21 show turbulent kinetic energy contour plots for the burning unconfined co-swirl and counter-swirl conditions, respectively. In terms of the turbulent kinetic energy peaks, greater peak magnitudes exist for the unconfined reacting flow than the unconfined isothermal flow for the co-swirl condition – a probable effect of increased velocity magnitudes due to combustion. Overall both flowfields exhibit smaller regions of high TKE values than their non-reacting counterparts. This is attributed to smaller regions of mean vorticity and, thus, a smaller amount of mean flow energy is lost to turbulence.

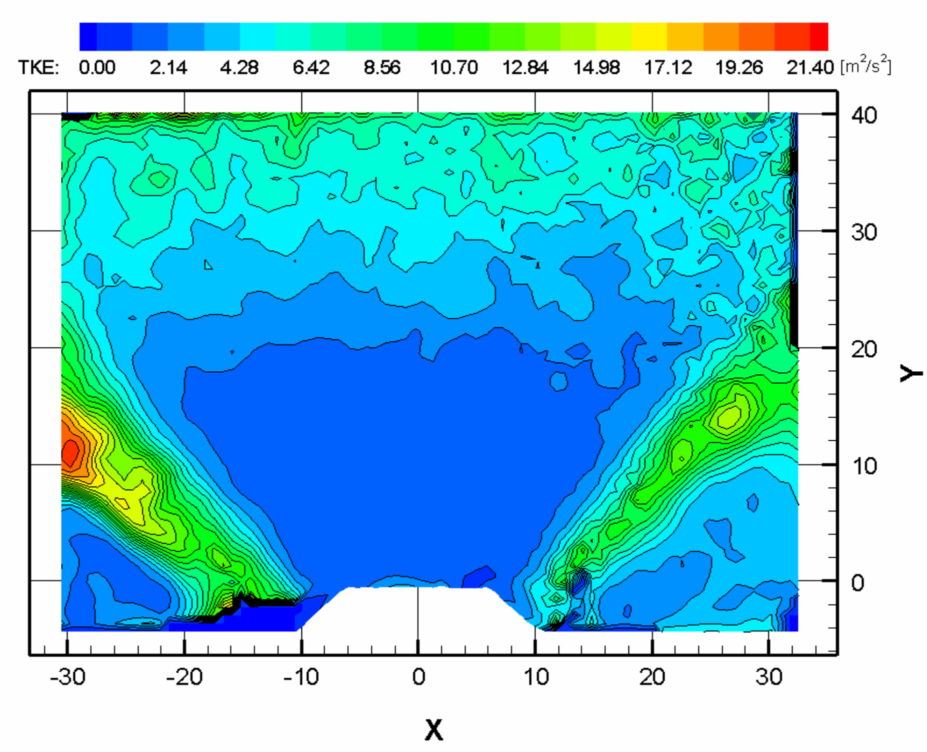

Figure 5.20 Turbulent Kinetic Energy contour plot, 45°/50° co-swirl case, reacting condition, unconfined

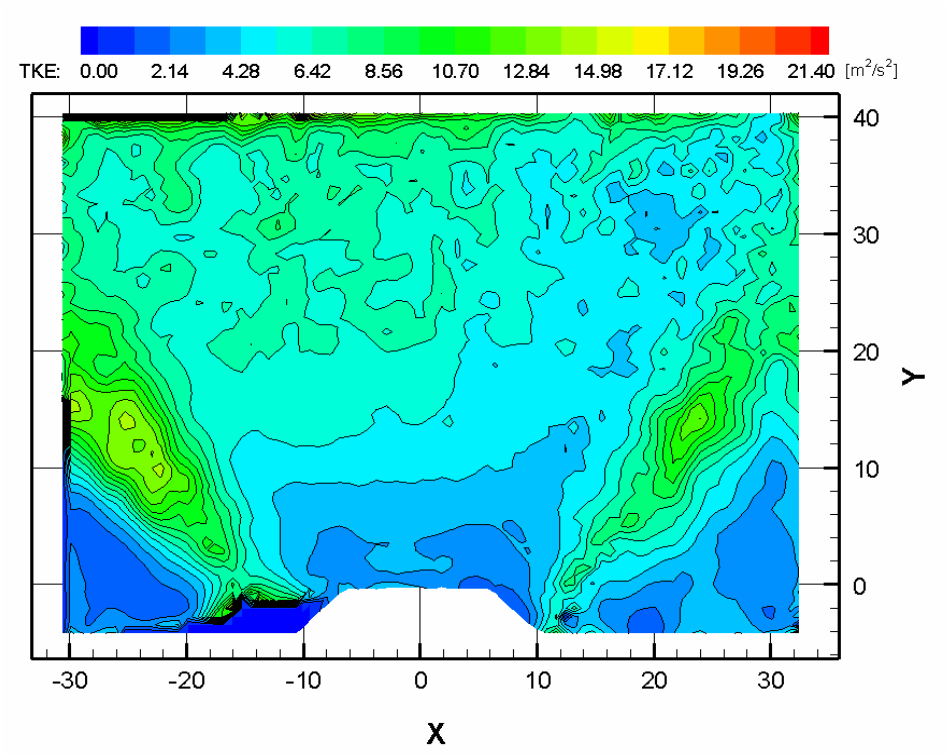

Figure 5.21 Turbulent Kinetic Energy contour plot, 45°/-50° counter-swirl case, reacting condition, unconfined

The differing momentum distributions and shearing forces created by the co-swirl and counter-swirl configurations cause differing velocity magnitudes, velocity decay, velocity trajectory, and positioning of maximum velocities for the jet outflow as you move further downstream. The co-swirl configuration has the higher velocity magnitudes further downstream in the outflow or shear layer region. The co-shearing forces in the co-swirl configuration seem to allow slower velocity decay and thus it can be rationalized that the mixing between the inner and outer annulus flows takes place over a longer time and not as efficient as the mixing for the counter-swirl condition.

5.2.3 Confined Non-Reacting Flowfield Data

Due to the increase in internal reflections distorting the observed flowfields for confined data the reported and discussed images are 2-D. Axial velocity vector plots, seen in figures 5.22 and 5.23, show many attributes of the two investigated non-reacting confined swirling flowfields. The data shows that confinement also affects the flowfields. The image in figure 5.22, a co-swirl condition (45°/50°), shows a wider and slightly longer internal recirculation zone. The incoming jet flow also is at a greater angle compared to the image in figure 5.23, a counter-swirl condition (45°/-50°). The above two observed physical aspects are attributed to the co-rotating natural expansion of both the inner and outer annulus air flows for the co-swirl flow. Note, the co-swirl condition does not provide a flow distribution that promotes opposing swirl directions for the inner and outer annulus flows. The confined environment impact the internal recirculation zones by reducing the width compared to the respective unconfined cases. The internal recirculation zones for the investigated confined flows have longer lengths than those observed for unconfined flows, figures 5.3 and 5.4, with the same swirl distributions. It is reasoned that the lack of surrounding air for confined flows enables internal recirculation zone lengths to develop unimpeded for a confined flow. The internal recirculation zone widths are reduced due to forced dampening of the tangential velocity. This is due to the imposed zero velocity boundaries at the walls. We also noticed that the annular jet flow velocity decays slower. Although the confined flowfields do not exhibit peak axial velocity magnitudes in the shear region, compared to the unconfined flowfields, they do exhibit higher velocities further downstream. This shows the effect of the area reduction forcing fluid out of the confinement and stretching the entire flowfield. The non-symmetry is thought to be a combination of imperfections in the swirler vanes from use and movement of the annuli pipes.

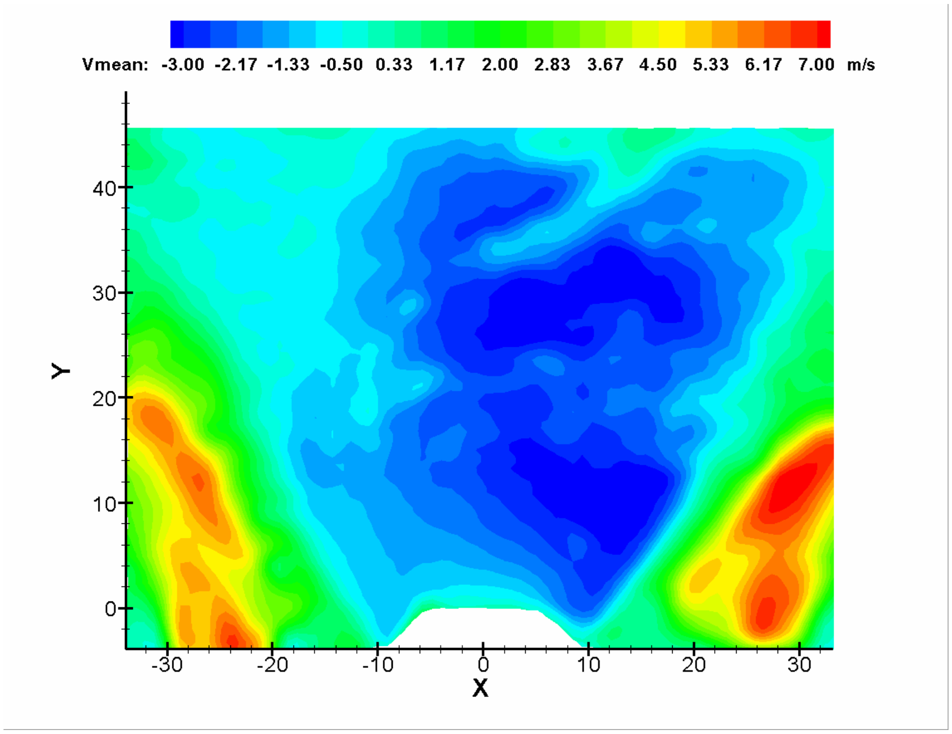

Figure 5.22 2-D Axial Velocity contour plot, 45°/50° co-swirl case, non-reacting condition, confined

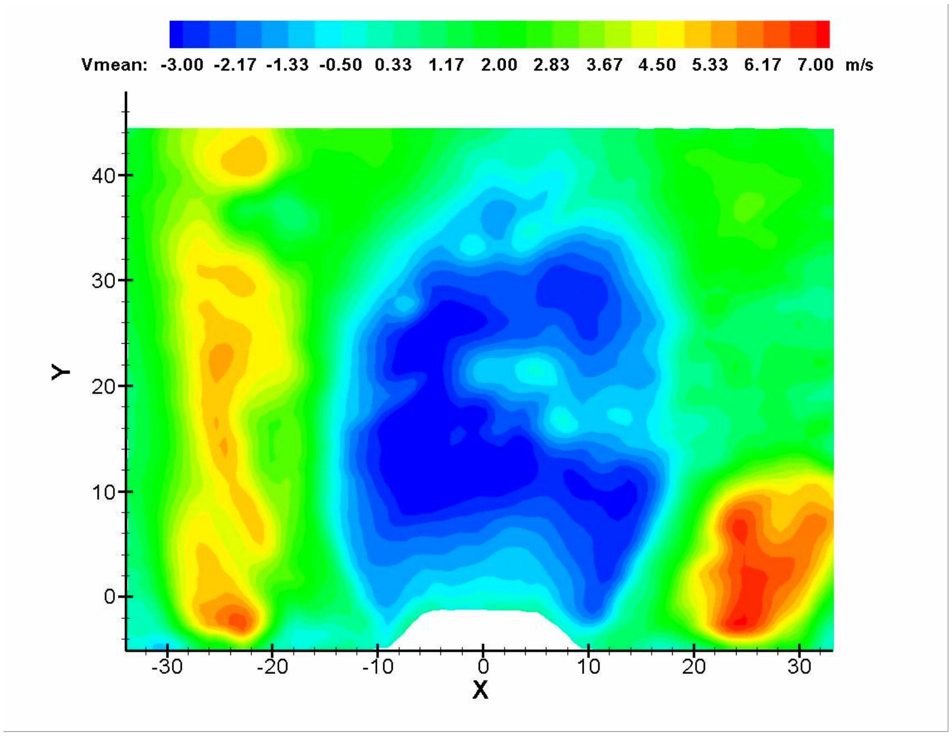

Figure 5.23 2-D Axial Velocity contour plot, 45°/-50° counter-swirl case, non-reacting condition, confined

For the current confined flows, the walls of the combustor isolate the flowfields from excess surrounding air. It is reasoned that recirculation zone length is now more readily controlled by the entrained mass flowrate derived from the input mass flowrate through the swirlers. The entrained mass flowrate is partly a function of the flowfields swirl strength, as shown by Kerr and Fraser [9].

$$\frac{\dot{m}_{e}}{\dot{m}_{sw}} = (0.35 + 1.4S_{N})\frac{x}{d_{eff}} \tag{5.5}$$

m_e	entrained mass flowrate
m_{sw}	swirler mass flowrate
S_N	swirl number
x	downstream distance
d_{eff}	effective diameter

The effective diameter term is determined with the following equation

$$d_{eff} = (D_{sw}^{2} - D_{hub}^{2})^{0.5} \tag{5.6}$$

D_{sw}	swirler diameter
D_{hub}	hub diameter

The observed flowfields as stated earlier have a difference in internal recirculation zone length. The counter-swirl internal recirculation zone length is less than that of the co-swirl internal recirculation zone length. This suggests that the swirl strength for the counter-swirl flowfield could be greater than that of the co-swirl flowfield. Shorter recirculation zone length could mean that you have a smaller area under the curve for axial velocity, thus decreasing the axial velocity flux and reducing the denominator in the swirl equation. With tangential momentum fluxes, numerator of the swirl equation, being equal a smaller denominator would allow for higher swirl strength. The data for the confined flowfield data investigation is 2-D which does not allow for calculation of the swirl number because the 2-D data does not provide the needed tangential velocity.

To explain how the counter-swirl condition could have stronger reverse flow velocities, let us revisit our discussion earlier about swirling axisymmetric flows. The tangential movement of fluid in axisymmetric flows induces centrifugal forces, which are balanced by a radial gradient of static pressure, seen in equation 5.2.

At the axis of symmetry a minimum pressure is generated and towards the jet boundary a positive pressure gradient is generated. Downstream of the swirler exit plane there is a decline of tangential velocity and the resulting centrifugal forces due to the divergence of the jet and conservation of angular momentum flux. This causes the static pressure to rise with increased distance from the swirler exit plane. A positive pressure gradient is generated along the axis. Once the pressure exceeds a characteristic value, a reversal of the flow velocity is achieved with negative axial velocities starting along the line of symmetry. The counter-swirl arrangement provides an additional decay of tangential velocity decay. This decay is superimposed on the effect of jet divergence as the inversely orientated fluxes of angular momentum from the inner and outer annulus partially compensate each other. These competing fluxes work to produce a stronger pressure gradient for the counter-swirl flowfield. This stronger pressure gradient is responsible for possibly increasing the reverse flow velocity of the counter-swirl flowfield.

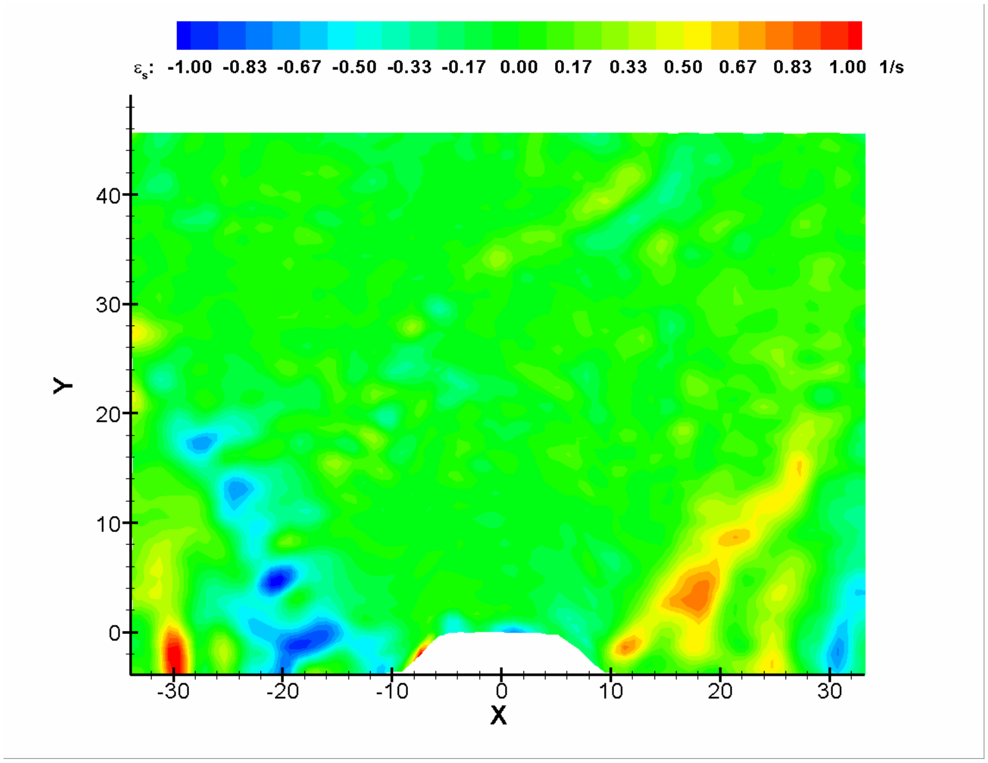

Figure 5.24 2-D Shear Strain contour plot, 45°/50° co-swirl case, non-reacting condition, confined

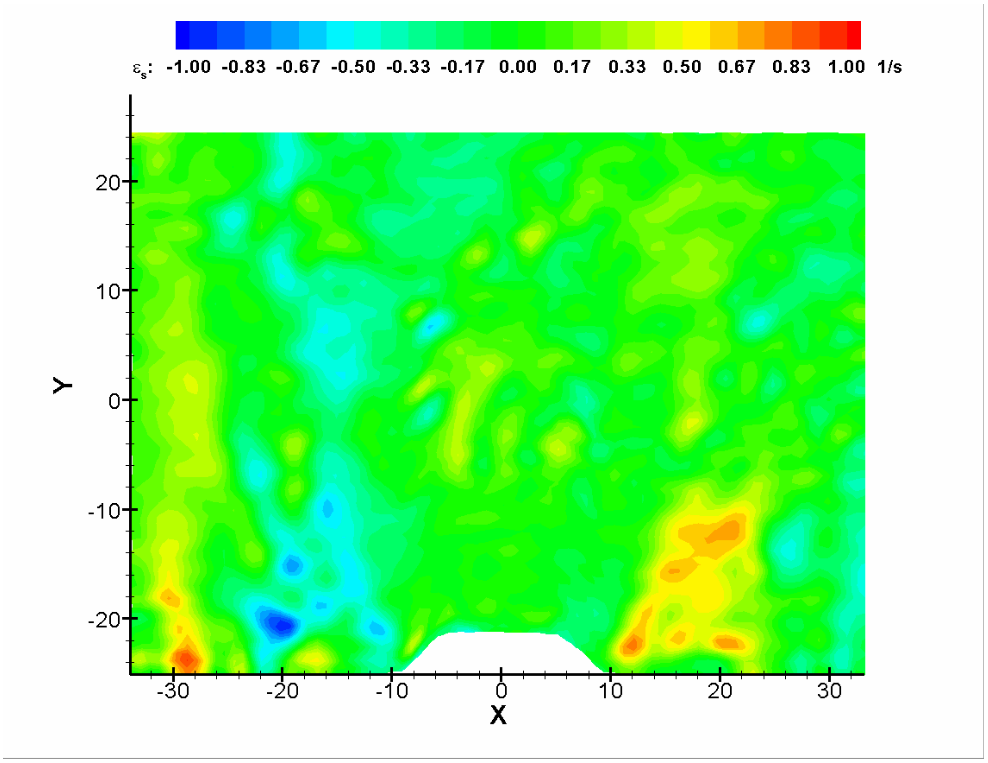

Figure 5.25 2-D Shear Strain contour plot, 45°/-50° counter-swirl case, non-reacting condition, confined

Figures 5.24 and 5.25 show the shear strain distribution for the confined non-reacting flowfields. The equation used to derive the shear strain from the investigated flowfields is the following:

$$\varepsilon_S = \frac{du}{dy} + \frac{dv}{dx} \qquad (5.7)$$

ε_S	shear strain rate
v	axial velocity (in the direction of the flow)
u	radial velocity (normal to the direction of the flow)

The shear strain is intimately tied to the turbulent mixing process. Regions of high shear strain magnitude (maximum shear strain rates) coincide with regions of zero maximum axial velocity. It is in these regions where the majority of mixing of inner and outer annulus flows and entrainment of reverse flow occurs. The counter-swirl condition shows greater regions of maximal shear strain. The difference between the rates of or magnitude of shear strain is negligible for the co-swirl and counter-swirl conditions. With essentially equivalent magnitudes of shear strain, the co-swirl condition having regions of smaller width of maximal or minimal shear strain over longer distances shows how the mixing process is longer and slower for the co-swirl condition. This is also evident in the length of the internal recirculation zone for the co-swirl condition.

The axial velocity contour plots, figures 5.22 and 5.23 also show that in the confined flows, formation of corner recirculation zones are possible. The location of these corner recirculation zones is between the edge of the outer swirler diameter and the combustor wall, which was not the region of measurement focus for this investigation. Even without the measurement region specifically taking into account the region where the corner recirculation zones are present, it should be noted that figures 5.22 and 5.23**,** show the presence of corner recirculation zones.

Flow confinement increases the internal recirculation zone length and also reduces axial velocity magnitude. Confinement causes a shift in the velocity magnitudes of two of the components of velocity, axial and radial velocity. Axial velocity magnitude is lessened by confinement while radial velocity is increased. Figures 5.26 and 5.27 show the confined non-reacting radial velocity contour plots.

The boundary layer build up on the walls of the enclosure helps in the dampening of the axial velocity magnitude. Also the area in which the flow has to pass through to flow out of the enclosure affects the velocity magnitudes. With this area being smaller than the confined environment it forces the incoming flow to preferentially accelerate in the radial direction (increased radial velocity) to offset the loss of momentum and velocity in the axial direction. The component of jet out flow in the radial direction is at a greater angle for the confined flows then for the unconfined flows, which supports the globally seen increased radial spreading in the confined environment.

Figures 5.28 - 5.31 show the unconfined and confined non-reacting radial strain contour plots. The positive radial strain is greater for the confined flowfields. This is expected and supports the increase in radial spreading and velocity for the confined flowfields.

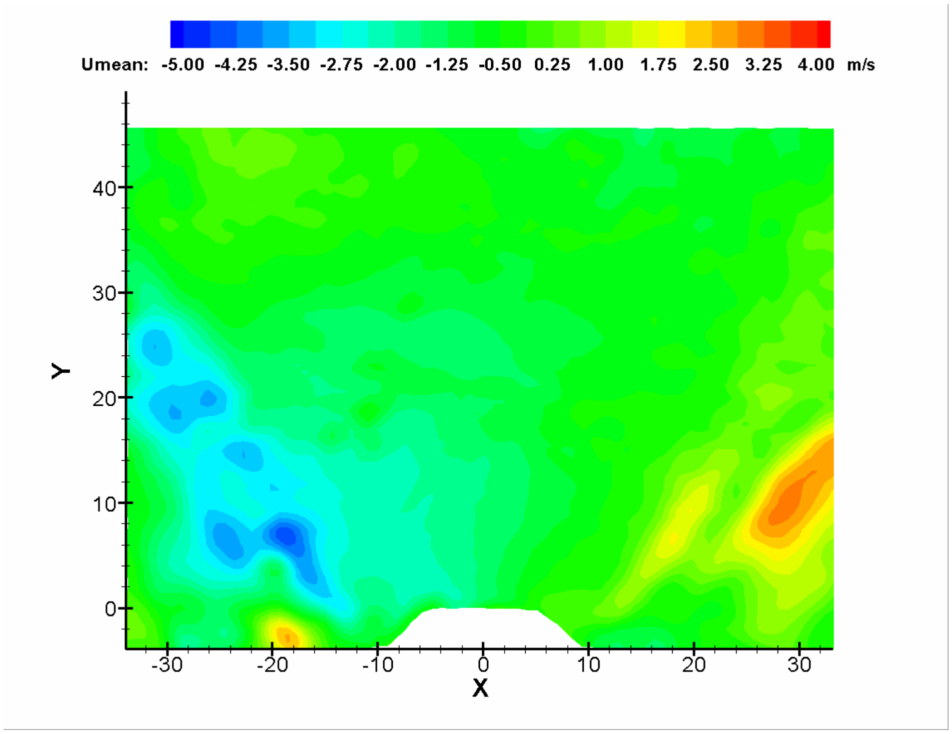

Figure 5.26 2-D Radial Velocity contour plot, 45°/50° co-swirl case, non-reacting condition, confined

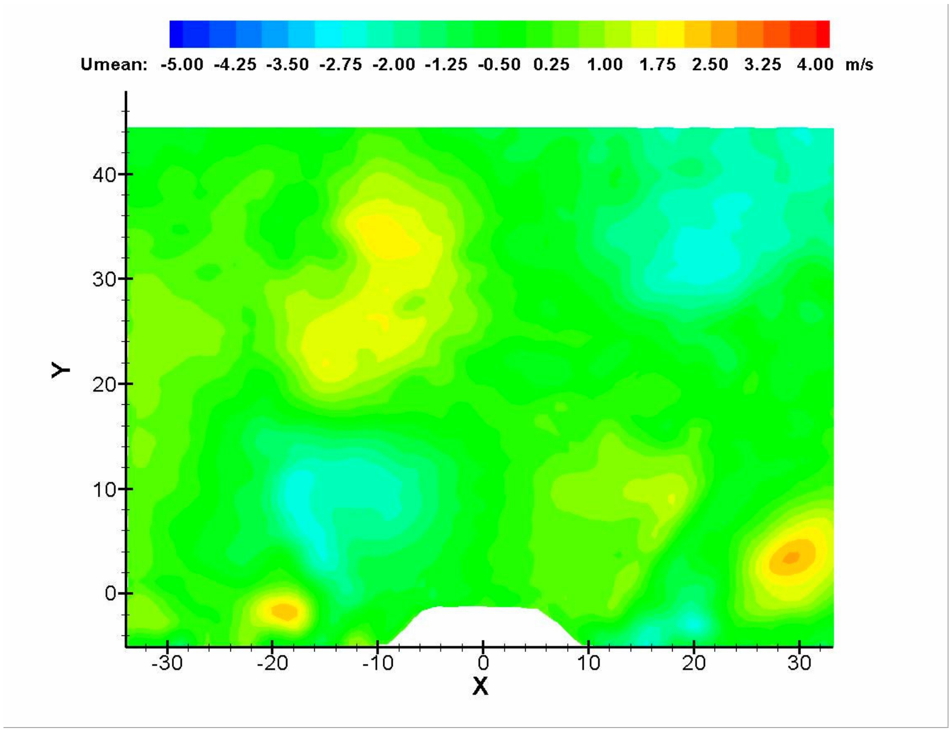

Figure 5.27 2-D Radial Velocity contour plot, 45°/-50° counter-swirl case, non-reacting condition, confined

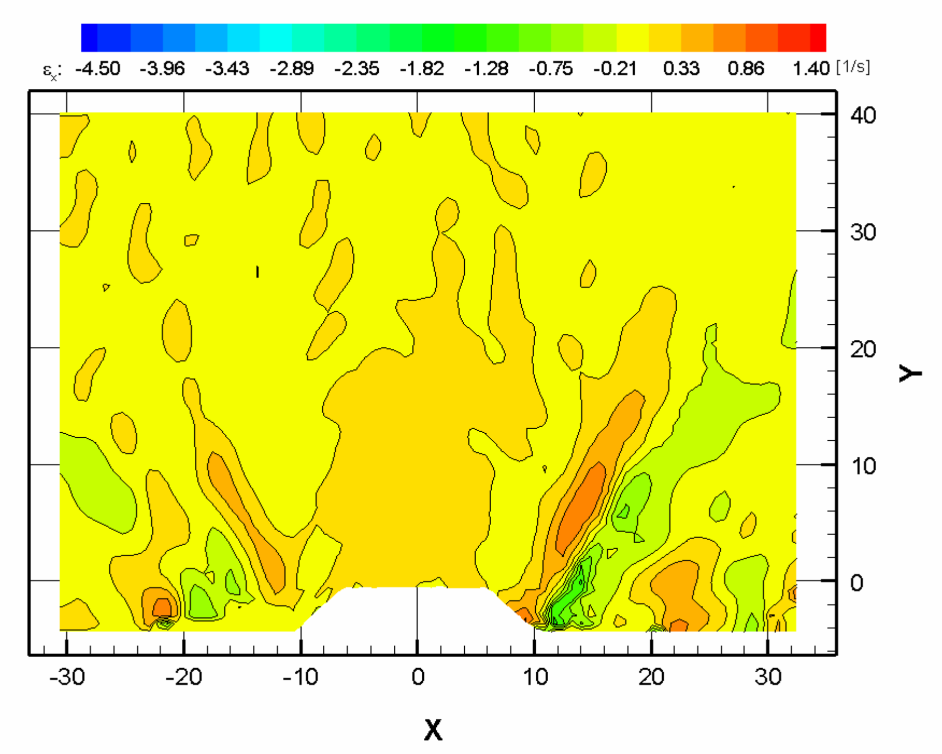

Figure 5.28 **Radial Strain contour plot, 45°/50° co-swirl case, non-reacting condition, unconfined**

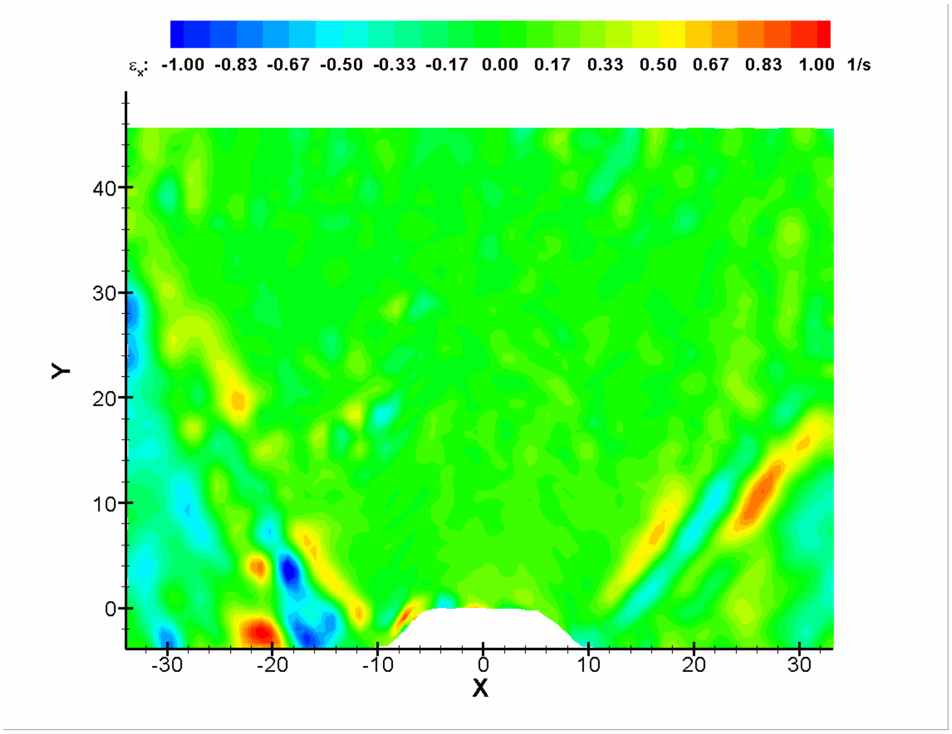

Figure 5.29 **2-D Radial Strain contour plot, 45°/50° co-swirl case, non-reacting condition, confined**

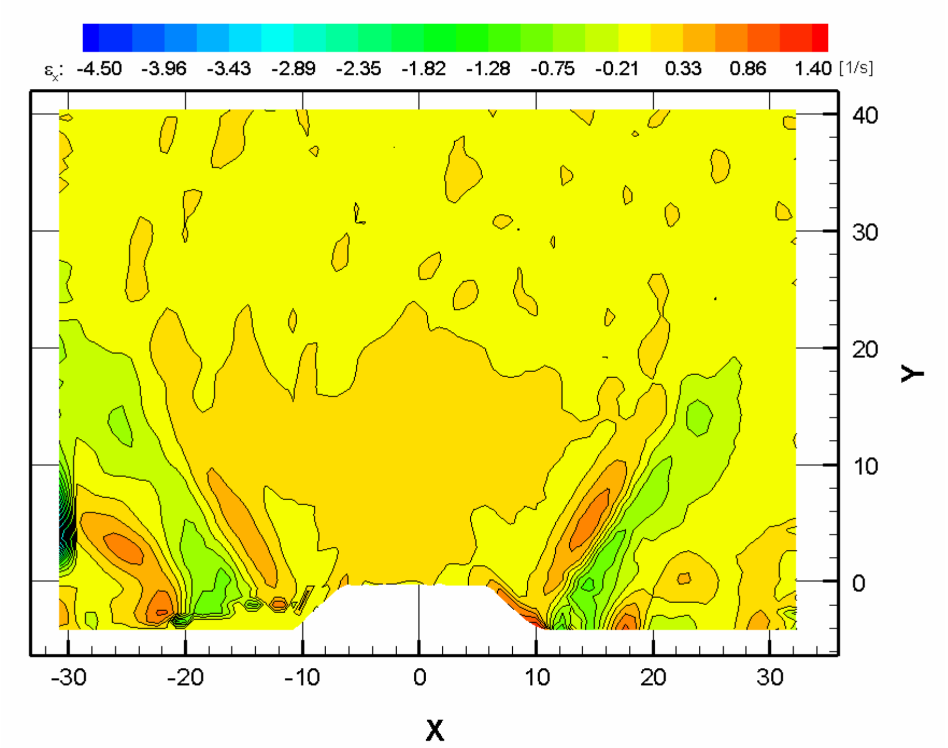

Figure 5.30 Radial Strain contour plot, 45°/-50° counter-swirl case, non-reacting condition, unconfined

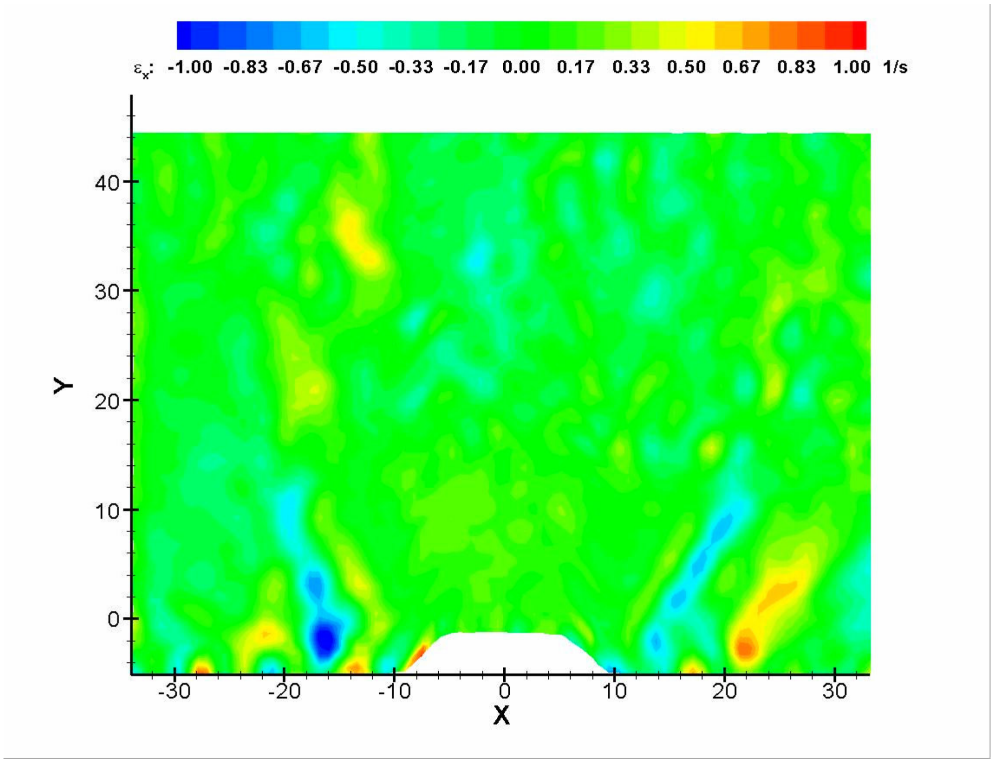

Figure 5.31 2-D Radial Strain contour plot, 45°/-50° counter-swirl case, non-reacting condition, confined

Figures 5.32 and 5.33 show the experimentally obtained axial rms or axial turbulence characteristics for the non-reacting confined flowfields. The turbulence characteristics of the confined flowfields do not differ greatly from that of the unconfined flowfields. The turbulence values peak in the shear layer regions and the internal recirculation zones. The maximum axial rms values are higher for the confined flows. This is mainly a result of higher velocity gradients in the confined flowfields. These higher velocity gradients are a function of the confinement impeding flow movement at the walls. Also velocity within the confinement is faster on a whole than the velocity seen in the unconfined flowfields. The turbulence magnitudes are increased due to the increase in regions of nearly zero local mean velocities in the confined flowfields.

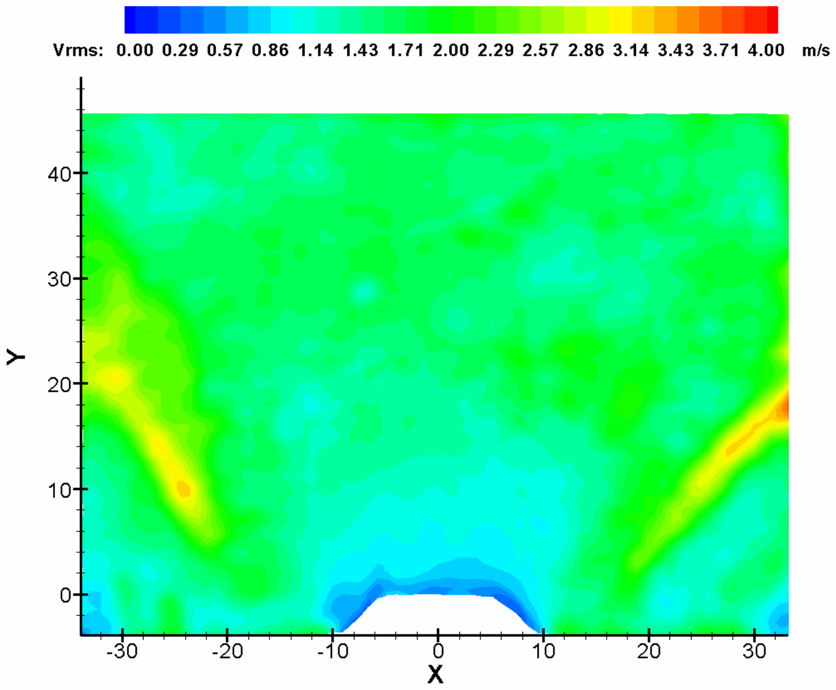

Figure 5.32 2-D Axial RMS contour plot, 45°/50° co-swirl case, non-reacting condition, confined

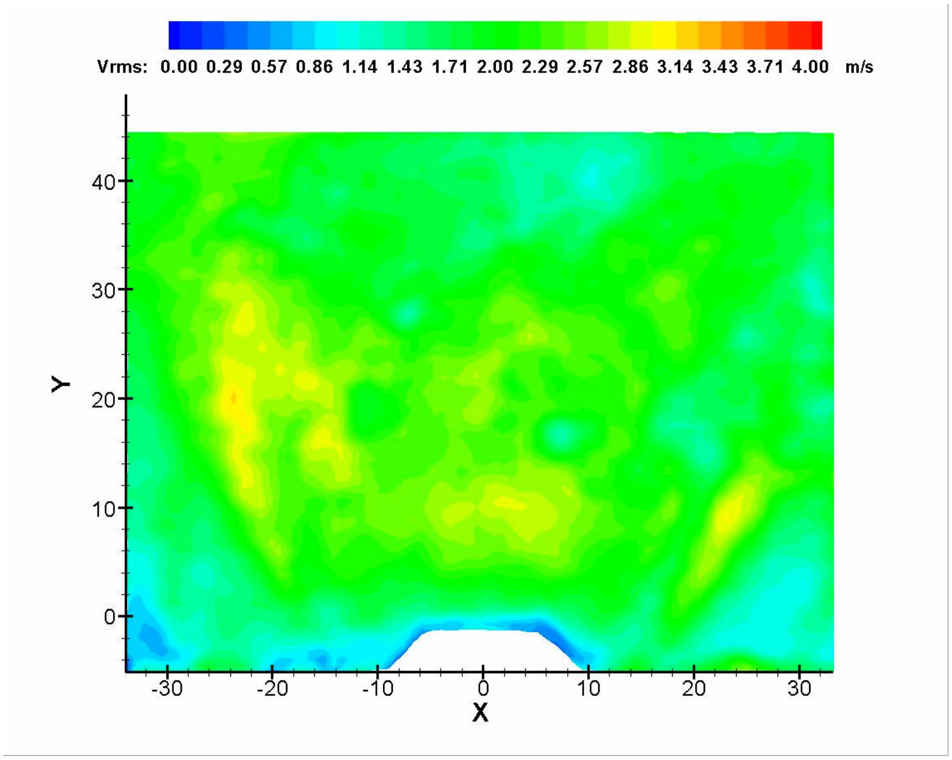

Figure 5.33 2-D Axial RMS contour plot, 45°/-50° counter-swirl case, non-reacting condition, confined

Turbulent kinetic energy contour plots for the confined non-reacting flows are seen in figures 5.34 and 5.35. The turbulent kinetic energy peaks in the shear region for the co-swirl confined non-reacting flowfield just as it does for the unconfined co-swirl flowfield. There are similarities between confined and unconfined flowfields for the co- and counter-swirl. They both have strong regions of TKE in the shear layer that extend to the internal recirculation zones that helps substantiate the influence of higher swirl strength for the counter-swirl condition. The sizes of the TKE peak regions in the shear layer are smaller for the confined flowfields. In the non-reacting flows of the confined environment there is an additional source for vorticity production, the enclosure walls. This allows for a more uniform turbulent energy distribution because of the increased number of vortex filaments tilted and stretched by the mean shear flow. It is reasoned that the confined environment allows for many smaller energy carrying eddies instead of the larger but less in number, eddies of the unconfined environment. The smaller energy carrying eddies allows the TKE for the confined environment to have a lower magnitude than that of the unconfined environment and signals that less flow energy is lost and allows for stronger chemical reactions.

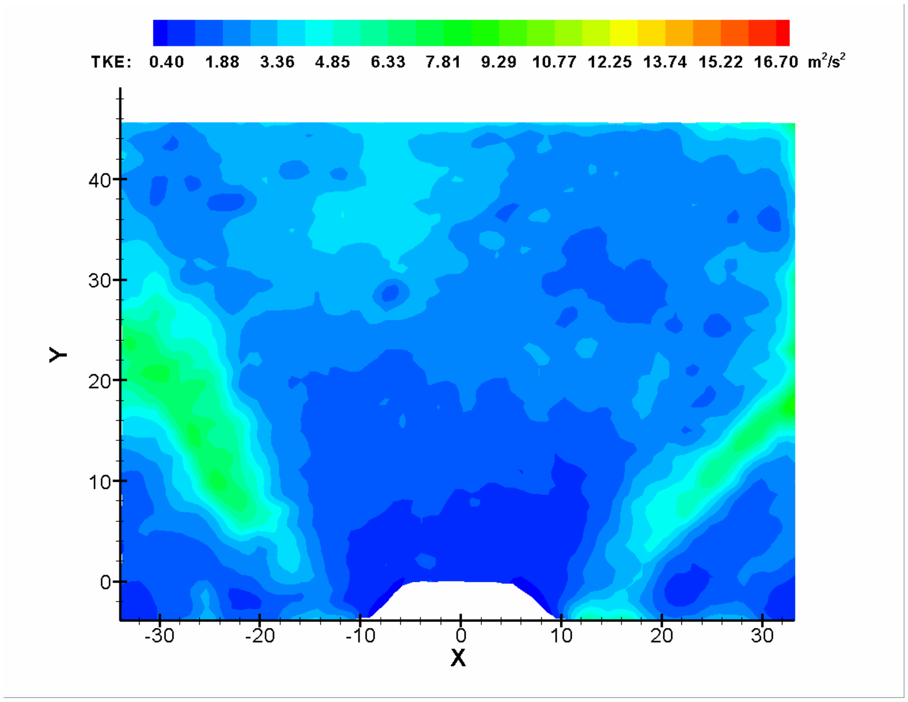

Figure 5.34 **2-D Turbulent Kinetic Energy contour plot, 45°/50° co-swirl case, non-burning condition, confined case**

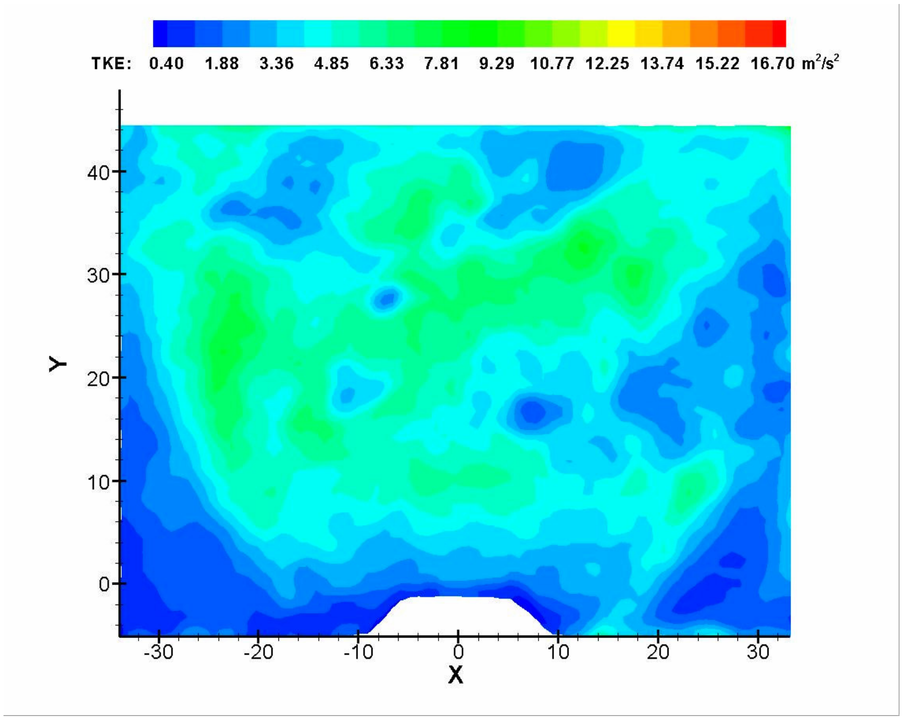

Figure 5.35 2-D Turbulent Kinetic Energy contour plot, 45°/-50° counter-swirl case, non-burning condition, confined case

5.2.4 Confined Reacting Flowfield Data

Figures 5.36 and 5.37, show confined reacting axial velocity contours for the investigated swirl distributions. Combustion influences the resulting flowfields in important ways. The internal recirculation zone is reduced in length with combustion. The decrease in internal recirculation zone length suggests that combustion influences swirl strength and mass flowrate entrainment for the swirl distributions investigated. Asymmetries seen are a result of swirler imperfections.

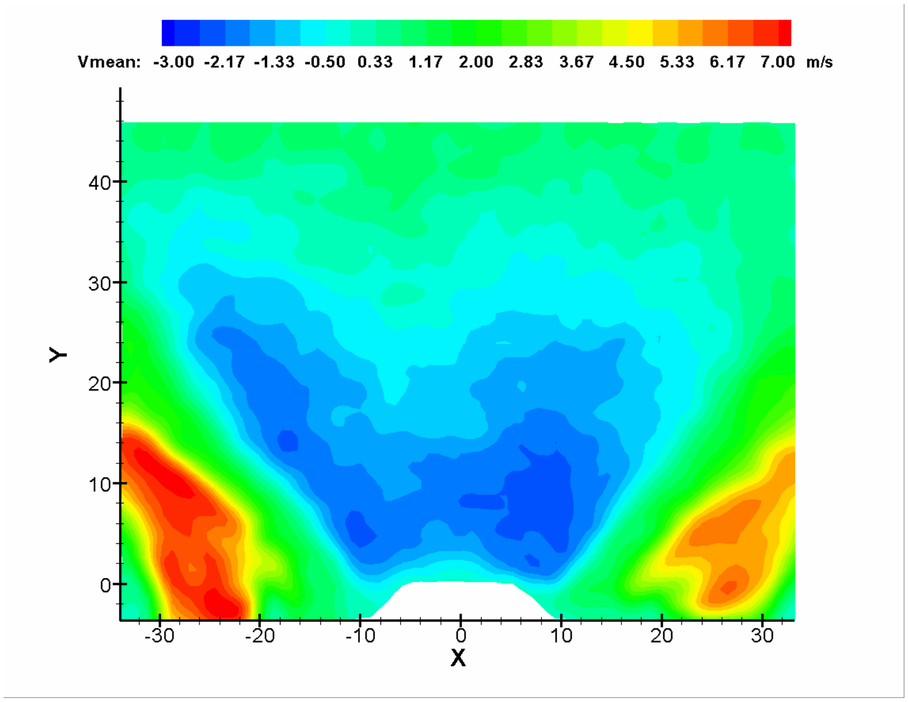

Figure 5.36 2-D Axial Velocity contour plot, 45°/50° co-swirl case, reacting condition, confined case

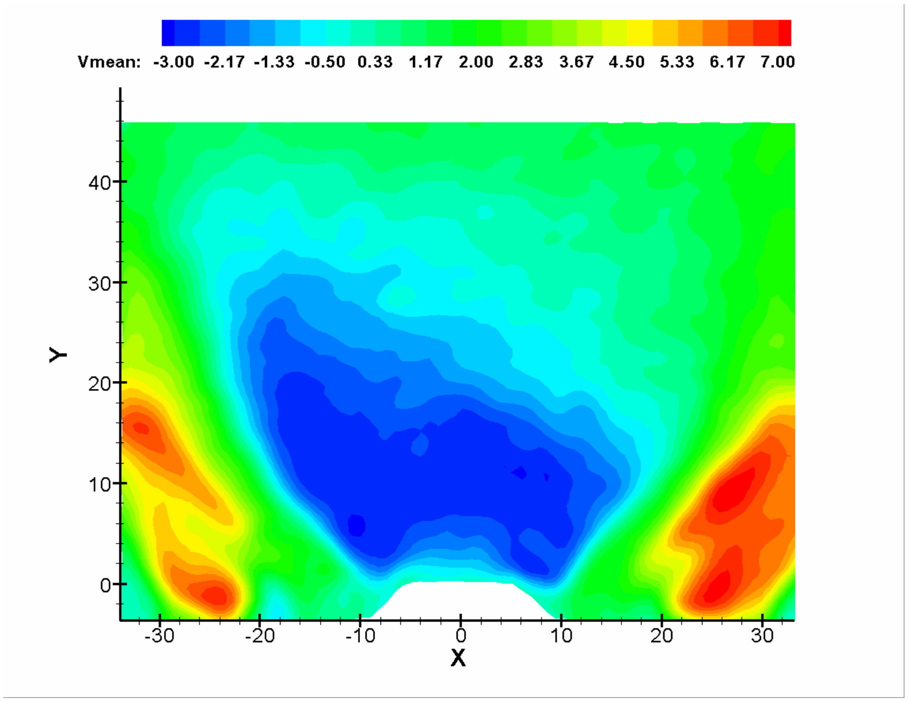

Figure 5.37 2-D Axial Velocity contour plot, 45°/-50° counter-swirl case, reacting condition, confined case

Consequently, combustion also expands the flowfield radially. This radial expansion of the flowfield is seen in the width of the internal recirculation zones, the angle of the jet outflow from the swirlers, and the radial strain. The angle of jet outflow, measured from the centerline, increases with the addition of combustion in both the co- and counter- swirl flowfields. The increased radial growth in the flowfields is the result of thermal expansion caused by the heat release involved in the combustion process. Figures 5.38 and 5.39 reveal an increase in positive radial strain for the reacting confined flows.

The velocity magnitudes increase with combustion. This increase in velocity magnitudes is more readily seen in the radial velocity magnitudes of the investigated swirl distributions. Greater radial expansion for the reacting confined cases is seen in figures 5.40 and 5.41. Also, in the reacting axial velocity flowfields there is clearly a greater uniformity of maximum velocity of the reverse flow and an increase in the reverse flow velocity magnitudes. This increased uniformity in maximum velocity is also seen in the jet outflow velocities. Increase in velocity magnitudes is the result of exothermic reactions that cause the hot gases created in the flame environment to travel faster than the corresponding fluid under non-combustion conditions. This is because the hotter gases have a lower density and thus the higher momentum gained at the reaction zone results in acceleration or greater velocity of the flow.

The counter-swirl flow distribution has a higher and more uniform reverse flow magnitude than the co-swirl flow distribution. This could signal greater swirl strength for the counter-swirl flow distribution. Reasons for counter-swirl flow distribution having higher swirl strength were discussed earlier.

Confinement also plays a role in the shape and size of the internal recirculation zones. The internal recirculation zone widths are reduced by confinement due to forced dampening of the tangential velocity. This is due to the imposed zero velocity boundaries at the walls. Figures 5.36 and 5.37, also show that in the confined reacting flows corner recirculation zones are present. In the examined measurement region of this investigation with the flow expansion caused by combustion these regions are very small and therefore not significantly discussed.

Figures 5.42 and 5.43 show the reacting shear strain contour plots for the two investigated swirl distributions. The regions (spatial distribution and width) of maximal and minimal shear strain decrease with the addition of combustion. This decrease in size of shear regions that signal turbulent mixing processes in the flowfield implies faster mixing of the fluid streams in the reacting flowfields. The heat release involved in the combustion process plays a role in reducing the size of the shear strain regions like it does in reducing vorticity regions in a combusting flowfield. Vorticity is reduced by the expansion of the fluid that coincides with the heat release of the combustion process. Reduction of vorticity is a result of the fluid expansion destroying the local vortex tubes. It reasons that since vorticity is the anti-symmetric part of the flowfield and the shear strain is the symmetric part of the flowfield that a reduction in one will also mean a reduction in the other. Even with the reduction of vorticity, combustion causes the vorticity generation terms in another part of the flowfield to increase; consequently this also implies that the shear strain generation terms increase. This can possibly explain how combustion can increase mixing with smaller shear strain regions.

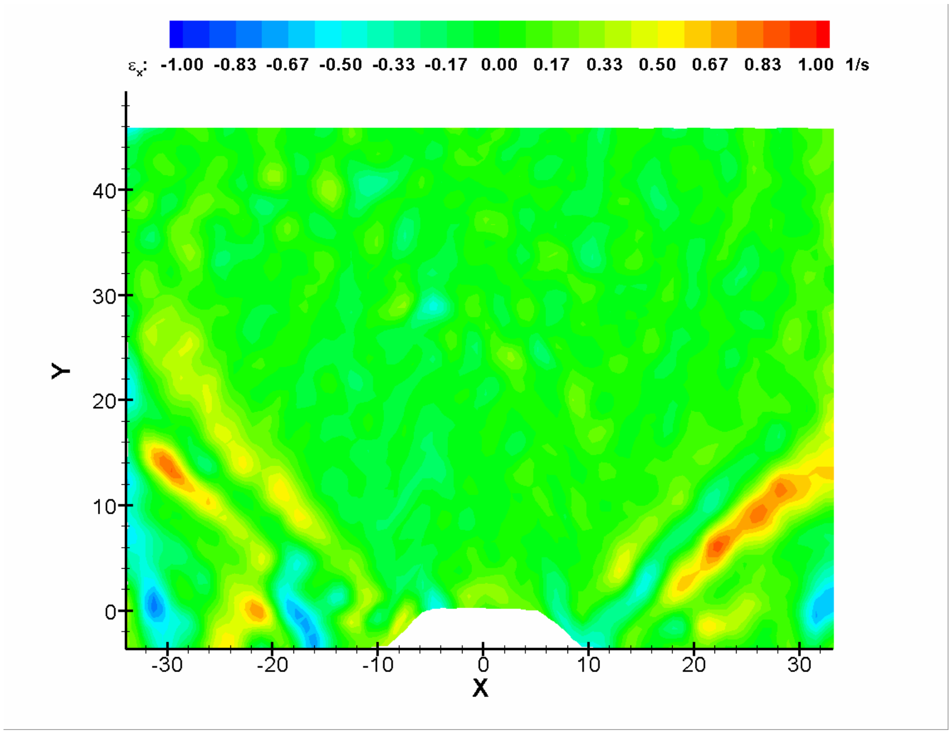

Figure 5.38 2-D Radial Strain contour plot, 45°/50° co-swirl case, reacting condition, confined case

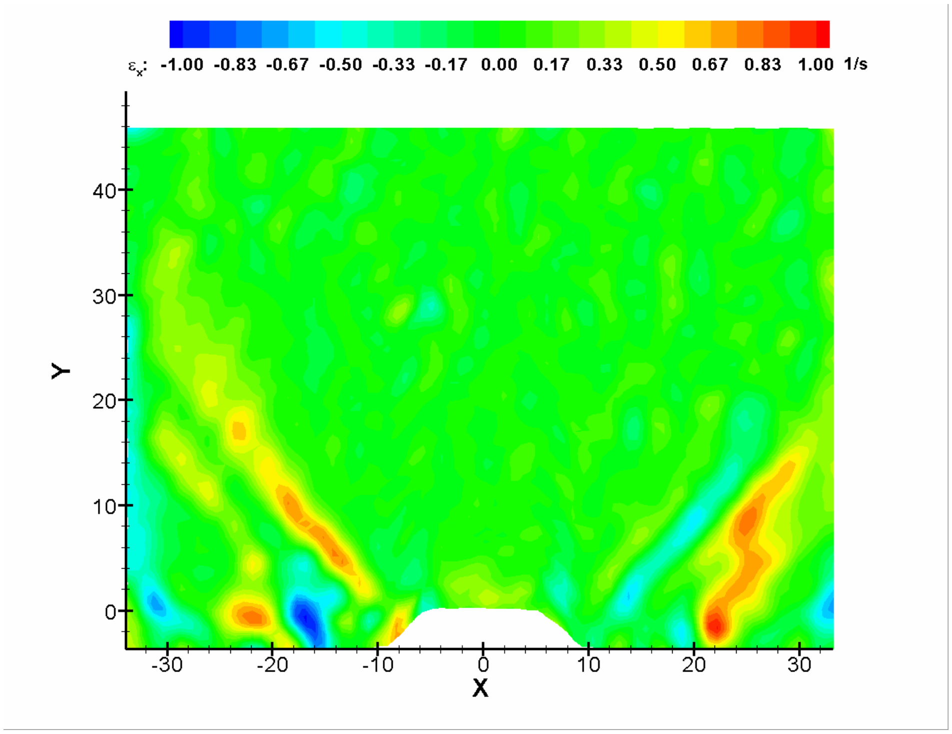

Figure 5.39 2-D Radial Strain contour plot, 45°/-50° counter-swirl case, reacting condition, confined case

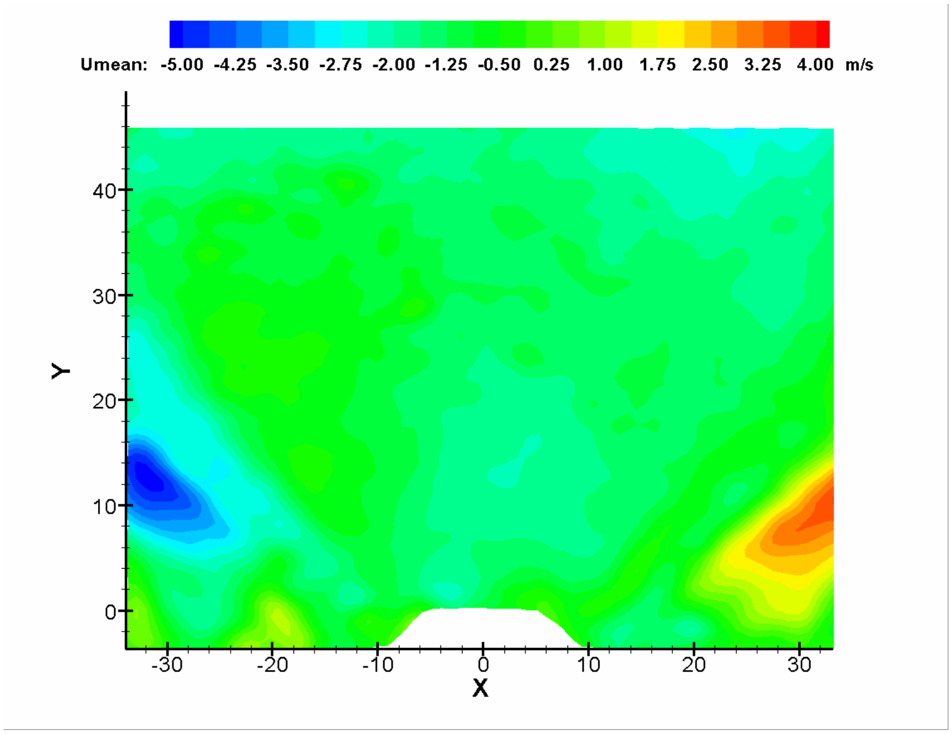

Figure 5.40 2-D Radial Velocity contour plot, 45°/50° co-swirl case, reacting condition, confined case

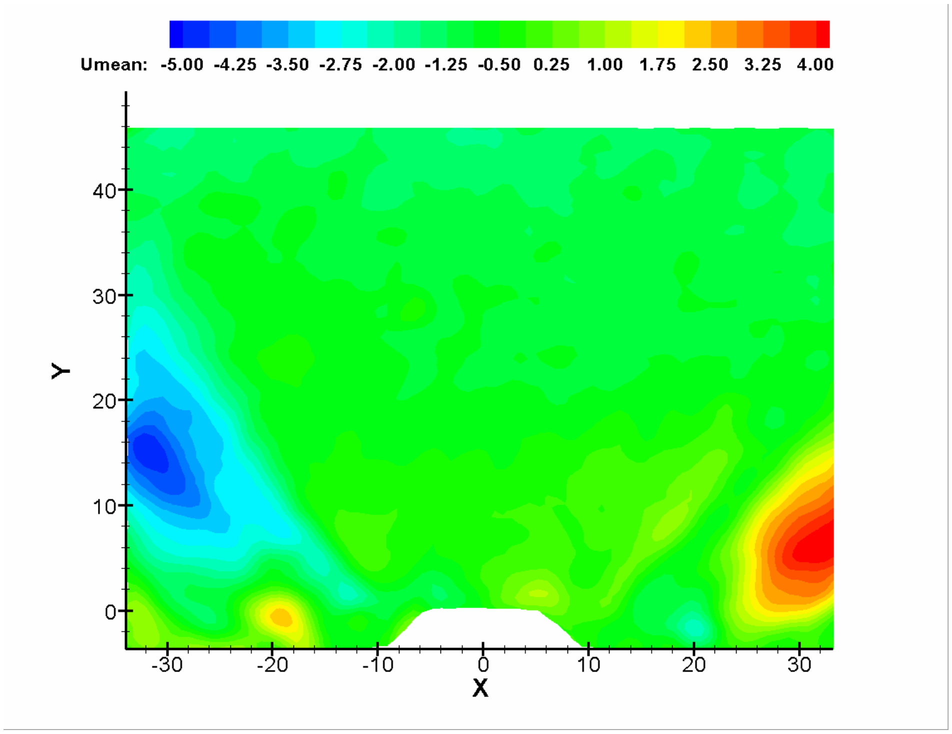

Figure 5.41 2-D Radial Velocity contour plot, 45°/-50° counter-swirl case, reacting condition, confined case

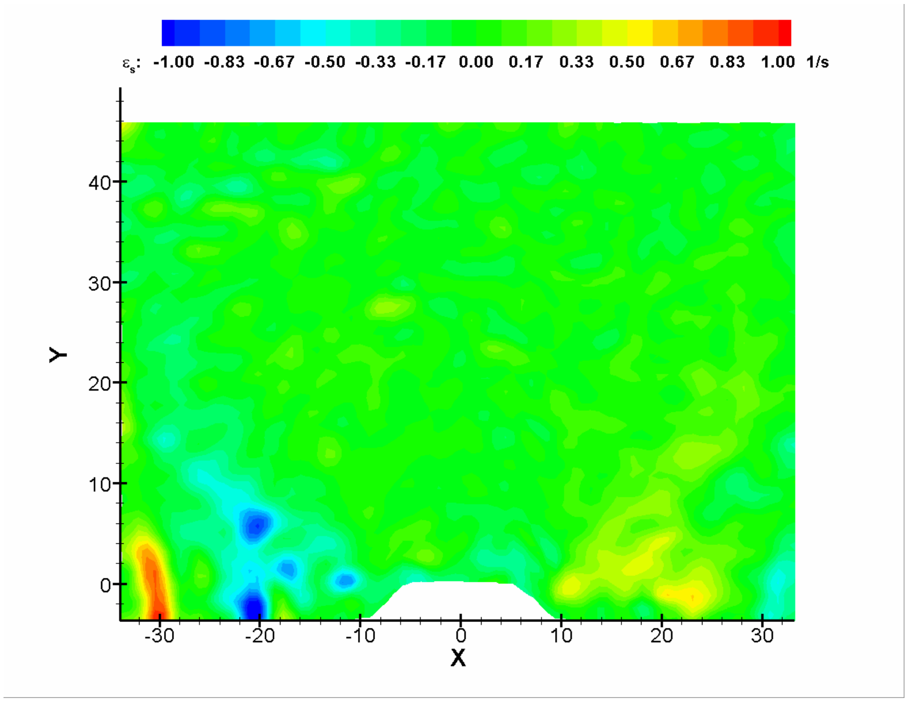

Figure 5.42 2-D Shear Strain Contour plot, $45^o/50^o$ co-swirl case, reacting condition, confined case

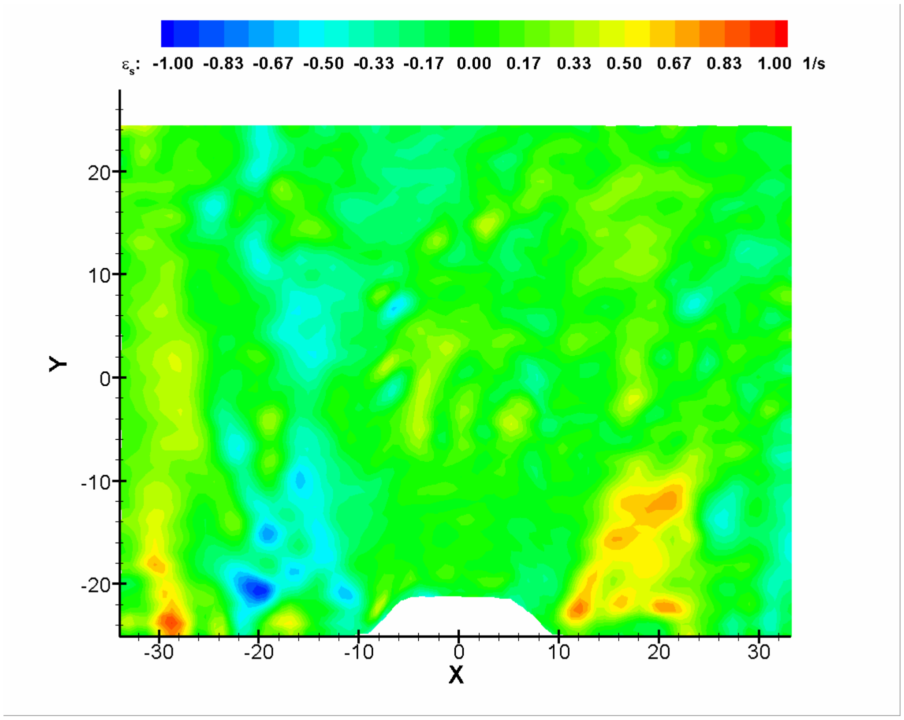

Figure 5.43 2-D Shear Strain Contour plot, $45^o/-50^o$ counter-swirl case, reacting condition, confined case

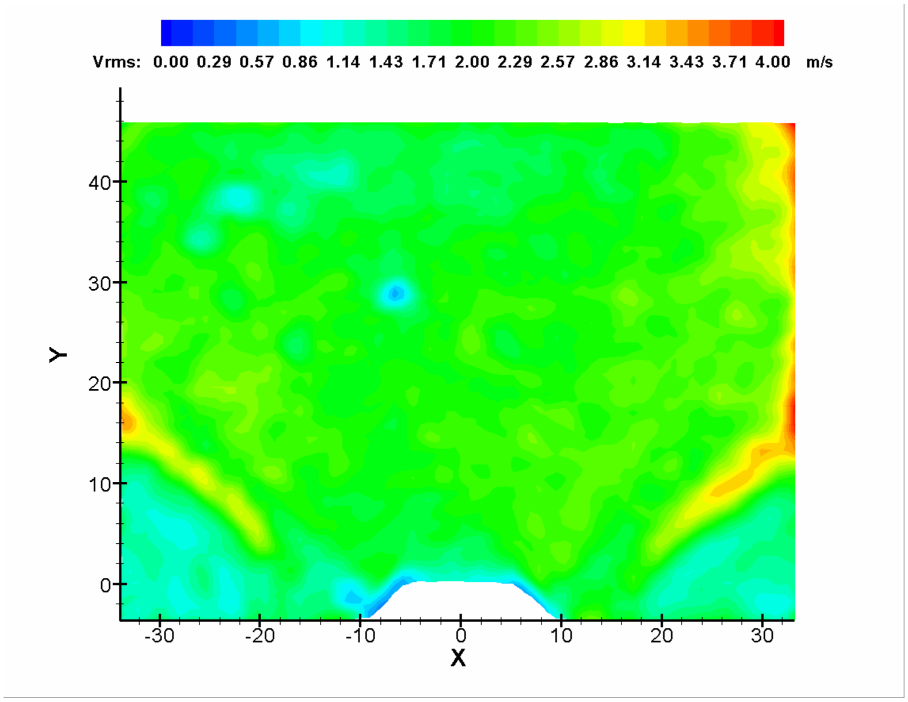

Figure 5.44 2-D Axial RMS Contour plot, $45^o/50^o$ co-swirl case, reacting condition, confined case

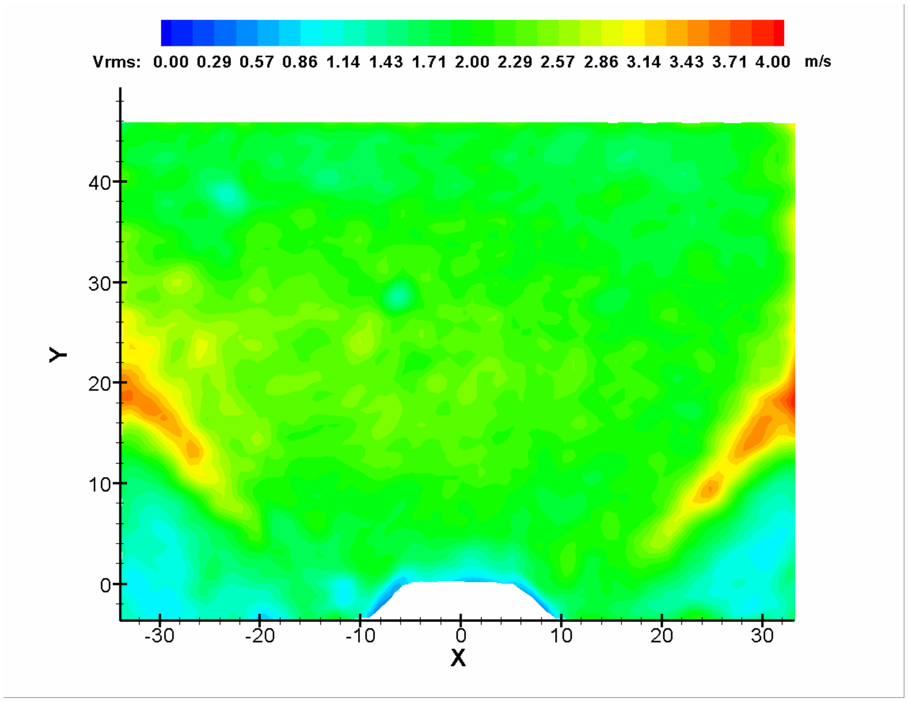

Figure 5.45 2-D Axial RMS Contour plot, $45^o/-50^o$ counter-swirl case, reacting condition, confined case

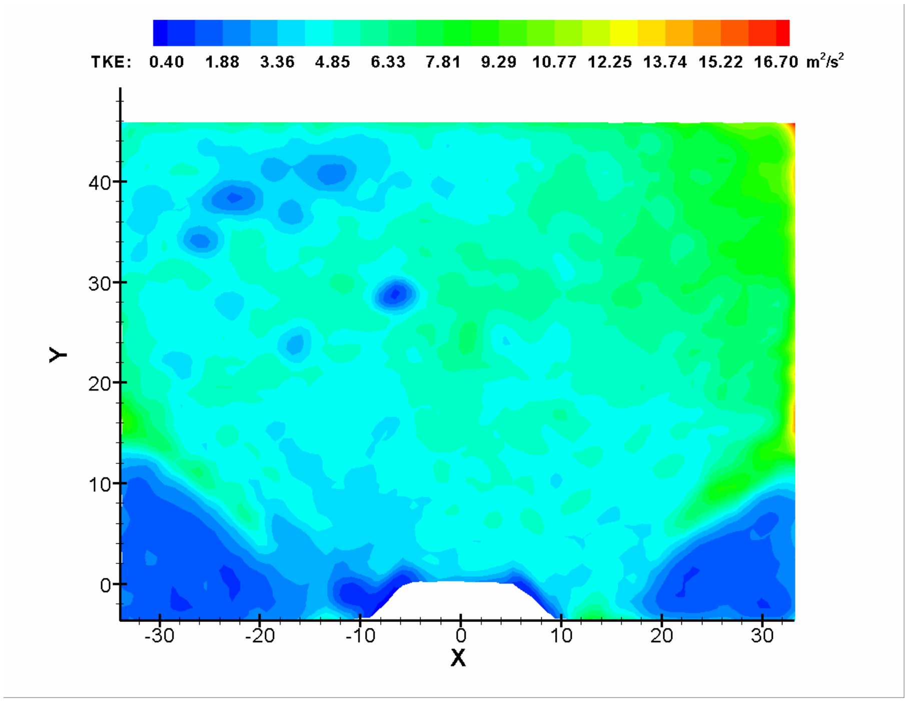

Figure 5.46 2-D Turbulent Kinetic Energy Contour plot, 45°/50° co-swirl case, reacting condition, confined case

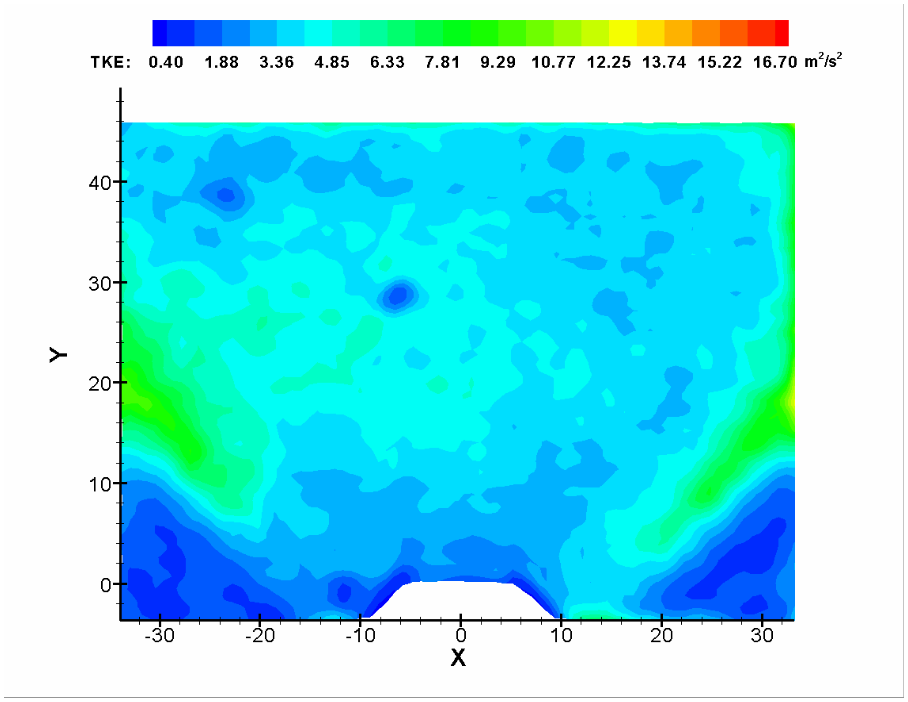

Figure 5.47 2-D Turbulent Kinetic Energy Contour plot, 45°/-50° counter-swirl case, reacting condition, confined case

Figures 5.44 – 5.47 show the axial rms and TKE for the reacting confined flowfields. Many of the trends seen in these figures have been discussed earlier. With confinement one achieves a greater uniformity of flow velocity and properties but not necessarily absolute magnitudes. Velocities can be abruptly terminated or dampened due to the wall effects of the enclosure. This plays a role in keeping velocity magnitudes and derived quantities to lower maximums than the unconfined flowfields. It is believed that the confined flame has a smaller residence time due to its shorter recirculation region. Also it is seen that the turbulence increases with combustion, which relates to increased mixing. Confinement enhances many of the general trends observed in unconfined flowfields.

5.2.5 Calculated Swirl Numbers and Entrained Mass Flowrate

Using the obtained PIV velocity data the swirl numbers for the investigated unconfined flows were determined. The equation for the swirl number calculation considering velocity field data is the following [8],

$$S=\frac{M_\varphi}{R_0 \cdot M_X} \tag{5.8}$$

S	swirl number
R_0	characteristic length (nozzle radius)
M_φ	angular momentum flux
M_x	axial momentum flux

$$M\varphi=\int w\cdot r\cdot\rho\cdot u\cdot 2\cdot\pi\cdot r\cdot dr \tag{5.9}$$

$$M_X=\int u\cdot\rho\cdot u\cdot 2\cdot\pi\cdot r\cdot dr \tag{5.10}$$

w	tangential component of the velocity
u	axial component of the velocity
ρ	fluid density

The calculated swirl number considering geometric considerations only for an inner swirler vane angle of 45° is 0.78 and the geometrically determined swirl number for an outer swirler vane angle of 50° is 1. The above geometrically determined swirl numbers are calculated using the following equation found in Gupta [8].

$$S=\frac{2}{3}\cdot\left[\frac{1-(d_h/d)^3}{1-(d_h/d)^2}\right]\tan\alpha \tag{5.11}$$

α	swirl vane angle
d	nozzle diameter
d_h	hub diameter

The combined geometrically determined swirl number is taken as the square root of the sum of the squares of the inner swirl number and outer swirl number. This is evaluated to be 1.27. Table 5.1 shows the calculated combined swirl numbers for the investigated flows using equations 5.8, 5.9 and 5.10. The velocity data used to calculate the swirl number in each case is at the far upstream point of the measurement region, which is the swirler exit plane.

Table 5.1 Calculated combined velocity field data swirl numbers for the investigated unconfined flows

Swirl Distribution and Condition	Calculated Swirl Number using velocity field data
45/50 co-swirl, non-reacting, unconfined	1.47
45/-50 counter-swirl, non-reacting, unconfined	1.21
45/50 co-swirl, reacting, unconfined	1.55
45/-50 counter-swirl, reacting, unconfined	0.99

The swirl number calculated using geometrical considerations is an over prediction of the swirl number calculated using velocity data in all unconfined counter-swirl cases. It under predicts the calculated swirl number for all unconfined co-swirl cases. This over prediction with equation 5.11 is expected as the geometrical swirl number is more of an ideal swirl number and does not account for momentum losses, flow perturbations, swirler interaction and hysteresis that can reduce swirl strength. The combined geometrical swirl number and the velocity calculated swirl number are in reasonable agreement. The observations of greater swirl strength for the counter-swirl condition are not verified with the calculated swirl number from velocity data at the swirler exit plane. The calculated swirl numbers due show what is expected, that the co-swirl condition imparts greater swirl strength. With the addition of combustion the co-swirl swirl strength increases while the counter-swirl swirl strength decreases. Possibly at the swirler exit plane the recirculation zone boundary is larger for the non-reacting counter-swirl case. A smaller recirculation zone boundary is possible for the counter-swirl case due to the increase in negative radial strain (acceleration of fluid toward the centerline) with combustion in this region. Gupta [8] showed that swirl strength increases with recirculation zone width. Interesting to see would be the downstream behavior of the calculated swirl number. The reverse flow velocity downstream, figure 5.48, is greater for the counter-swirl condition. This could provide for smaller axial momentum in the denominator of equation 5.7. Consequently, this could increase the calculated swirl strength. Confinement is expected to increase the reported swirl numbers for the unconfined condition

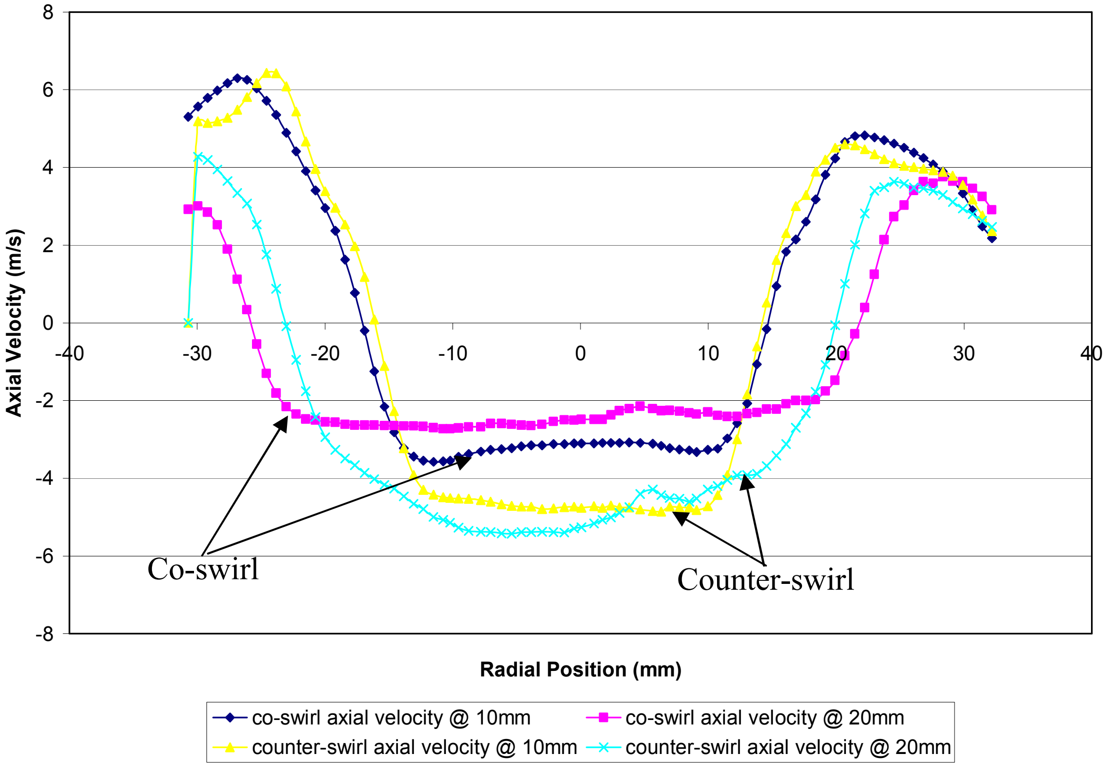

Figure 5.48 **Comparison of Axial Velocity at downstream locations for burning flowfields**

A measure of entrained mass flowrate is calculated using a relationship developed by Kerr and Fraser [9] for flat vane swirlers. This relationship is shown in eqn 5.12. The relationship shows that the entrained mass flowrate varies linearly with the downstream distance *x* according to the equation:

$$\frac{\dot{m}_e}{\dot{m}_{sw}} = (0.35 + 1.4S)\frac{x}{d_{eff}} \qquad (5.12)$$

m_e	entrained mass flowrate
m_{sw}	swirler mass flowrate
S	swirl number
x	downstream distance
d_{eff}	effective diameter

The effective diameter term is determined with the following equation

$$d_{eff} = (D_{sw}^2 - D_{hub}^2)^{0.5} \qquad (5.12)$$

D_{sw}	swirler diameter
D_{hub}	hub diameter

Table 5.2 shows the ratio of entrained mass flowrate to swirler mass flowrate for the unconfined investigated flows. The downstream *x* distance used is the maximum relative to the length of the internal recirculation zone.

Table 5.2 Calculated ratio of entrained mass flowrate to swirler mass flowrate for the unconfined flows

Swirl Distribution and Condition	Ratio of entrained mass flowrate to swirler mass flowrate
45/50 co-swirl, non-reacting, unconfined	1.668
45/-50 counter-swirl, non-reacting, unconfined	1.416
45/50 co-swirl, reacting, unconfined	2.417
45/-50 counter-swirl, reacting, unconfined	1.665

Combustor performance is influenced directly by the capacity of the swirler efflux to entrain combustion products. The relative proportions of air and burned products in the primary recirculation zone govern the temperature and equivalence ratio of the combustion process. And thereby control the rates of reaction and soot formation. From table 5.2 it is seen that the entrainment increases with combustion and that the co-swirl non-burning and burning conditions entrain more mass flow than the counter-swirl non-burning and burning conditions. The entrainment and other flowfield characteristics for the co- and counter- swirl conditions should be reflected in the optical emission spectroscopy images, the IR thermal images and the gas sampling emissions.

5.2.6 Internal Recirculation Zone Boundary

The internal recirculation zone boundary is determined from the velocity field data. The boundary between the main flow (jet outflow) and the reverse flow is located where the axial velocity is zero. Figure 5.49 shows the internal recirculation zone boundary for the non-reacting and reacting unconfined flowfields. Figure 5.50 shows the internal recirculation zone boundary for the non-reacting and reacting confined flowfields. These figures illustrate the region over which angular momentum fluxes are acting for the unconfined and confined, non-reacting and reacting flows. The internal recirculation zone boundaries help to support or explain the swirl strength calculated using velocity field data for the unconfined flows and the swirl strength observed for the confined flows. It is observed in the axial velocity field data for the co-swirl unconfined and confined flows that the positive axial velocity is greater for the co-swirl condition. For the unconfined flows the recirculation zone boundary is widest at the exit plane for the co-swirl cases. This supports the calculated greater swirl strength for unconfined co-swirl cases. It is also seen as suggested earlier that the boundary for the counter-swirl non-reacting case is wider than that of reacting counter-swirl case supporting that the non-reacting counter-swirl case have a greater swirl number. The confined boundaries suggest that confinement with combustion reduces swirl strength and that internal recirculation zone boundary alone is not sufficient to help in explaining and supporting swirl strength in a confined environment. One side is provided because zero velocity points at the swirler exit plane are obstructed by the fuel injector

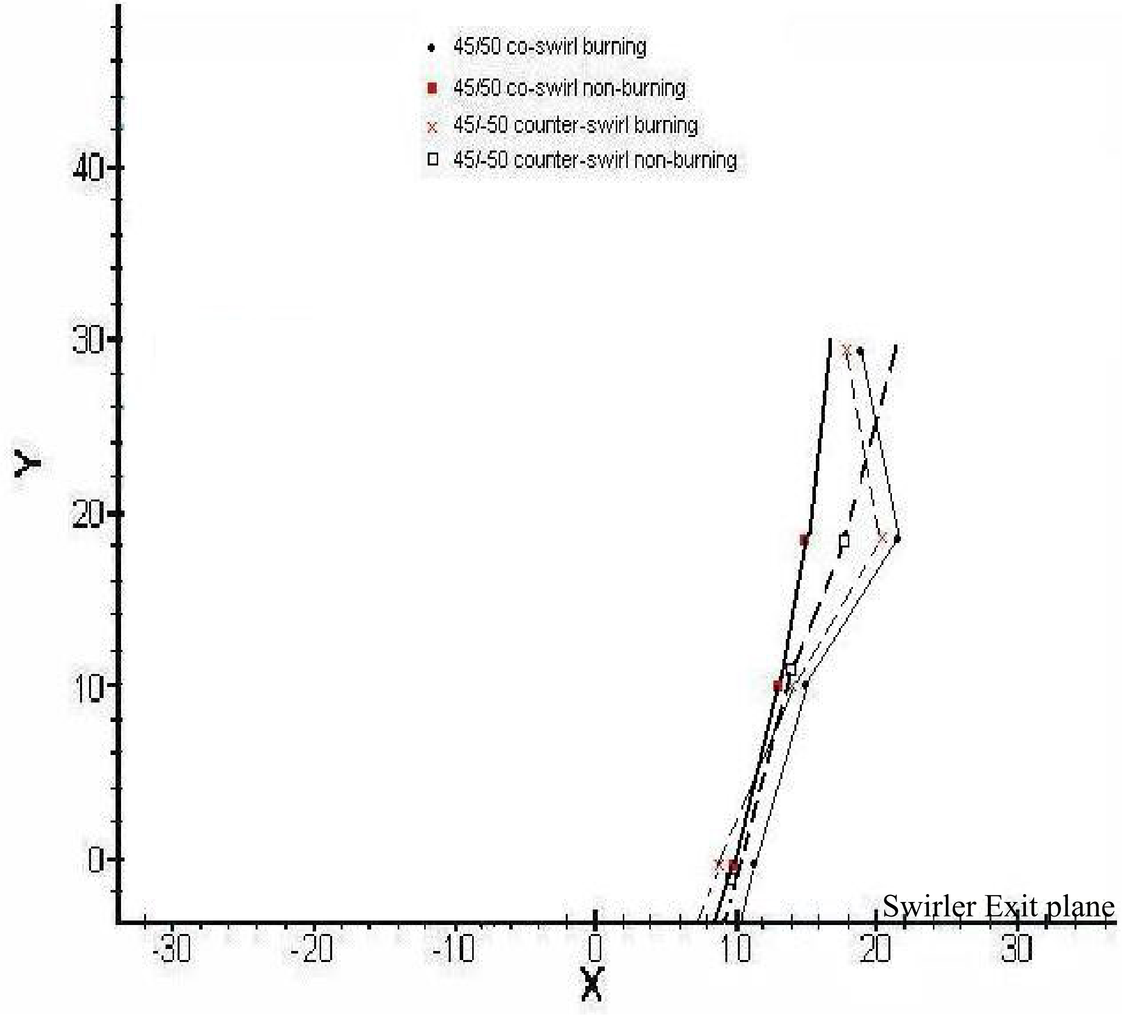

Figure 5.49 Sketch of Recirculation Zone boundaries for unconfined co- and counter- swirl non-reacting and reacting flowfields

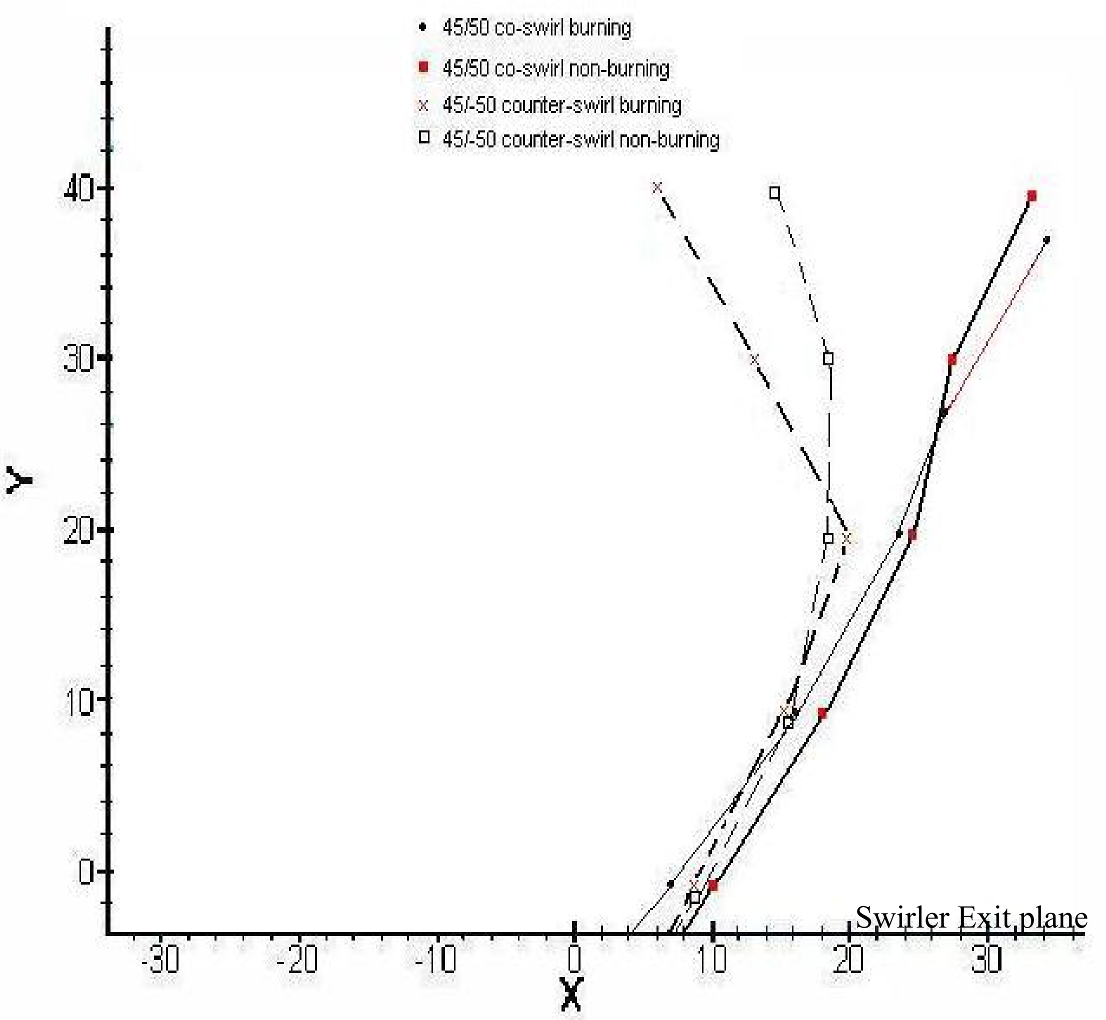

Figure 5.50 Sketch of Recirculation Zone boundaries for confined co- and counter- swirl non-reacting and reacting flowfields

5.3 Optical Emission Spectroscopy (OES)

The OES technique provides information on the chemical behavior of flames. The flame features can be observed with the use of the ICCD camera/detector and narrow bandpass filters. This technique relies on one of the most important features of the combustion of fuels such as hydrocarbons. That is emission of radiation at a wide range of wavelengths from the ultraviolet to infrared region. The flame radiations depend highly on the temperature of the flame and the reactive species present in the flame. The most prominent reactive species present in the flame are free radicals like CH, OH, C2, CN, and NH. These radicals can get excited at comparatively low energy levels and produces band spectra in visible or near ultraviolet region. They can be excited strongly by the limited temperatures of flames. The OH*, CH* and C2* radicals creates the strongest bands of the flames that can be detected by chemiluminescence. The chemiluminescence of flames is the result of radicals chemically generated directly on an excited state. Photons are then emitted during radiative deexcitation.

5.3.1 Distribution of 2-D CH* Radicals

Figure 5.51 shows the CH* distribution and intensity of the investigated flames. The images presented in this section are generated by WinView/WinSpec software. The images presented are the average of 30 sequential images that have an exposure time of 9 ms. The CH* radical is a marker of heat release zones in flames. The main chemical reaction commonly attributed to CH production and leading to chemiluminescence is [52];

$$C_2H + O \rightarrow CO + CH(A^2\Delta) \text{ and then: } CH(A^2\Delta) \rightarrow CH(X^2\Pi) + h\nu \qquad (5.13)$$

Equation 5.13 depicts the bonding of an oxygen atom with a carbon atom to form carbon monoxide thus creating an excited CH* radical (change at all locations). The resulting CH* radical then steps down to a lower energy level giving of energy in the form of light or photons.

The images in figure 5.51 show that the spatial volume decreases with change in swirl distribution from counter-swirl to co-swirl. CH* species intensity increases with the counter-swirl condition. The increase in the intensity of the CH* distribution supports the idea that the counter-swirl condition increases the rate of chemical reaction. The CH* species peak intensity distribution is over a larger region for the unconfined counter-swirl case. The unconfined co-swirl case (45°/50°) has more symmetrical radical distribution. This is because of less shear strength at interface of inner and outer annulus. The average intensity of combustion radicals increases with confinement of the flame. CH* intensity is greatest for 45°/-50° counter-swirl flame with and with out confinement. Uniform distribution of combustion radicals and wider radial distribution also results from confinement. The peak values or maxima of CH* intensity indicate the areas where reaction occurs in the flames. CH* intensity does not reduce to zero in the central region even though it is unlikely that much chemical reactions takes place there. This is due to chemiluminescence emissions, which occur in the background of the control volume.

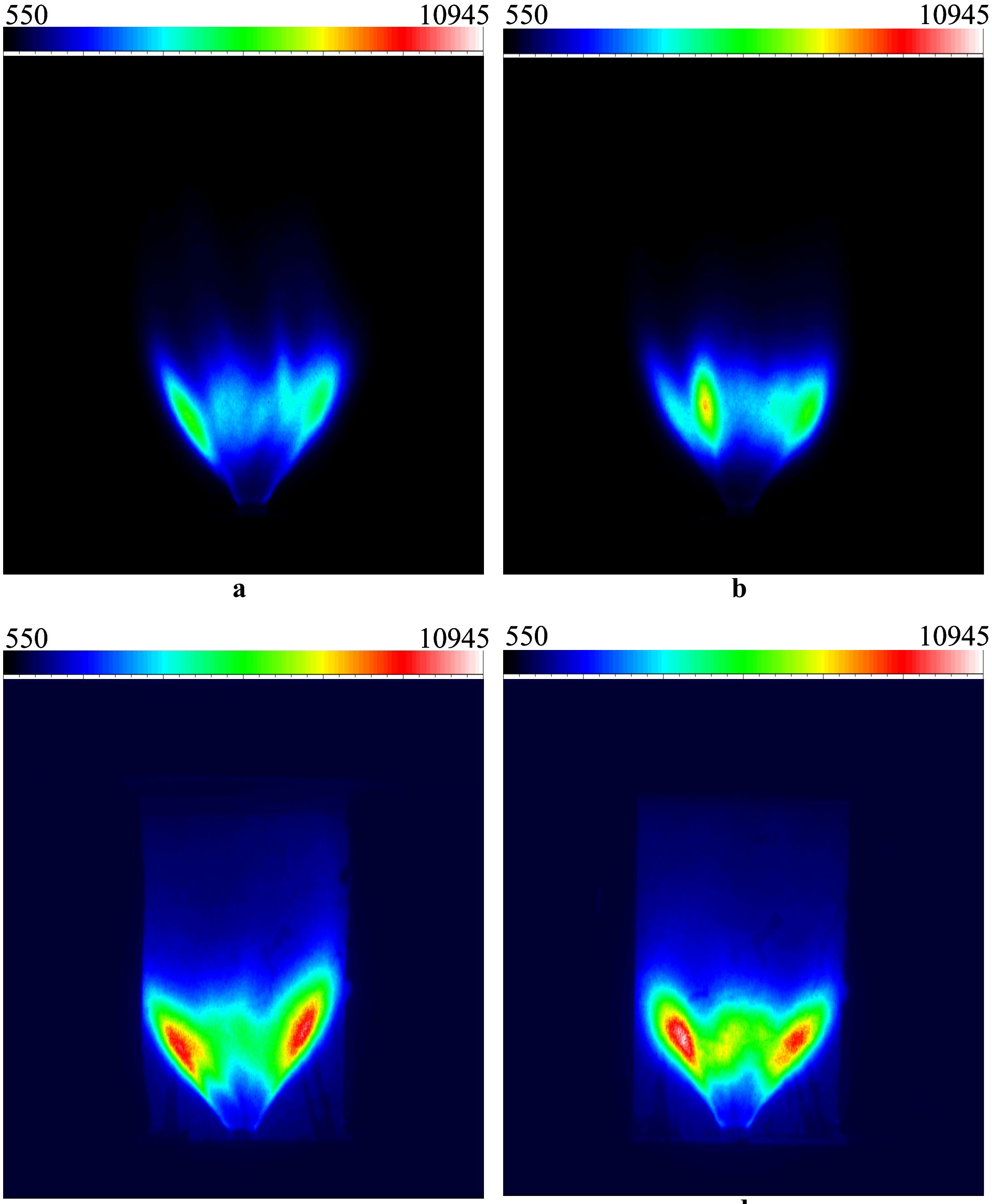

a b

c d

Figure 5.51 2-D Spatial distribution of CH intensity for unconfined and confined flames

a) Average CH image, unconfined condition, 45°/50° co-swirl

b) Average CH image, unconfined condition, 45°/-50° counter-swirl

c) Average CH image, confined condition, 45°/50° co-swirl

d) Average CH image, confined condition, 45°/-50° counter-swirl

5.3.2 Distribution of 2-D OH* Radicals

The OH radicals provide a marker of the flames reaction zone. Figure 5.52 shows the OH* intensity distribution of the flames. The images presented are the average of 30 sequential images that have an exposure time of 9 ms. The images presented in this section are also generated by WinView/WinSpec software. The main chemical reaction commonly attributed for OH production and leading to chemiluminescence is [52];

$$CH + O_2 \rightarrow CO + OH(A^2\Sigma) \text{ and then: } OH(A^2\Sigma) \rightarrow OH(X^2\Pi) + h\nu \tag{5.14}$$

Equation 5.14 depicts a CH radical attacking an oxygen molecule and forming carbon monoxide and an excited OH* radical. Subsequently the OH* radical gives light energy or photons upon reaching to the ground state.

Intensity of the OH* species increases for counter-swirl case. The volume, total image area of the OH* distribution decreases with counter-swirl condition. The reaction zone is more compact for the counter-swirl condition. This is attributed to greater mixing which can lead to enhanced combustion. OH* species distribution is more even for counter-swirl suggesting greater stability because of stronger mixing. For co-swirl (45°/50°) case, the time-averaged reaction zone, (OH) occurs predominantly at the regions of fluid interface.

In the confined condition, the reaction zones move radially inward with counter-swirl (45°/-50°). High intensity of OH* radical is found centrally. The confined co-swirl condition has larger OH* distribution than unconfined co-swirl condition. Reaction zones are more continuous for the confined co-swirl condition.

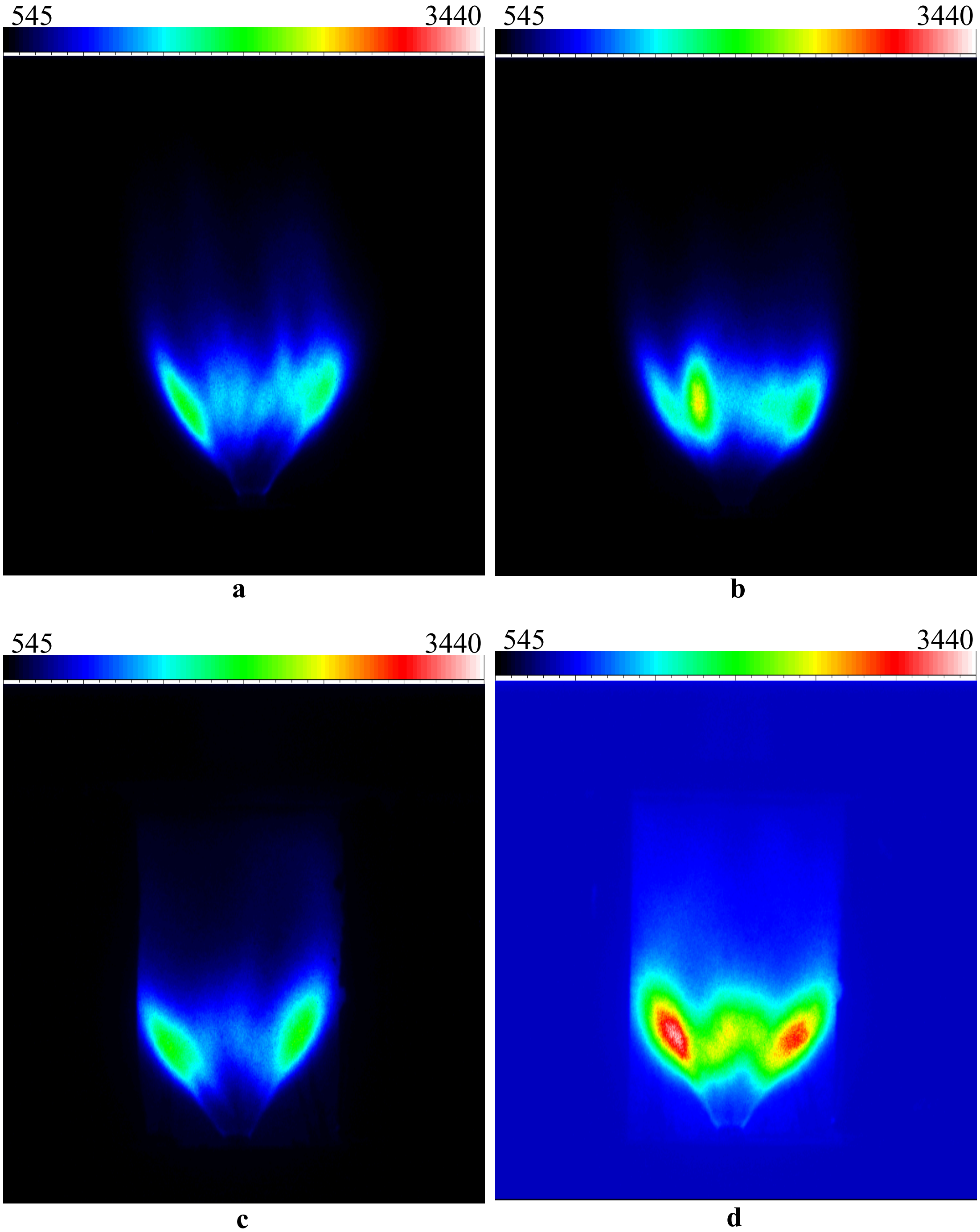

Figure 5.52 2-D Spatial distribution of OH intensity for unconfined and confined flames

a) Average OH image, unconfined condition, 45°/50° co-swirl
b) Average OH image, unconfined condition, 45°/-50° counter-swirl
c) Average OH image, confined condition, 45°/50° co-swirl
d) Average OH image, confined condition, 45°/-50° counter-swirl

The OH* intensity distribution is more continuous (larger) than CH* distribution; this suggests that most heat is released from smaller reaction zones.

5.3.3 Distribution of 3-D CH* and OH* Radicals

The 3-D images of the CH* and OH* radical were obtained after implementation of Abel inversion. Abel inversions of the images are performed via a developed Matlab code and the images presented are generated from the Matlab program. Figures 5.53 and 5.54 show the 3-D distribution of the CH* and OH* radicals, respectively.

These images clearly show the effect of swirl distribution and confinement on flame structure represented by the radical distribution. The counter-swirl condition promotes high radical luminous intensity closer to the center of the flame volume. This is apparent for the unconfined and confined conditions and is a result of the increased mixing of the counter-swirl condition. The counter-swirl condition reduces flame expansion due to the counter-rotating shear that promotes a strong mixing region between the inner and outer annuli. The PIV data showed that the turbulent kinetic energy was greater for co-swirl flows/flames. This implies that larger eddies are formed in the co-swirl condition. Also the vorticity fluctuation is greater for the counter-swirl condition. The influences of these characteristics manifest itself in the radical distribution in the location of the peak luminous intensities. Smaller eddies promote rapid mixing and significantly increases the momentum, heat, and mass transfer. In the 2-D radical distributions the relative comparison of the images can be skewed due to the thickness of the flame along the line of sight. The 3-D images obtained after Abel inversion are more readily compared. After closer examination of figures 5.53 and 5.54, it is seen that the intensity of the radical luminosity is greater for the co-swirl flames. This is not the result of better mixing or faster reactions but rather the result of the higher flame temperatures due to smaller reverse flow velocities and shear strain and vorticity regions seen in the PIV data. The weaker reverse flow, for co-swirl, provides slower entrainment, which increases residence time and the peak flame temperature, which influences the flame radical intensity. Yet, it is clearly seen that the counter-swirl condition promotes the chemical reaction based on more uniform high intensity regions with less fluctuation. Confinement enhances the intensity and radical production.

Figure 5.55 shows a relative comparison of CH* intensity along the radius from the center of the burner. The there is a large difference in location of peak intensity for the unconfined co-swirl and counter-swirl condition. This shows that confinement is a driving force on uniformity of flame structure. This is a result of the walls reducing the normal expansion of the flow and influencing the flow movement with the outlet of the combustor. A narrower distribution and less fluctuation in intensity are seen with the counter-swirl condition, both unconfined and confined. Again the turbulence created with the counter-swirl condition influences this observation. Turbulence is highly diffusive and rapid mixing is increased in the counter-swirl condition due to the increased vorticity fluctuation and smaller eddies of the counter-swirl condition depicted by the PIV data. Location of chemical reaction, intensity maxima and the rapid reduction in intensity seems to be influenced by a combination of factors. The intensity maxima lie on the boundary of the internal recirculation zone for the given flames. The varying swirl distributions influence the size and shape of the internal recirculation zone. Rapid reduction in intensity for the unconfined flames is primarily a function of air entrainment, which suppresses reactions. The counter-swirl flame internal recirculation zone width is smaller than the co-swirl flame internal recirculation zone width. This along with the enhanced mixing of the counter-swirl condition provides a less steep slope of intensity reduction. The unconfined flames do not have the plateau at the intensity maxima seen for the confined flames. This plateau is attributed to the more uniform flowfield produced in the confined environment along with less influence from surrounding air due to the combustor walls. PIV data shows that velocity magnitudes are constant further downstream along with less fluctuations for the confined flows this possibly helps the confined flames sustain the maximum intensity of their reactions.

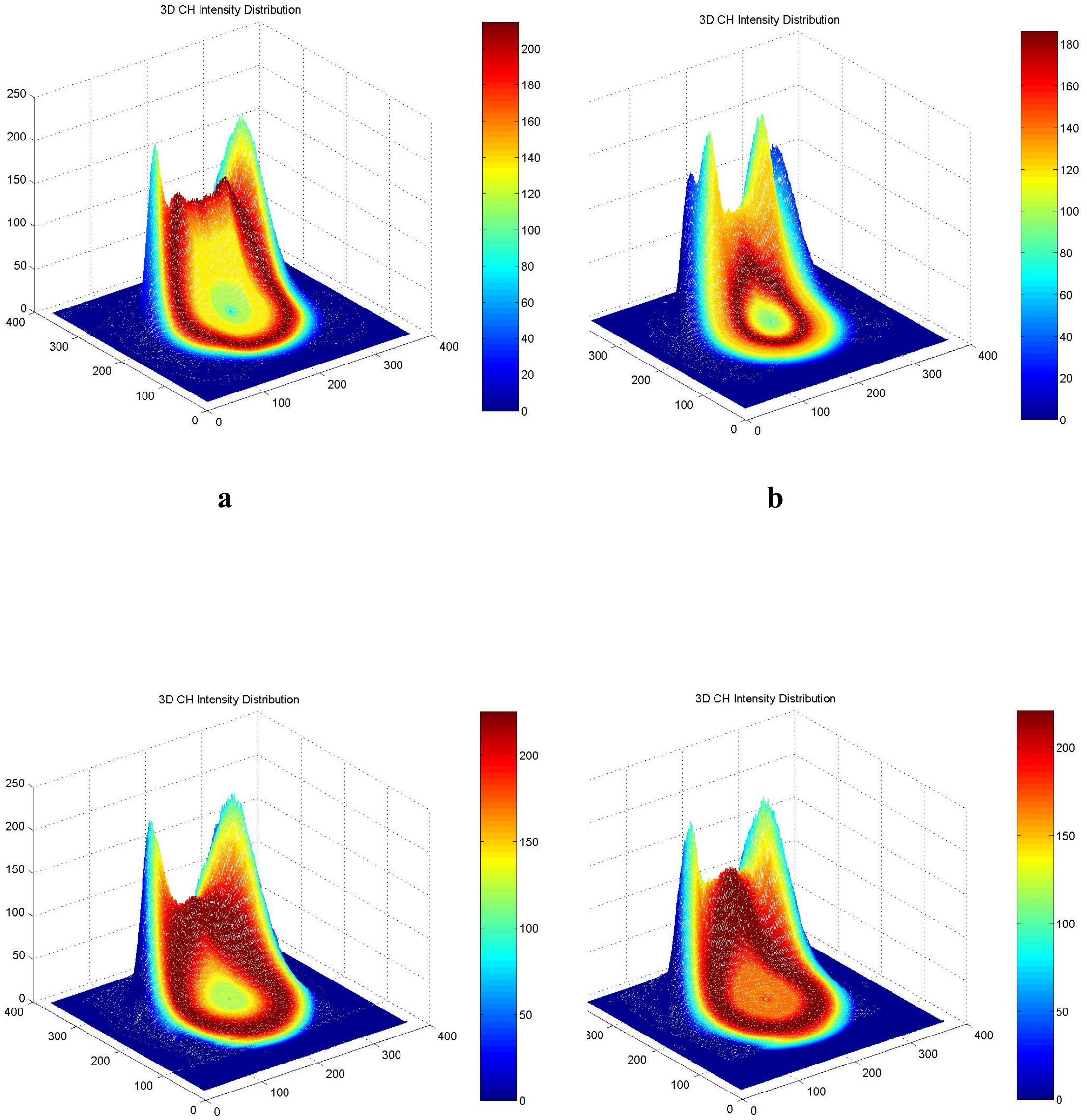

a

b

c

d

Figure 5.53 3-D Spatial distribution of CH* intensity for unconfined and confined flames

a) Average 3-D CH* image, unconfined condition, 45°/50° co-swirl

b) Average 3-D CH* image, unconfined condition, 45°/-50° counter-swirl

c) Average 3-D CH* image, confined condition, 45°/50° co-swirl

d) Average 3-D CH* image, confined condition, 45°/-50° counter-swirl

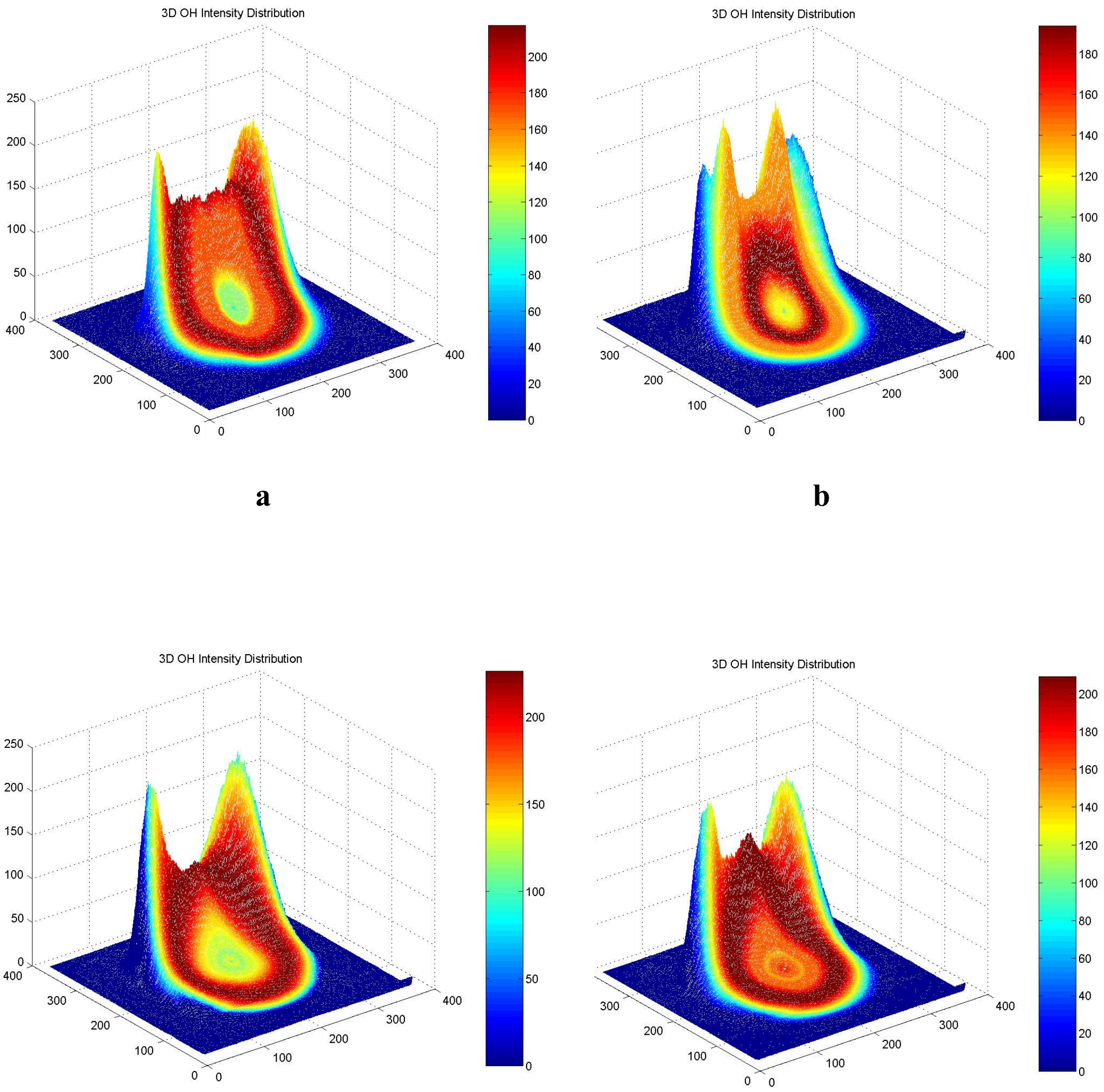

a b

c d

Figure 5.54 3-D Spatial distribution of OH* intensity for unconfined and confined flames

a) Average 3-D CH* image, unconfined condition, 45°/50° co-swirl

b) Average 3-D CH* image, unconfined condition, 45°/-50° counter-swirl

c) Average 3-D CH* image, confined condition, 45°/50° co-swirl

d) Average 3-D CH* image, confined condition, 45°/-50° counter-swirl

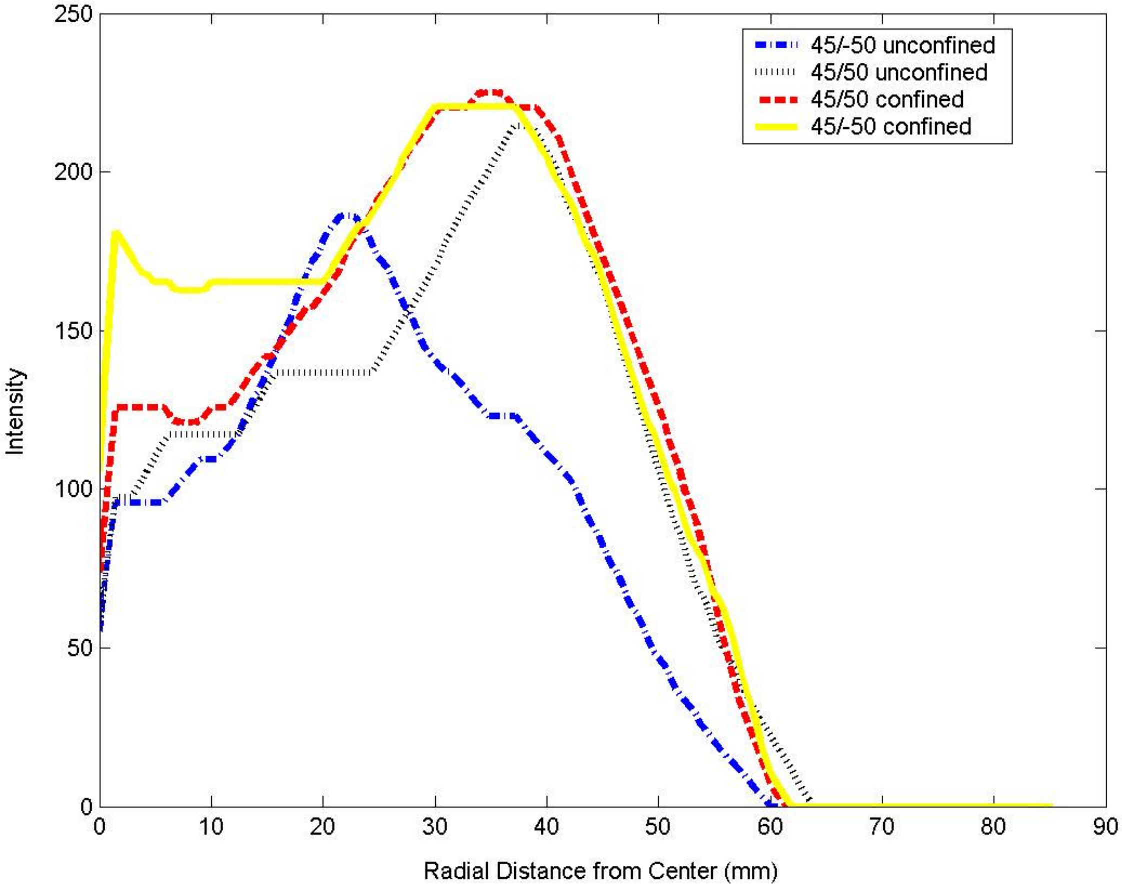

Figure 5.55 Comparison of CH* distribution along the radius for unconfined and confined flames over length of flame

5.3.4 Calculated Vibrational Temperature Distribution

By comparing the emission intensities of two bands of C_2* occurring from the same electronic transition, the vibrational temperature distribution have been from the measured C_2 radical distribution in the flames. Figure 5.56 shows the vibrational temperature distributions for the unconfined and confined flames.

The temperature distribution images suggest that the reaction zones for the unconfined and confined regions differ in their formation. The confined flames have radially stretched temperature distributions. The temperature distributions for the unconfined flames suggest the reaction region is long and axially stretched. The temperature distributions for the confined flames suggest that the reaction regions are flatter, thus more radially expanded than their unconfined counterparts. Zones of high strain are good indicators of regions of chemical reaction. Examining figures 5.57 and 5.58, a comparison of the axial strain for the co-swirl unconfined and confined conditions, and the differences in temperature distribution shape are explained. It is clearly seen that the confined flame high strain region is flatter in shape/angle than the unconfined high strain region. The high strain regions are highlighted by a box in the figures. This observation is attributed to the influence of the combustor walls forcing the flowfield movement to preferentially radially expand. The temperature distributions of figure 5.56 also show that close to the burner exit the temperature is not the maximum due to the formation of strong recirculation zones for all the flames. In the images maximum temperature occurs further downstream for all flames. This is consistent with swirling flow flowfields in that the reactions take place in the shear layer region and bulk fluid movement, which carries the heat, propagates downstream with only a portion entrained into the recirculation region to ignite the unburned fuel and air. The effect of swirl distribution on the temperature distribution is identified as a decrease in high temperature region volume for a counter-swirl distribution. The continuousness of the high temperature region for the co-swirl distribution is a result of slower reverse flow velocity and poor balance between air and combustion products in the internal recirculation zone. The confined condition also produces a more homogeneous temperature distribution. This homogeneity can be attributed to less fluctuation in the flowfield characteristics for confined flows. It shows that confinement enhances flame stabilization. It is possible that lean flammability limits could be extended with a favorable confined environment, thus leading to higher thermal efficiencies.

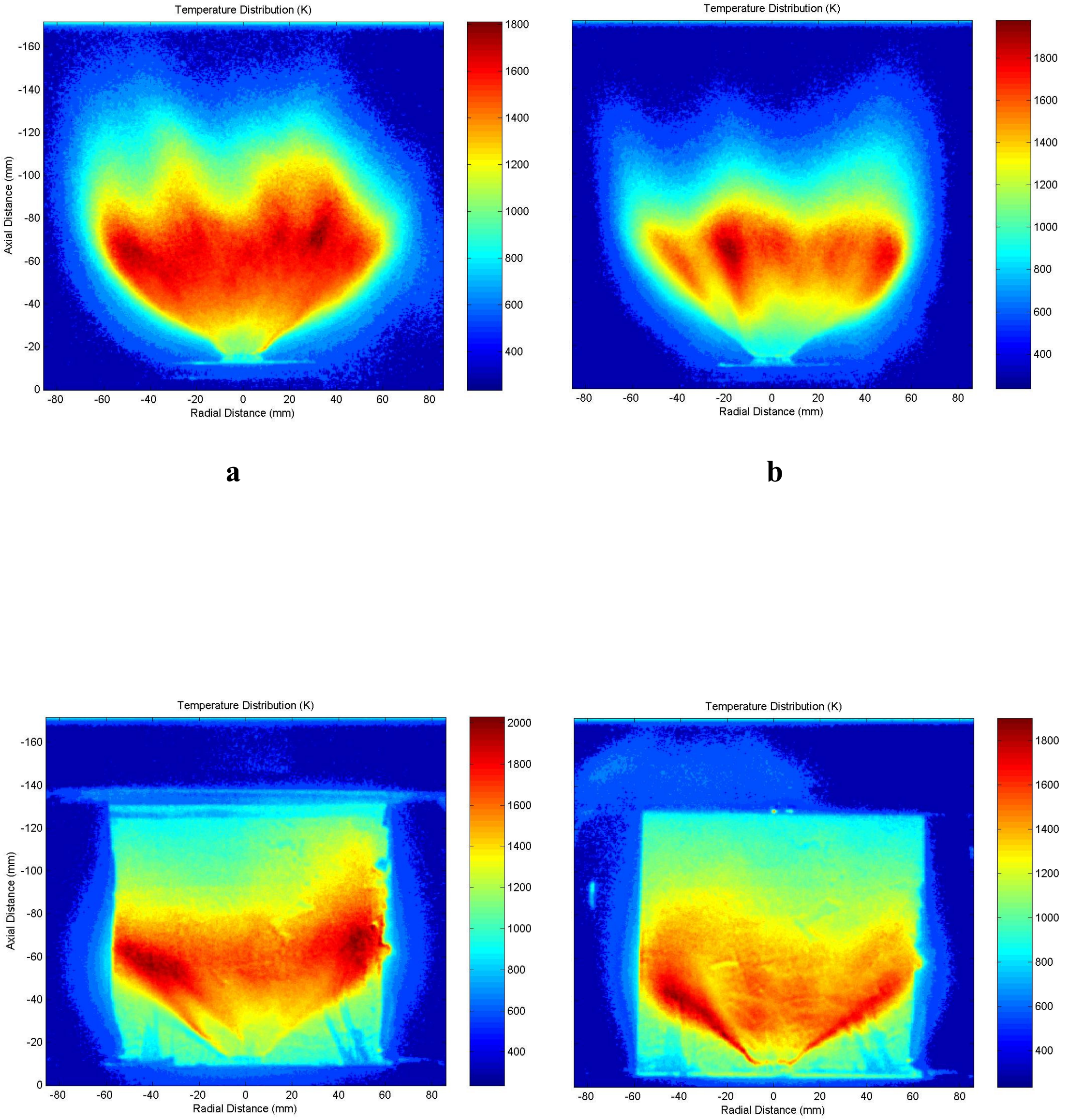

a

b

c

d

Figure 5.56 Vibrational Temperature Distribution (K), within the flame for unconfined and confined flames

a) Vibrational Temperature distribution image, unconfined condition, 45°/50° co-swirl

b) Vibrational Temperature distribution image, unconfined condition, 45°/-50° counter-swirl

c) Vibrational Temperature distribution image, confined condition, 45°/50° co-swirl

d) Vibrational Temperature distribution image, confined condition, 45°/-50° counter-swirl

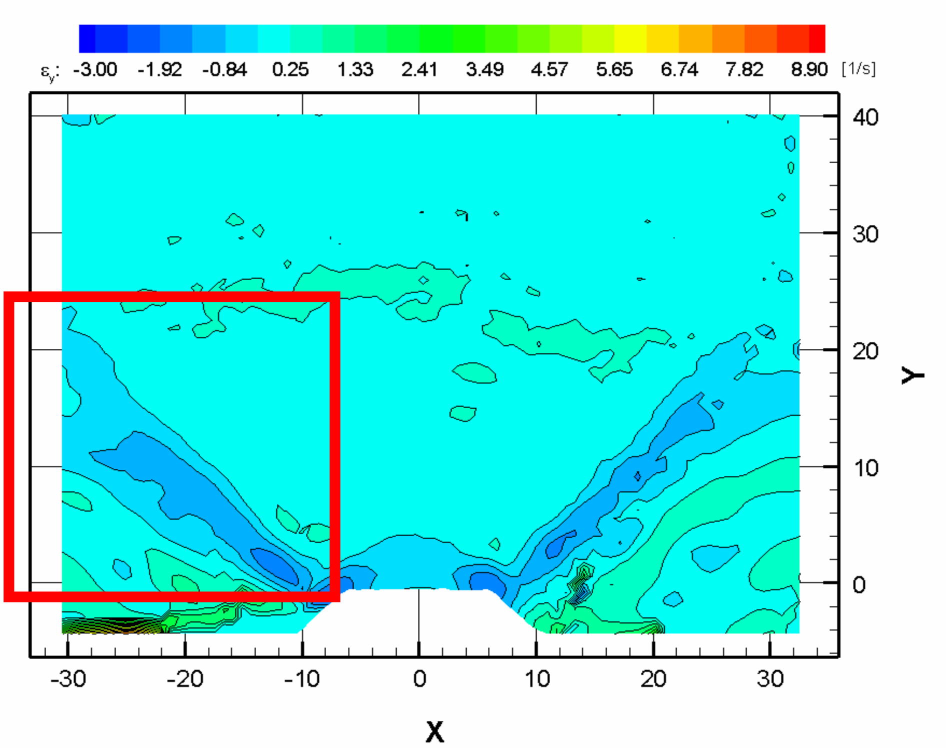

Figure 5.57 Axial Strain contour plot, 45°/50° co-swirl case, burning condition, unconfined case

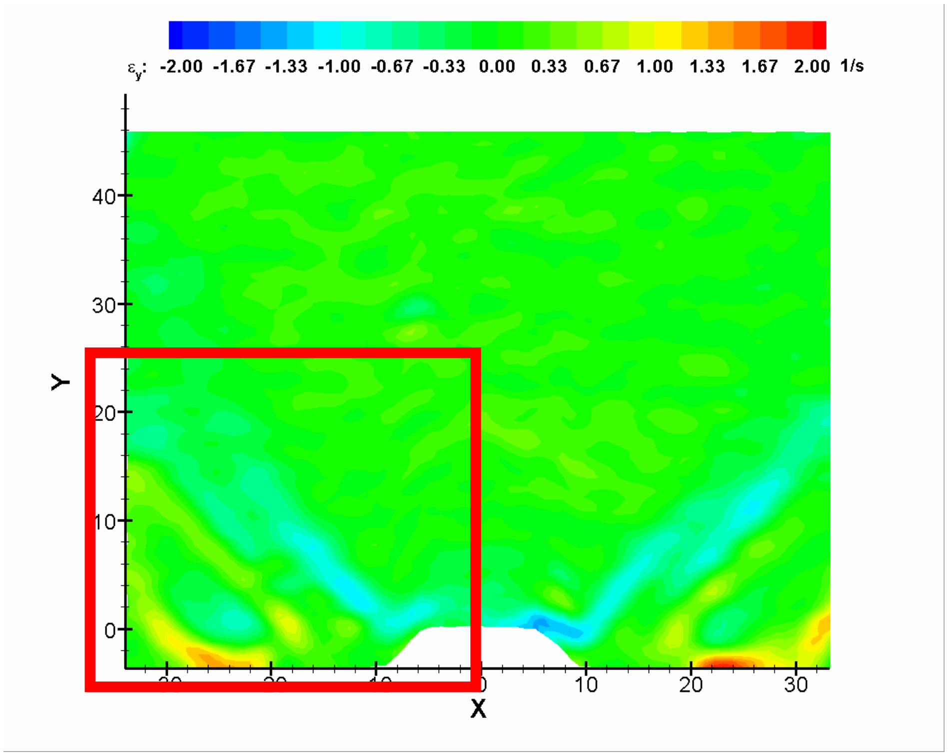

Figure 5.58 Axial Strain contour plot, 45°/-50° counter-swirl case, burning condition, confined case

5.4 Infrared (IR) Thermometry

IR thermal field images of the flame have been obtained using a long range infrared camera attached with an optical sensor to analyze infrared light emitted by hot combustion products. Hot combustion gases and species emit radiations in the infrared region of the electromagnetic spectrum. The infrared camera captures and images the emitted infrared radiations from an object, in this case a hydrocarbon flame. The radiance captured by an infrared camera depends mainly on object temperature, background temperature and emissivity of the source object. The camera and software captures sequential frames from the investigated flames at 60 Hz. In the flame environment, radiations emitted in the infrared region are produced mainly by hot combustion products such as, CO_2, H_2O, CO, NO_x and soot. The time averaged images of approximately 300 frames are presented in this investigation. Matlab is used to average the frames and display the thermal distribution as a function of temperature in degrees Kelvin.

Figure 5.59 shows the 2-D IR thermal distributions for the two unconfined flames. As stated earlier, due to non-transmittance of the quarts glass the confined IR thermal distributions could not be obtained.

The co-swirl distribution provides a thinner more elongated thermal field. It also provides a greater IR temperature. This elongated thermal field is a product of the shape and formation of the internal recirculation zone observed in the PIV data for the unconfined co-swirl condition. The counter-swirl condition provides a more uniform thermal field. It is reasoned that the counter-swirl condition provides better mixing which allows for a more uniform thermal field. Flowfield data obtained with the use of particle image velocimetry supports the hypothesis of better mixing for a counter-swirl condition compared to the co-swirl condition. This observation is for the unconfined reacting flowfields.

The volume of the high temperature region is also greater for the 45°/50° co-swirl condition as seen in the vibrational temperature images. Again this is the effect of the increased balance of air and combustion products entrained with faster reverse flow velocity produced with the counter-swirl condition. The IR temperature distributions coincide well with the calculated vibrational temperature distributions. Both methods produce thermal distributions that show similar trends and the data from each method supports the other. The two sets of images, vibrational temperature distribution and IR thermal images, lead one to conclude that the thermal strain imposed by the counter-swirl condition is greater. This is clearly represented by the larger regions of peak temperature seen in the co-swirl conditions.

The strong mixing in the counter-swirl condition leads to rapid temperature changes that result in temperature field asymmetries

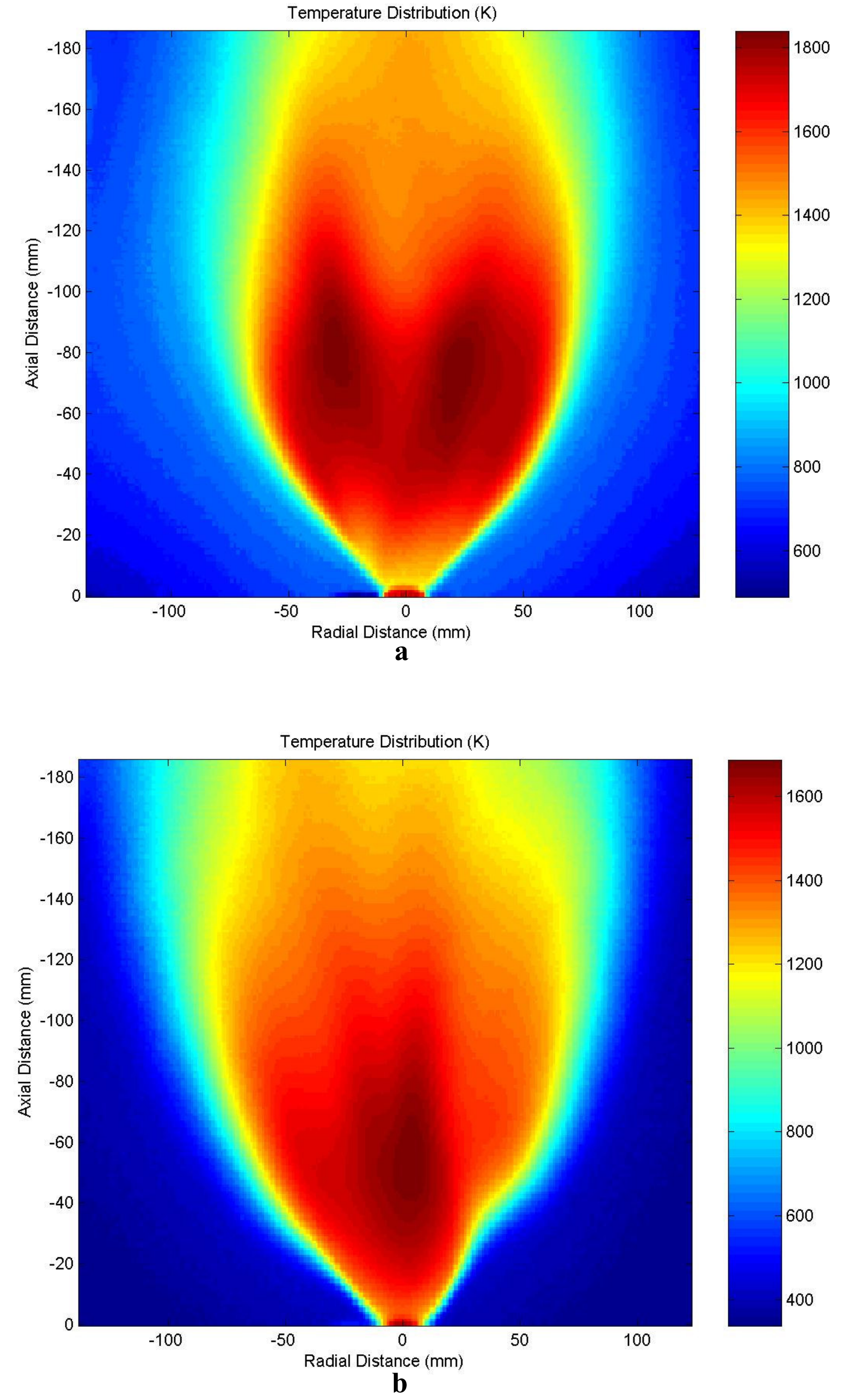

Figure 5.59 IR Temperature Distribution (K) for unconfined flames
a) Average IR image, unconfined condition, 45°/50° co-swirl (top)
b) Average IR image, unconfined condition, 45°/-50° counter-swirl (bottom)

5.5 Thermocouple Temperature Measurement

Downstream temperature profiles are obtained with a micro-thermocouple for the unconfined flames only. The effect of the micro-thermocouple on the flow is negligible [12, 46]. The confined environment does not allow for the desired probing locations therefore the micro-thermocouple measurements are not attempted for the confined flames. The thermocouple measurements provide another view of the thermal behavior of the investigated unconfined flames. The obtained temperature profiles are composed of 23 radial positions at 4 downstream axial positions. The graphs show the uncompensated temperatures and compensated temperatures. Compensation is needed to incorporate and account for the response time and radiative losses of the thermocouple probe.

The compensated raw temperature data is obtained by means of post processing with an IDL (Iterative Data Language) program first developed by Marshall, [12]. The post processing is performed on a Sun workstation. Post processing with the IDL program also provides micro- and integral- thermal time scales, probability density functions, and power spectra. This added data also gives insight into the lean direct injection flame behavior. The obtained temperatures and thermal time scales are discussed below.

Figures 5.60 and 5.61 show the temperature profiles for the unconfined 45°/50° co-swirl flame and the unconfined 45°/-50° counter-swirl flame respectively. Maximum temperature is measured at the initial downstream location for both flames, at a distance 95 mm above the swirler exit plane (approximately 1.5 times the burner diameter). As you move further downstream, the temperature profile values decrease.

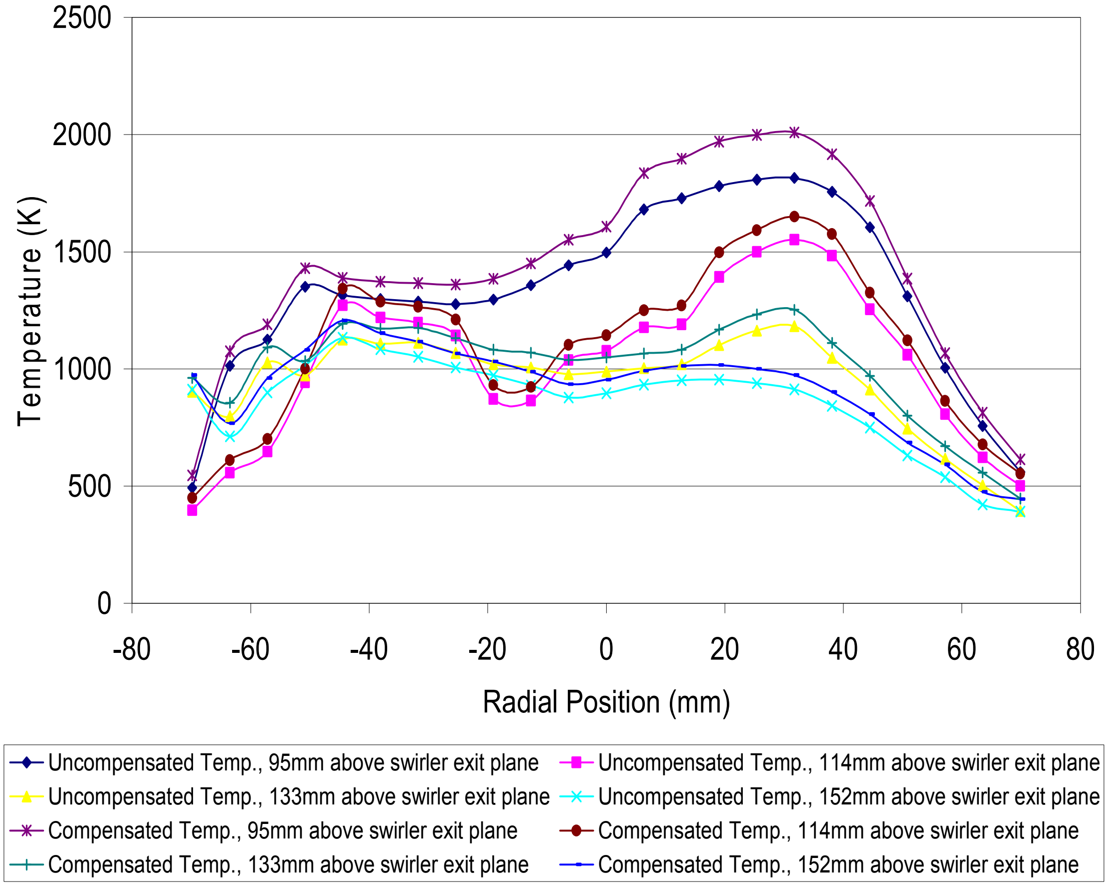

Figure 5.60 Uncompensated and Compensated Downstream Temperature Profile for the Unconfined 45°/50° Co-swirl Flame at 95, 114, 133, and 152 mm downstream from swirl exit

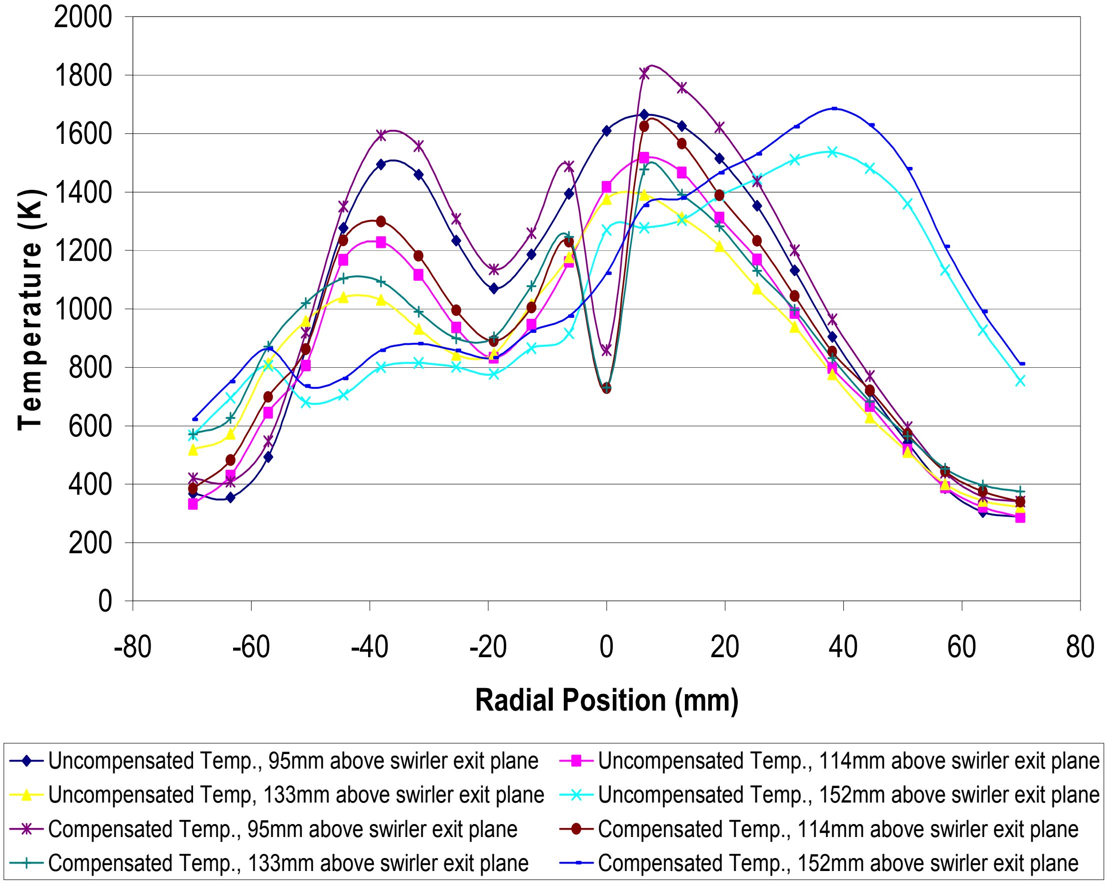

Figure 5.61 Uncompensated and Compensated Temperature Profile for the Unconfined 45°/-50° Counter-swirl Flame at 95, 114, 133, and 152 mm downstream from swirl exit

The co-swirl flame temperature profiles, figure 5.60, are flatter, thus at a higher constant temperature than those of the counter-swirl flame, figure 5.61. This is a reflection of the mass flow entrainment, mixing, and size of the vorticity and shear strain regions seen in the co-swirl flame. The co-swirl temperature profiles do not show a strong temperature dip in the center of the temperature profile like the counter-swirl temperature profiles. The counter-swirl temperature profiles have this large temperature dip due to its greater reverse flow velocity and mass flowrate entrainment. The counter-swirl temperature profiles have a smaller difference between their overall maximum and minimum values. This is a desired trend and is reflected in the calculated vibrational temperature and IR temperature distributions. The small overall maximum and minimum temperature difference for the counter swirl temperature profiles, figure 5.61, is attributed to greater mixing and smaller local eddies. The temperature profiles exhibit asymmetry due to the varying location of large vortical structures, the general turbulence nature, local flowfield disturbances/perturbations and influence from a precessing vortex core.

The thermal time scales calculated for the two unconfined flame conditions also provide very interesting information. Table 5.3 gives a comparison of average integral- and micro- time scales at the each of the 4 distances above the swirler exit plane for the unconfined co- and counter- swirl conditions. The thermal integral-time scales provide insight on the size of large scale eddies in the fluid flow. The integral-time scales for the co-swirl flow are much larger than those for the counter-swirl flow. These results coincide well with insight and observations obtained from the

PIV data. It was discussed earlier that the co-swirl condition is thought to produce larger vortical structures and the integral-time scales substantiate this observation.

Table 5.3 Comparison of Average Integral- and Micro- thermal time scales for the unconfined flames using compensated micro-thermocouples

	Co-swirl, 45°/50°, reacting, unconfined		**Counter-swirl, 45°/-50°, reacting, unconfined**	
Distance above swirler exit plane (mm)	Average Integral-time scales (ms)	Average Micro-time scales (ms)	Average Integral-time scales (ms)	Average Micro-time scales (ms)
95	10.71	2.27	8.30	2.48
114	13.07	2.90	10.26	2.85
133	14.77	3.30	9.99	2.86
152	13.91	3.55	8.40	2.35

The large values of integral time scales along with the high temperatures can also play a role in the pollutant formation for the co-swirl condition. Those combined factors of large integral-time scales and high temperatures can work together to enable a high emission of NO_x and other undesirable pollutants.

The micro-time scales provide insight on fluid flow mixing, eddy speed, and thermal fluctuation. From the observed micro-time scales it is clearly seen that fluid mixing and eddy speed is better and more consistent for the counter-swirl condition. Again this is first observed with the PIV flowfield data and substantiated with the thermal time scales.

5.6 Emissions Measurement

The emission data provides an opportunity to look into the completeness of the combustion in the investigated flames and the concentration of the resultant products of combustion. Observing the emissions from the simulated lean direct injection flames of this investigation allows one to make some remarks about the reaction mechanism of the lean fuel air mixture. One can get an understanding of the formation mechanism in combustion from the concentrations of NO_x/NO. A key observation is whether the emission data agrees with temperature distribution and how the observed flowfield information may have led to the observed emissions. It is expected that the higher the mean temperature the lower the emission of CO and unburned hydrocarbon (UHC), and the higher the emission of CO_2. With high emissions of UHC and CO, it is considered to be a sign of more incomplete combustion, which is undesirable. It is seen that the counter-swirl condition produce stronger turbulence than the co-swirl condition. It is also seen that the co-swirl condition tends to provide a longer thinner thermal field and a longer flowfield with slower reverse flow velocity. This could result in the thermal stretch phenomenon and increase the time of the combustion process.

Emissions data is sampled from the centerline of the investigated flames over a 5 minute period and averaged. The height of the probe for all measurements was approximately 2.5 burner diameters (162.5 mm).

5.6.1 NO emission

It was observed that both confinement and swirl distribution had an effect on the emission of nitric oxide (NO). Both the unconfined and confined co-swirl

(45°/50°) conditions produced higher amounts of NO compared to their counter-swirl counterparts. It should be noted that these quantities are not corrected for O_2 concentration; therefore the differences in magnitude could change significantly. The effect of the swirl distribution and confinement should not be altered. Figure 5.62 shows a graph of the NO emission for the investigated flames. It is interesting to see that when comparing the emission of NO to the intensity levels of the 2-D CH* images, it is seen that the high NO emissions correspond to low intensity levels of CH* which is a marker of heat release rate. It must be noted that the formation of NO is several orders of magnitude slower than the main heat release reactions and is thus kinetically limited. The higher NO emissions indicate higher temperature and longer residence times or slower reverse flow velocities. Also the size of the internal recirculation zone and flowfield formation can influence the emission of NO. The observed flowfield (PIV) data shows the co-swirl conditions, unconfined and confined, have longer internal recirculation zones and elongated flowfields. This can be seen in the axial velocity and strain rates contour plots. The confined geometry is responsible for the higher emission of NO compared to the unconfined flames. This indicates the influence of higher overall temperatures and longer internal recirculation zones for the confined flames. These differences can be attributed to the lack of significant surrounding air entrainment and dilution and also the influence of the walls to increase radial velocity while decreasing axial velocity.

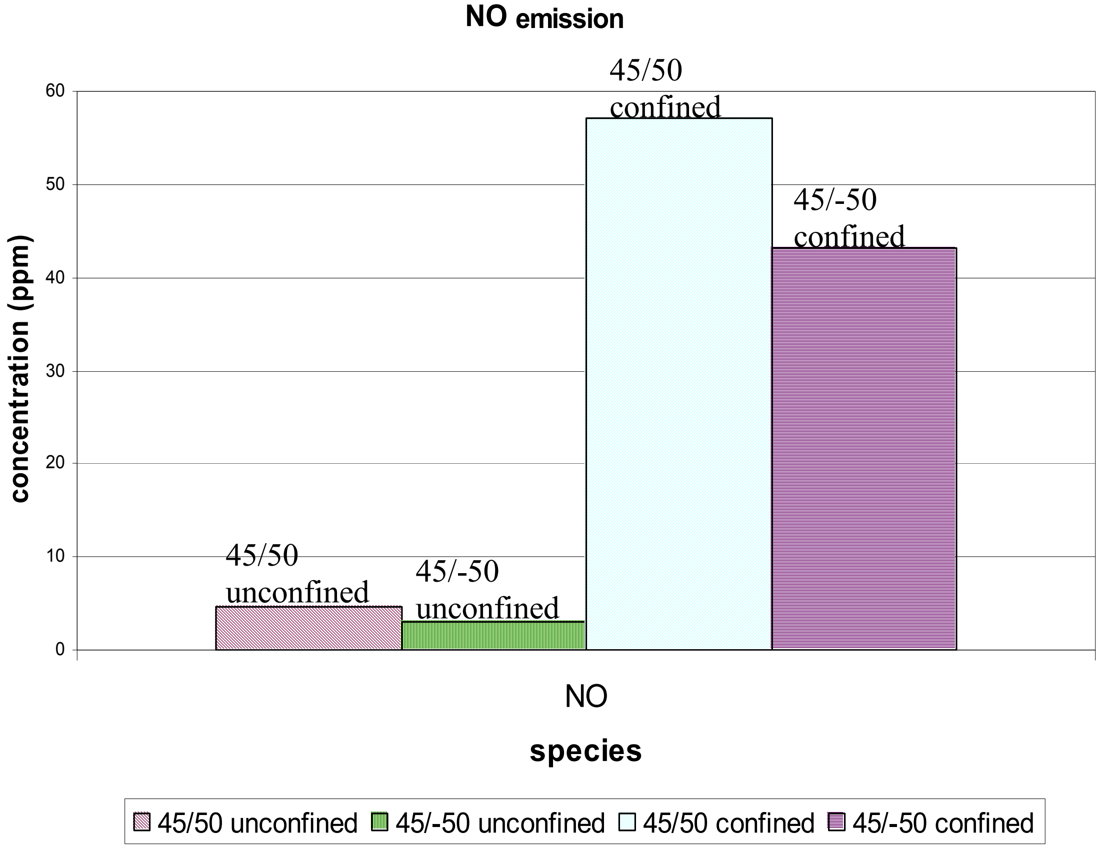

Figure 5.62 Graph of average centerline NO emission for unconfined and confined flames taken at 162.5 mm downstream from the swirler exit

5.6.2 CO emission

Figure 5.63 is a graph of the carbon monoxide (CO) emission from the investigated flames. It should be noted that these quantities are not corrected for O_2 concentration. The unconfined flames emitted the highest percentage of CO. It is reasoned that in the unconfined environment this increased CO emission is due to the surrounding air entrainment. The entrainment of this air reduces the effective combustion thus promoting incomplete combustion in the unconfined flames. CO emission is greatest for the unconfined co-swirl (45°/50°) flame. This is believed to be due in part to the slower mixing and chemical reactions. These mechanisms of slow mixing and chemical reactions are seen in the flowfield data, represented by the lower turbulence levels and slower reverse flow velocities and initially faster shear layer velocities. The initial accelerated shear layer velocities can act to stretch the flame environment thus promoting the formation of CO. The stretch of the flame is proportional to the axial velocity. High axial velocity will increase the stretch of the flame. Stretching of the flame can hinder complete reaction by elongating the internal recirculation zone and reducing the effective residence time. In the confined flames it is seen that the CO emission is highest for the counter-swirl condition. This is accounted for by the presence of increased mean temperature in the co-swirl confined condition. As stated earlier temperature does effect the formation of CO and high mean temperatures that are seen to be present in the confined co-swirl flames are reducing the emission of CO. This is effectively being achieved through dissociation of the CO compound because of the large volume of high temperature.

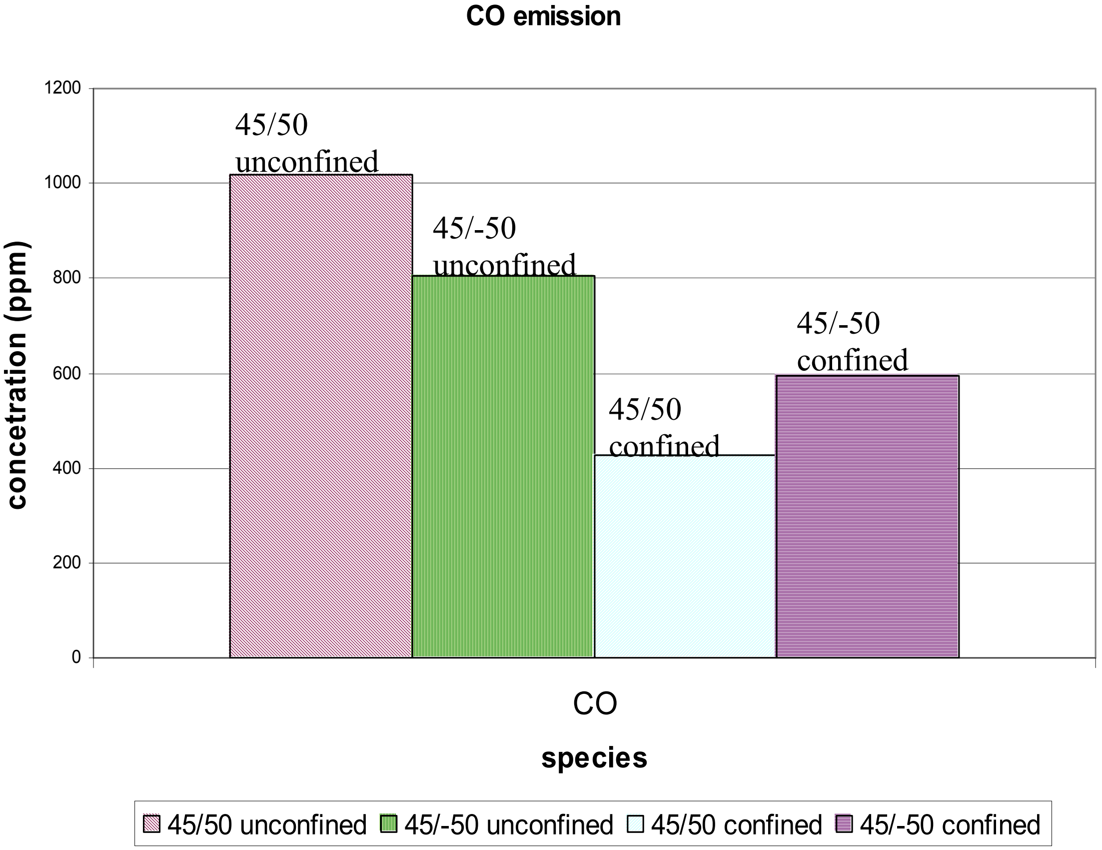

Figure 5.63 Graph of average centerline CO emission for unconfined and confined flames taken at 162.5 mm downstream from the swirler exit

5.6.3 CO_2 emission

As expected the carbon dioxide (CO_2) emission increased with confinement. The differences in swirl distribution are negligible. The graph of CO_2 emission for the investigated flames can be seen in figure 5.64. The more complete combustion process takes place in the confined environment. This observation is supported by the CH and OH flame radical images, which shows an increase in reactions as a result of the confined environment.

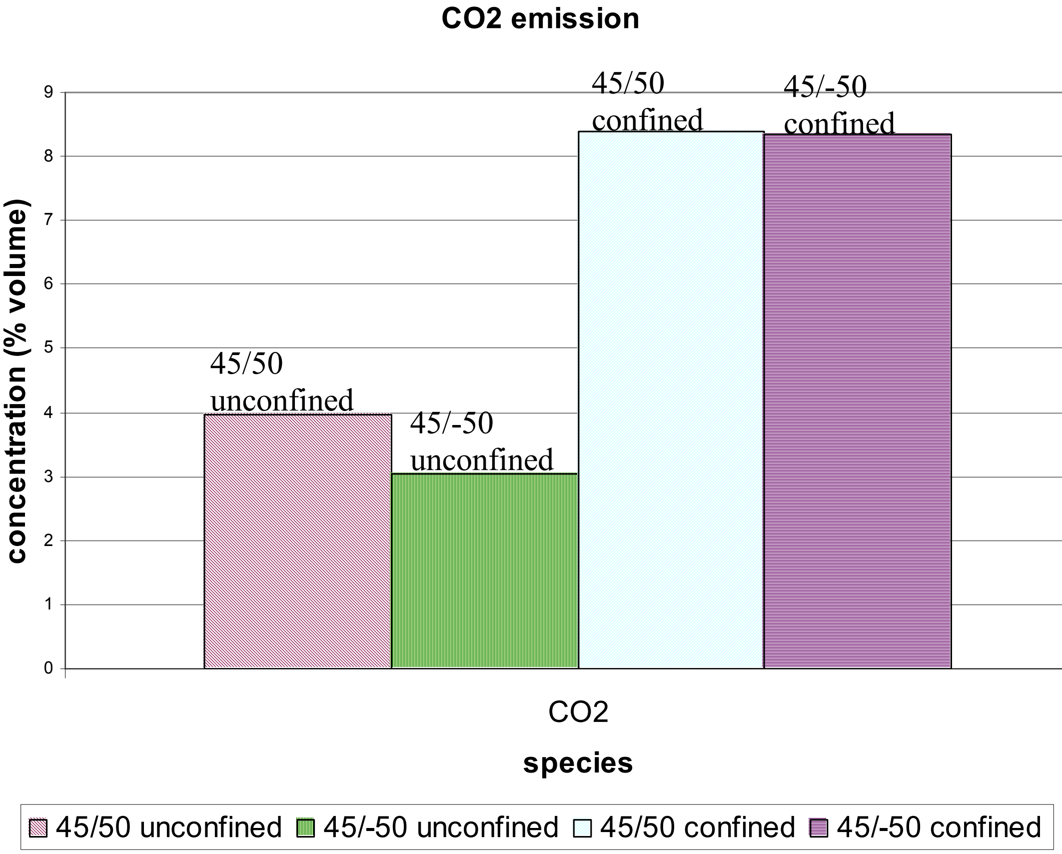

Figure 5.64 Graph of average centerline CO_2 emission for unconfined and confined flames taken at 162.5 mm downstream from the swirler exit

Chapter 6: Conclusions

A comprehensive investigation has been carried out in an experimental double concentric swirl burner on turbulent swirling flows. Flow and combustion characteristics of non-reacting and reacting swirl flowfields are characterized using a simulated Lean Direct Injection (LDI) method which consists of a central nozzle that radially injects fuel from 16 small holes into swirling combustion air. Particle image velocimetry (PIV), optical emission spectroscopy (OES), infrared (IR) thermometry, gas analysis and computer compensated micro-thermocouple measurements, were employed to determine the influences characteristics of unconfined and confined co- and counter- swirl flows with and without combustion. The data collection allowed for the following noteworthy observations to be made concerning the principle aspects of this investigation.

Unconfined Flows

- The investigated swirl distributions may not be optimal for an unconfined environment as the temperature distributions for the unconfined flames suggest the reaction region is long and stretched. This is supported by the shape of the shear strain regions with and without combustion as they frame the internal recirculation zones. A significantly stretched thermal field could lead to unstable combustion.
- The counter-swirl condition does provide more desirable characteristics in the unconfined environment. Globally the counter-swirl condition produced a

flame with shorter length. It has a smaller volume high temperature region and a more uniform thermal field. It is reasoned that the counter-swirl condition provides better mixing, seen in larger regions of shear strain, which allows for a more uniform thermal field and an increased balance of air and combustion products entrained with faster reverse flow velocity produced with the counter-swirl condition. The counter-swirl temperature profiles have a smaller difference between their overall maximum and minimum values. This is a desired trend. The small overall maximum and minimum temperature difference for the counter swirl temperature profiles, is attributed to greater mixing and smaller local eddies. The thermal time scales support this, because the integral time scales, which represent eddy size are smaller for the counter-swirl condition. The micro-time scales provide insight on fluid flow mixing, eddy speed, and thermal fluctuation and these values are lower for the counter-swirl condition.

- Flowfield data obtained with the use of particle image velocimetry supports the counter-swirl condition providing more desirable flame characteristics in the unconfined environment because of greater reverse flow velocity, larger areas of peak axial turbulence as a result of larger areas of peak negative and positive vorticity, and larger shear strain regions. These flowfield characteristics lead to larger spatial distribution of peak intensity of OH and CH radicals with high radical luminous intensity closer to the center of the flame volume with less fluctuation in radical intensity.

- The non-reacting co-swirl case has greater velocity in its jet outflow region, slower velocity decay, and higher turbulence in the shear layer region
- Combustion increases the width and length of both co- and counter- swirl internal recirculation zones and increases reverse flow velocity. Wider internal recirculation zones with greater reverse flow velocity indicate that combustion enhances swirl strength. Vorticity magnitudes increase but the widths of maximum vorticity regions decrease with combustion.

Confined Flows

- Confinement is a driving force on uniformity of flame structure. There is a more homogeneous temperature distribution in the confined environment. This homogeneity can be attributed to less fluctuation in the flowfield characteristics for confined flows such as slower jet velocity decay, increased velocity magnitudes (radial and reverse), greater velocity uniformity, increased positive radial strain, and increased turbulence.
- Confined flames have radially stretched temperature distributions. Flowfield characteristics of increased radial spreading, radial velocity, and positive radial strain support and help establish the temperature distribution.
- Confinement increases CH and OH radical intensity and spatial distribution
- Counter-swirl condition in the confined environment benefits from the increased mixing established in the unconfined environment as it promotes high radical luminous intensity closer to the center of the flame volume. Higher turbulence for the counter-swirl condition is a desired flow

characteristic. Turbulence is highly diffusive and rapid mixing is increased in the counter-swirl condition due to the increased vorticity fluctuation and smaller eddies of the counter-swirl condition

General Observation on temperature

- Close to the burner exit the temperature is not the maximum due to the formation of strong recirculation zones for all the flames. In the images maximum temperature occurs further downstream for all flames. This is consistent with swirling flow flowfields in that the reactions take place in the shear layer region and bulk fluid movement, which carries the heat, propagates downstream with only a portion entrained into the recirculation region to ignite the unburned fuel and air. The effect of swirl distribution on the temperature distribution is identified as a decrease in high temperature region volume for a counter-swirl distribution.

Chapter 7: Future Work Recommendations

From the conclusions drawn here many ideas for future work can be developed. One of the main conclusions was that the counter-swirl flowfield produced the more desirable flow, chemical, and thermal characteristics. Future work could focus on this aspect in which a comparison of several counter-swirl distributions that differ in their vane angle for the outer annulus to determine should be explored to determine if there is an optimal configuration for a set of governing parameters. Also the role of flow distributions in the two annuli on the general trends observed here should be examined and confirmed to harmonize the trends observed here. It was shown that at the swirler exit plane, the co-swirl condition imparted greater swirl. However, it was seen that at far downstream locations that the reverse flow velocity is greater for the counter-swirl condition and it would be worthwhile to examine to see if this holds at downstream locations and this effects the swirl strength calculation at downstream locations. Also future work should be done to determine the radial pressure gradients at distinct points. This would show how the pressure gradient changes with swirl distribution and flow velocity.

Also, because this work was done at atmospheric conditions it is logical that the next step would be to move to higher pressures. Many of the atmospheric and room temperature combustion phenomenon have been outlined. It would be important to see the affect of increasing pressure on the fate of these complex swirling flows. Experimenting under increased pressure conditions will move this fundamental research to more practical conditions of gas turbines used for stationaryand aero-propulsion. In keeping emphasis toward more practical conditions it could be of use to include a premixing zone in the burner geometry (to reflect a true LDI geometry) so that it better represents a practical configuration. It would be beneficial for the premixing zone to be optically accessible so that data at the swirler exit can be taken as this is critical for applying proper boundary conditions in all modeling applications. Research could also be done on determine the effectiveness of the used LDI strategy in this investigation. Also this work provided some initial data on the effects of confinement. The problems faced here to obtain 3-D PIV data under confined conditions should be explored. Additional information could be gleaned if one was to look at the effect of differing confinement sizes or exhaust openings.

One could also supplement the findings of optical emission spectroscopy, which relies on the natural chemiluminescences of the flame, with planar laser induced fluorescence (PLIF) data. This technique allows for the imaging of various planes throughout the flame. It can provide the fluorescence imaging of the NO radical along with the OH and CH radicals. PLIF data can further quantify mixing regions in the flame and when combined with PIV you can more readily overlay planar images and see direct correlation between flowfield structure and chemical structure. This can broaden our knowledge and help to clarify issues of chemical kinetics in modeling. Future research could also be enhance by the simultaneously measuring OH and CH radicals with velocity field data and/or imploring Spontaneous Raman Scattering (see Appendix D) and Coherent Anti-stokes Raman Scattering.

The above recommended experimentation will enhance our fundamental knowledge of complex swirling flows. It will also increase our database of information so that future modeling of these flows with computer codes can be validated and applied for various practical applications.

Appendix A

Appendix (List of Papers)

Archer, S, Gupta, A. K. “Swirl Effects on Global and Chemical Behavior of Flames”, 2002 IECEC Conference, Washington, DC, July 28-Aug 1, 2002

Archer, S. and Gupta, A.K. “Effect of Swirl and Combustion on Flow Dynamics in Lean Direct Injection Gas Turbine Combustion”, 41st AIAA Aerospace Sciences Meeting, Reno, NV, January 6-9, 2003, paper No. AIAA-2003-1343

Archer, S. and Gupta, A.K. “Investigation of Chemical Composition and Flow Dynamics in Swirl Stabilized Lean Direct Injection Gaseous Combustion”, 2003 IECEC Conference, Portsmouth, VA, July 29-Aug 1, 2003

Archer, S. and Gupta, A.K. “Swirl and Combustion Effects on Flow Dynamics and Lean Direct Injection Gas Turbine Combustion”, 23rd ASME Computers and Information in Engineering Conferences, Chicago, IL, September 2-6, 2003

Archer, S., and Gupta, A. K. “Effect of Swirl on Flow Dynamics in Unconfined and Confined Gaseous Fuel Flames”, 42nd AIAA Aerospace Sciences Meeting, Reno, NV, January 5-8, 2004, Paper No. 2004-0813

Archer, S. and Gupta, A.K. “The Role of Confinement on Flow Dynamics under Fuel Lean Combustion Conditions”, 2004 IECEC Conference, Providence, RI, August 16-19, 2004, Paper No. AIAA-2004-5617

Archer, S. and Gupta, A.K. “Flow Dynamics of Unconfined and Confined Swirl Stabilized Gaseous Flames”, 24th ASME Computers and Information in Engineering Conferences, Salt Lake City, UT, September 28-Oct. 2, 2004, Paper No. DETC2004-57732

Gupta, A. K., Lourenco, L., Linck, M., and Archer, S.: “A New Method to Measure Flowfield in Luminous Spray Flames”, J. Propulsion and Power, Vol. 20, No. 2, March 2004.

Archer, S. and Gupta, A.K., “Flow Dynamics of Unconfined and Confined Swirl Stabilized Gaseous Flames”, 2004 ASME Power Conference, Baltimore, MD, March 30 – April 1, 2004, Paper No. PWR2004-52079

Archer, S. and Gupta, A.K., “Flow Dynamics of Unconfined Swirling Flames under Fuel-Lean Conditions”, Submitted to J. Propulsion and Power, August 2005

Archer, S. and Gupta, A.K., “Flowfield Dynamics of Confined Flames under Fuel-Lean Conditions”, Submitted to J. Propulsion and Power, August 2005

Archer, S. and Gupta, A.K., “Confinement Effects on Flow Dynamics in Swirling Flames” 2005 ASME Power Conference, Chicago, IL, April 5-7, 2005

Appendix B

Appendix (Fuel and Air Flowrates spreadsheet). The actual code is in PC 22 under file name ‘correct.xls’

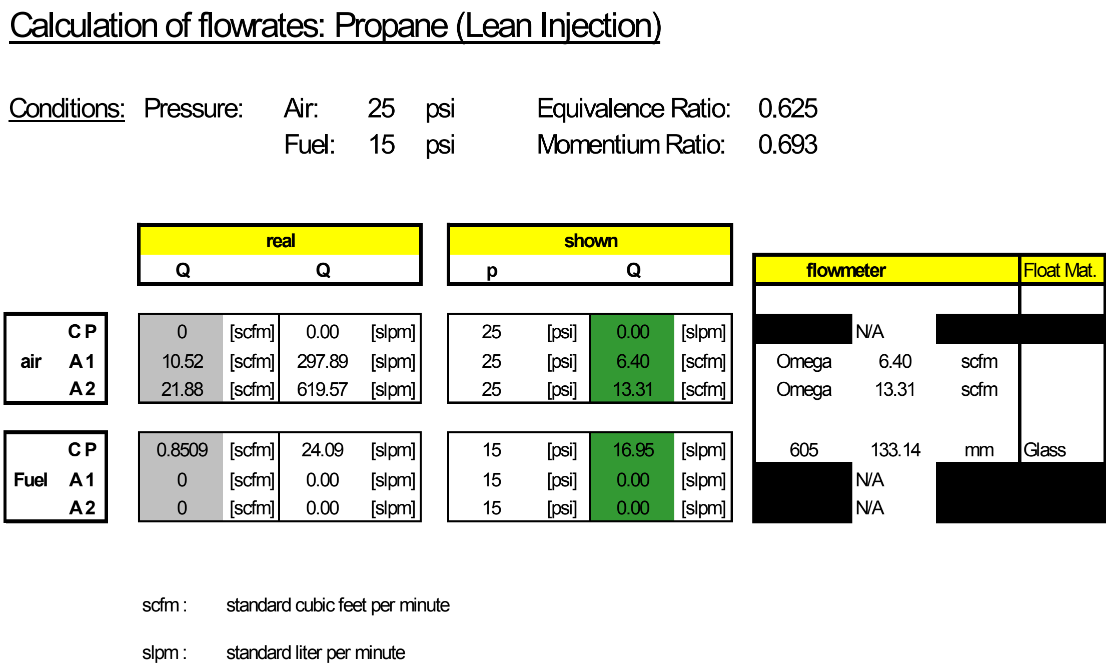

Calculation of flowrates: Propane (Lean Injection)

Conditions:	Pressure:	Air:	25	psi	Equivalence Ratio:	0.625
		Fuel:	15	psi	Momentium Ratio:	0.693

		real				shown				flowmeter			Float Mat.
		Q		Q		p		Q					
air	C P	0	[scfm]	0.00	[slpm]	25	[psi]	0.00	[slpm]		N/A		
	A 1	10.52	[scfm]	297.89	[slpm]	25	[psi]	6.40	[scfm]	Omega	6.40	scfm	
	A 2	21.88	[scfm]	619.57	[slpm]	25	[psi]	13.31	[scfm]	Omega	13.31	scfm	
Fuel	C P	0.8509	[scfm]	24.09	[slpm]	15	[psi]	16.95	[slpm]	605	133.14	mm	Glass
	A 1	0	[scfm]	0.00	[slpm]	15	[psi]	0.00	[slpm]		N/A		
	A 2	0	[scfm]	0.00	[slpm]	15	[psi]	0.00	[slpm]		N/A		

scfm : standard cubic feet per minute

slpm : standard liter per minute

Appendix C

Appendix (Data)

Radial Velocity RMS Contour Plots (non-reacting, unconfined, 3D)

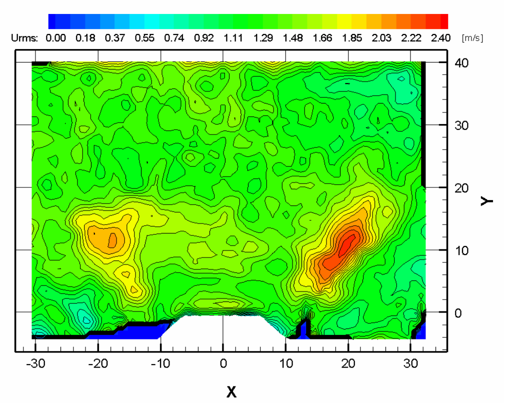

45°/ 50° co-swirl non-reacting unconfined

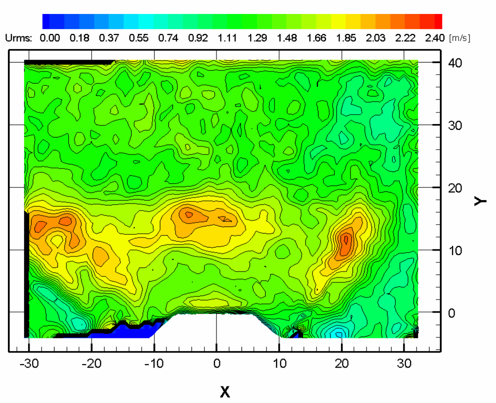

45°/ -50° counter-swirl non-reacting unconfined

Tangential Velocity RMS Contour Plots (non-reacting, unconfined, 3D)

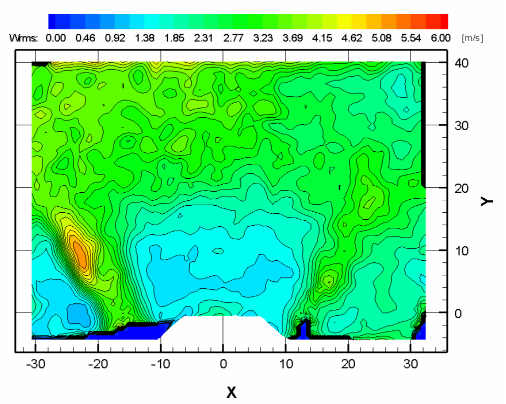

45°/ 50° co-swirl non-reacting unconfined

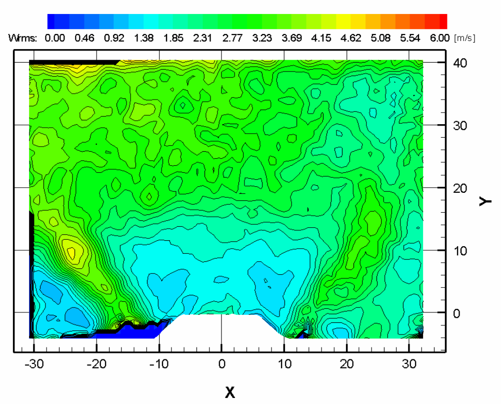

45°/ -50° counter-swirl non-reacting unconfined

Appendix D

Appendix (Implementation of Spontaneous Raman Scattering)

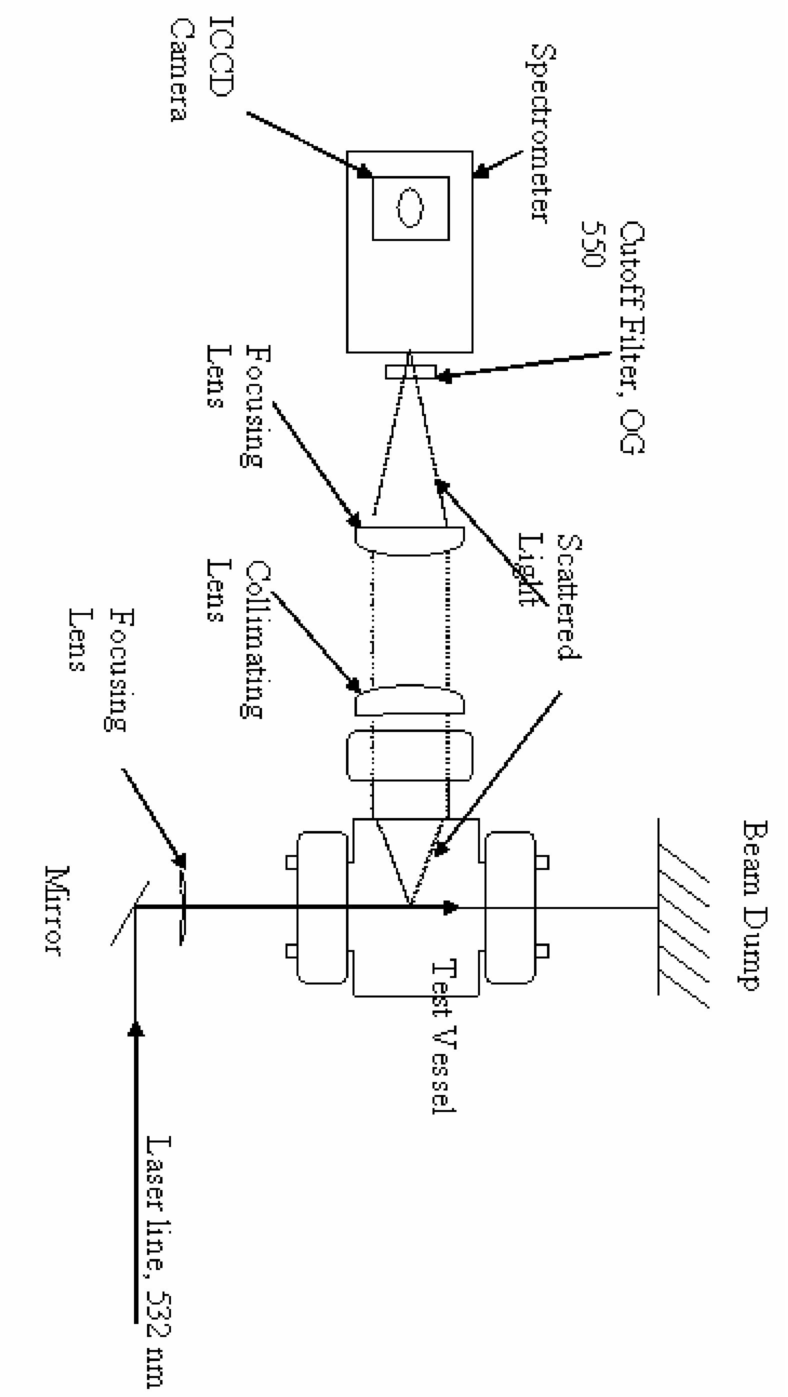

Figure D1 Basic Experimental Setup

Basic Experimental Equipment

A Continuum frequency-doubled Nd:YAG laser can be used as the excitation source. The laser can provide 532-nm light in 7-nsec pulses at a repetition rate of 10 Hz. The incident laser can be focused into the center of the vessel using a 1-inch plano-convex lens with focal length of 150 mm. The energy at the focus can start out to be approximately 100mJ/pulse.

The Raman scattered light can be collected using a four inch, f = 350 mm plano-convex lens and focused onto the spectrometer's entrance slit by a second 350 mm, four-inch lens. A 2-inch OG 550 long pass filter placed just before the entrance slit can be used to reject unwanted laser scatter; thereby reducing Rayleigh and Mie scattered light. This reduction in unwanted scattered light aids in the detection of the Raman scattered light.

The Acton Spectra-Pro 300i used should be an f/4 spectrometer with a focal length of 300 mm (already available in the Combustion Lab). Gratings are used to spectrally resolve the Raman-scattered light and focus it onto the detector. Initial measurements should start with a 600 groove/mm grating blazed a 300 nm (already equipped in the above spectrometer). Reasonable efficiency should be achieved above the gratings normal useful range of 200 to 500 nm. Other gratings to consider are a grating with 1200 groove/mm, holographic UV blaze and a 150 groove/mm grating blazed at 500 nm. The gratings can be spectrally calibrated using the emission lines of a mercury vapor lamp.

The detector is a Princeton Instruments gated and intensified CCD camera having a detector array of 384 x 576 pixels on a 0.5-inch format chip. The gate can initially be set to 50-ns with the camera synchronously triggered by the laser pulse. Princeton Instruments WinSpec software is used to control both the camera and the spectrometer grating position. The software also displays the collected spectra to the computer monitor in real-time.

Spontaneous Raman Scattering Implementation Details

When a monochromatic laser beam is incident on a volume of gas, a number of elastic and inelastic scattering processes could occur. By elastic in this context is referred to the fact that after the beam passes, the molecules as a whole have not interchanged energy with the impinging laser beam (Rayleigh Scattering). Alternately, during inelastic interaction of the laser beam with the gas molecules, energy is exchanged on a more permanent basis, and the molecules as a whole will have picked up energy or released energy as the result of the interaction (Raman Scattering).

When a laser pulse, with energy E_{laser} impinges on a volume of molecules of unknown temperature, pressure, and composition, according to Raman scattering theory, in the absence of stimulated Raman scattering, energy is inelastically scattered by the molecules. Each molecular species scatters energy at a different wavelength, dependent upon their initial and final internal ro-vibrational energy states. The intensity as well as the polarization of the Raman scattering from each molecule has an angular dependence with respect to the incident laser beam and its polarization. This angular dependency is related to the oscillating dipole that is induced in each molecule by the incident electromagnetic field. Because the strength of the induced dipole depends on the internal molecular energy field, the angular intensity distribution is different for each molecular species.

The configuration being considered for implementation calls for an angle of 90° (θ=90°) between the incident laser beam and the receiving optical axis. The polarization of the incident laser beam is perpendicular to the plane made up by the delivery and receiving optics. This maximizes the Raman scattering into the receiving optics. A polarization filter can be inserted into the receiving optics. This will improve the signal-to-noise ratio (SNR) by reducing up to half the ambient and stray light, which has commonly random polarization, while only reducing the Raman signal by a fraction. The energy collected and processed can be expressed as:

$$E_i = C(\nu_i) E_{laser} \left(\frac{\partial \sigma}{\partial \Omega} \right)_i \chi_i N \Omega l \tag{1}$$

Each of the terms of this equation is discussed below:

$C(\nu_I)$ is the wavelength dependent efficiency of the collection/dispersion/detection system. The frequency term ν_I at which the Raman signal is collected depends on the incident laser frequency and the Raman shift of the species i for the ro-vibrational transition considered. Transmission through anti-reflection coatings on collection lenses, and band rejection and notch filters, reflection from parabolic mirrors and dispersive gratings in the imaging spectrometer, and detection by means of photodiodes are all functions of wavelength and can be individually determined or calibrated as a system parameter after the full system has been assembled.

E_{laser} is the laser energy, which for the pulsed Nd:Yag laser used is typically on the order of 650 mJoule per pulse with a pulse length of 6 nsec at a wavelength of 532 nm. Pulse energy can be reduced when it becomes apparent that the high electric field density causes ionization of the nitrogen or other species present. Because not the full laser beam diameter is observed during experiments, the outer section of the Gaussian distribution has to be subtracted to obtain the observed energy.

σ_ι is the scattering cross section of species i, which depends on the angle θ, the polarization of the incident and observed scattering, and the temperature of the species. It is a concept used to describe the extent to which a molecule and an incident electromagnetic field interact. The term cross section is used as an analogy to the familiar collision cross section in molecular dynamics. Each ro-vibrational transition gives rise to a slightly different differential scattering cross section. When the temperature raises substantially, the Boltzmann population shifts to higher rotational states, affecting the overall scattering cross section. For practical purposes, the scattering cross section is considered to be a constant, which works well for the Stokes Q-branch, but can have over 5% error for the O- and S-branches. But because the differential scattering cross section for the latter two branches is much smaller then the Q-branch, the effect is neglected, although it can be observed, as will be shown in some of the spectra. Figure D2 shows how the scattering cross section changes with initial rotational state, for the three possible transitions, all three with $\Delta v=+1$ (Stokes), and for $\Delta J=0, \pm 2$. The values shown here are calculated for angle $\theta= 90°$ and for incident as well as collected light with polarization perpendicular to the plane formed by the incident and collection optics. The scattering cross sections shown are normalized with respect to the scattering cross section of the lowest rotational level. Data presented here are from analytical calculations by James and Klemperer, and Langhoff along with numerical calculations obtained from wavefunction-polarizability ellipsoid interactions. The difference between the analytical results and the numerical calculations are caused by some of the assumptions inherent in completing the analysis. Overall, analytical values and computational results are within acceptable variance from each other, at least for the scattering cross sections up to J=30. For increasing temperature, the number density distribution over the energy states will shift to the higher rotational levels. This will cause more transitions to occur at larger Raman shifts, which show up in the flame spectrum as enhanced intensity wings on the nitrogen spectrum. But because the S-branch scattering cross section decreases with increasing rotational level, while the scattering cross section for the O-branch increases, the O-branch shows intensity stronger then the S-branch. The scattering cross section for the Q-branch remains relatively unchanged with rotational level. Calculations similar to the results shown here can be made for all anglesθ, all polarization states of incidence and collected light, and for all types of allowable ro-vibrational or pure rotational transitions.

$(\partial\sigma/\partial\Omega)_\iota$ is the differential scattering cross section. The scattering cross section is strongly dependent on the angle between incident and collected light. When light is observed over a solid angle Ω, the scattering cross section will be different over the range of the solid angle, and the average value per unit of solid angle is given.

Eckbreth provides a list of values for common species with polarization states perpendicular to the incidence/collection plane, θ=90°, and for incident laser light at 532 nm. Stevenson provides a number of values for hydrocarbons with the same experimental setup but at an incident wavelength of 514 nm. These can be modified for 532 nm by using the λ^4 dependence of the scattering cross section. Even though we will not go into detail about the cause, it should be noted that the scattering cross sections of vibrationally excited molecules is larger than the differential cross sections of molecules in the ground state, similar to the difference in rotationally excited molecules. At lower temperatures, the effect of the variation in scattering cross section is limited, but at higher temperatures, these variations have to be taken into account. A possible solution is to use the intensity of the measured anti-Stokes line to determine the number densities in the first vibrationally exited level, and to use this number density to correct for the differential scattering cross section difference, if it is available for this state.

χ_i is the average species i mole fraction in the illuminated gas volume. The product of the mole fraction with the total number density N is the number of molecules of species i in the illuminated gas volume. Thus:

$$\chi_i = \frac{n_i}{N} \tag{2}$$

and

$$\sum_i \chi_i = \sum_i \frac{n_i}{N} = 1 \tag{3}$$

where all the mole fractions are accounted for.

Ω is the solid angle of observation, given in steradians. It is defined as the surface area of a unit sphere, which is subtended by a given object S. The solid angle corresponding to all of space being subtended is 4π steradians. The surface area of a full sphere is $4\pi R^2$. The surface area of an arbitrary cap of the sphere, see figure D3, is 2πRh, where the height from the bottom of the cap to the top of the cap, or sphere. If the angle α is defined as the angle between the sphere axis to the top of the sphere and the radius to the circle where the bottom of the cap intersects the sphere, the height h can be expressed as h=R-Rcosα.
The relationship between the $f^{\#}$ of an optical element and the angle α is $\tan\alpha = 1/2f^{\#}$. This gives the relationship between the $f^{\#}$, the planar angle α, and the solid angle Ω as:

$$\Omega = 4\pi\frac{Surface_{cap}}{Surface_{sphere}} = 4\pi\frac{2\pi R^2(1-\cos\alpha)}{4\pi R^2} = 2\pi(1-\cos\alpha) = 2\pi(1-\cos(\tan^{-1}(\frac{1}{2f^{\#}}))) \tag{4}$$

Thus for an $f^{\#}4$, the solid angle would be 4.85 x 10^{-2} sr. The CCD array has 384 pixels in vertical direction. With 0.022 mm size pixels, the physical dimension in vertical direction is 8.45 mm. According to Miles, the solid angle of collection and the spectrometer solid angle are connected by the equation:

$$\Omega = M^2 x \Omega_{spectr} \tag{5}$$

l is the length of the laser beam collected by the optics/spectrometer combination. With a 1:1 magnification of the optics, and a spectrometer slit size of 200 micron, l = 0.2 mm.

Temperature Measurement.

Raman thermometry is based on the ratio between the Stokes and Anti-Stokes line intensities of nitrogen. Because nitrogen is an inert species that does not participate in the chemistry, it is an ideal substance to gage the local temperature. In essence, Raman thermometry measures the number of molecules in the ground and first vibrational states, the ratio of which can directly be converted into the temperature. The total number of molecules residing in a specific rotational-vibrational energy state is given by Boltzmann as:

$$n_{i_{v,J}} = n_i \frac{g(2J+1)}{Q_i} \exp(-\frac{E_{init}}{kT}) \tag{6}$$

where n_i is the total number of the species, g is the nuclear degeneracy, which only affects homonuclear molecules, Q is the partition function of the initial distribution, E_{init} is the rotational vibrational energy of the initial state, k is Planck's constant and T the absolute temperature. Substitution of Equation (5) into Equation (1) for the Stokes and Anti-Stokes scattering, and taking the ratio of the two gives us:

$$\frac{E_{AS}}{E_S} = \frac{C(\nu_{AS})\left(\frac{\partial\sigma}{\partial\Omega}\right)_{AS} \exp\left(-\frac{E_{init,AS}}{kT}\right)}{C(\nu_S)\left(\frac{\partial\sigma}{\partial\Omega}\right)_{S} \exp\left(-\frac{E_{init,S}}{kT}\right)} = C(\nu_S,\nu_{AS})\frac{(\nu_0+\nu)^4}{(\nu_0-\nu)^4}\exp\left(\frac{E_{init,S}-E_{init,AS}}{kT}\right) \tag{7}$$

The difference between the first vibrationally exited state and the ground state is the energy hν, thus we can rewrite Equation (6) to the form:

$$T = \frac{h\nu c}{k}\left[\ln\left\{C(\nu_S,\nu_{AS})\frac{E_S}{E_{AS}}\right\} + 4\ln\left\{\frac{\nu_0+\nu}{\nu_0-\nu}\right\}\right]^{-1} \tag{8}$$

Thus the temperature can be extracted when the integrated Stokes and Anti-Stokes collected energies have been measured and when the wavelength correction parameter has been established. In previous experiments, where a known amount of nitrogen was heated in a closely controlled test vessel, measurements between 483 K and 590 K calibrated with thermocouples show that for excitation at 532 nm, the constant is:

C(607.3,473.3)=1.59 (or 1/0.63)

For the experiments to be conducted I would advise that a number of Stokes – Anti-Stokes ratios are obtained at different temperatures while the burner/rig/test vessel is heating up, while both the pressure and temperature are recorded accurately. These data will confirm the 1.59 ratio found at lower temperatures, or will suggest a different constant for the redesigned optical set-up in use.

Mole Fraction Measurements.

The number of photons of Raman scattered light at the anti-Stokes and Stokes wavelengths $S_{i,AS/S}$ from each molecular species *i* is determined from the scattered light energy $E_{i,AS/S}$ according to:

$$S_{,AS/Si} = \frac{E_{i,AS/S}}{h\nu_{i,AS/S}} = \frac{E_{laser}\left(\frac{\partial\sigma}{\partial\Omega}\right)_i \chi_i N\Omega l C\left(\nu_{i,AS/S}\right)}{h\nu_{i,AS/S}} \tag{9}$$

Each term was discussed in the introduction section. Ignoring the variation of differential scattering cross section with temperature, Equation 9 indicates that the number of scattered light photons is directly proportional to the molecular number density of the species *i*. Table I shows typical values for the commonly encountered compounds seen combustion experiments. In many references, these values will be given as relative differential scattering cross sections, where the values listed are given relative to the differential scattering cross section of nitrogen, thus where $\left(\frac{\partial\sigma}{\partial\Omega}\right)_{N_2} = 1$. These values are also given in table I.

i	Raman Shift (cm^{-1})	Stokes Wavelength (nm)	Anti-Stokes Wavelength (nm)	$\left(\frac{\partial\sigma}{\partial\Omega}\right)_{i,S}$ cm^2/sr	$\frac{\left(\frac{\partial\sigma}{\partial\Omega}\right)_{i,S}}{\left(\frac{\partial\sigma}{\partial\Omega}\right)_{N_2,S}}$
Nitrogen	2331	607.3	473.3	4.6x10^{-31}	1
Oxygen	1556	580.0	491.3	6.5x10^{-31}	1.41
Water	3652	660.3	445.5	8.94x10^{-31}	1.94
Carbon Dioxide	1285 1388	571.0 574.4	498.0 495.4	6.0x10^{-31} 4.5x10^{-30}	1.3 0.98

Methane	2914	629.6	460.0	3.37×10^{-30}	7.33
Ethane	2940	630.6	460.1	6.43×10^{-30}	13.98
Propane	2886	628.5	461.2	8.59×10^{-30}	18.67

From Equation 8 and Table 1, some preliminary calculations can be made for the signal strength. For example, the number of photons collected from nitrogen molecules in air at standard conditions ($P=1.01325\text{x}10^5$ Pa, $T=293.15$ K, $\rho=1.225$ kg/m^3) can be calculated by using the values from the table, together with:

$n_i=\chi_i N=2.13\text{x}10^{19}$ $^{\text{molecules}}/_{\text{cm}^3}$, $\Omega=(1.37)^2\text{x}4.85\text{x}10^{-2}=9.14\text{x}10^{-2}$ sr, $l=1.1$ cm,
$h=6.626\text{x}10^{-34}$Js, $E_{laser}=600$ mJ, $c=2.997 \times 10^{10}$ cm/s, C(607 nm)=0.5 (assumed)

For several different density values used in other experiments, and realizing that the relationship between the emission wavelength and photon frequency is:

$\nu=c/\lambda$ (for nitrogen this is $2.7797 \times 10^8/607 \times 10^{-9} = 4.94 \times 10^{14}$Hz)

	Mole fraction N_2	$^{\#\text{molecules}}/_{\text{cm}^3}$	# photons
Air at SPT	0.79	$2.13\text{x}10^{19}$	9.30×10^5
Nitrogen at 0.2MPa and 500K	1.00	$3.24\text{x}10^{19}$	1.41×10^6
Hencken Burner ~ 1600 F (1145 K)	0.71	$4.59\text{x}10^{18}$	2.00×10^5
Air in ASCR rig at 900 F (755 K) and 30 atm (3.0 Mpa)	0.79	$2.31\text{x}10^{20}$	1.01×10^7

Conversely, when the number of photons as well as the temperature is known, we can extract the number of molecules that scatter. When studying equation 9, it is obvious that for a given incident laser beam, the laser pulse energy is the same for all species, as well as the solid angle of observation, the length of the laser beam observed, and Planck's constant. These terms can be contracted into a single not-species-dependent constant for each experimental set-up:

$$\mathsf{C} = \frac{h}{E_{laser}\Omega l} \tag{10}$$

with which Equation 9 can be rewritten as:

$$\chi_i = \mathsf{C} N \frac{S_{i,S}\nu_{i,S}}{\left(\frac{\partial\sigma}{\partial\Omega}\right)_i C(i,\nu_i)} \tag{11}$$

and because the summation of all mole fractions should add up to 1, this becomes:

$$\chi_i = \frac{S_{i,S}\nu_{i,S}}{\sum_i \left(S_{i,S}\nu_{i,S}\right)} \frac{\sum_i \left(\left(\frac{\partial\sigma}{\partial\Omega}\right)_i C(i,\nu_i) \right)}{\left(\frac{\partial\sigma}{\partial\Omega}\right)_i C(i,\nu_i)} \tag{12}$$

Wavelength dependent collection efficiency factor ($C(i,\nu_i)$) determination

Several methods can be used to obtain the wavelength dependent collection efficiency factor. A short summary of issues that pertain to this problem will be given in this section.

Several components of the collection system can substantially influence the wavelength dependent collection efficiency, but can individually be determined, such as the band rejection-, notch-, and high-pass filters. Transmission curves for some of these items can be determined with a spectrophotometer. For some of the other components, such as lenses (coated or not), windows, gratings, mirrors, CCD array, etc., such curves are difficult to come by and other means have to be used.

Collection efficiency curves for the system as a whole can be obtained as a function of wavelength by assembling the full experimental facility and by flowing different gases through the test facility at ambient conditions. A combination of the Raman spectra of these gases obtained in a test facility and Equation 11, and comparing this with the Raman spectra obtained for nitrogen, will give the collection efficiency at the wavelength of that species as compared to the collection efficiency of nitrogen at the Stokes wavelength. Assuming that the collection efficiency at the nitrogen Stokes wavelength equals unity, this can be formalized by the collection efficiency factor:

$$C(i,\nu_i) = \frac{\left(\frac{\partial\sigma}{\partial\Omega}\right)_{N_2} S_{i,S}\nu_{i,S}\chi_{N_2}}{\left(\frac{\partial\sigma}{\partial\Omega}\right)_i S_{N_2,S}\nu_{N_2,S}\chi_i} \tag{13}$$

The values for the differential scattering cross sections and Raman wavelengths can be found in Table I. The ratio of integrated intensities measured is entered as the S-ratio. Any species can be entered in the facility as the only species at ambient pressure and temperature (χ_i=1) and compared with the spectrum of nitrogen in the air (χ_{N_2}=0.79). Alternately, a mixture of known mole fractions of the species with nitrogen can be entered. As an example, take data, obtained of 295 K, 300 psi air in an experimental rig. The oxygen and nitrogen lines are well defined. The area ratio of oxygen-to-nitrogen is:

$$\frac{S_{O_2}}{S_{N_2}} = 0.5178; \qquad \frac{\chi_{N_2}}{\chi_{O_2}} = \frac{0.79}{0.21} = 3.7619; \qquad \frac{\left(\frac{\partial \sigma}{\partial \Omega}\right)_{O_2,S}}{\left(\frac{\partial \sigma}{\partial \Omega}\right)_{N_2,S}} = 1.41;$$

$$\frac{\nu_{O_2}}{\nu_{N_2}} = \frac{\lambda_{N_2}}{\lambda_{O_2}} = 1.0471.$$

Thus C(O_2,580.0)=1.319.

This method of determining the collection efficiency is convenient on the Stokes side of the laser line.

For the anti-Stokes lines, alternate methods could be employed because the differential scattering cross sections are typically not known. An example of the determination of the collection efficiency at the anti-Stokes line of nitrogen is given by the following. Data was obtained with 28 psia inside a vessel, which could be heated up to 590 K with thermocouple readout of the bulk temperature. The resulting nitrogen Stokes-to-AntiStokes intensity ratios were plotted against the measured thermocouple temperatures. At the same time, the theoretical intensity ratio versus temperature curve was plotted in the same figure. By correcting the measured Stokes-to-AntiStokes intensity ratio, the Raman measured data points were made to coincide with the theoretical curve. This occurred at a correction (read efficiency factor) of 1.587 for the conditions occurring in this setup. The calibration curve is shown in Figure D4.

Other efficiency factors on the Anti-Stokes side can be determined similarly by heating a gas under known conditions, and calculating the theoretical curve. This is relatively straightforward for diatomic molecules, but becomes more complex for polyatomic species. At the same time, it is not necessary to know more then the nitrogen Anti-Stokes collection efficiency factor, because that value is used for thermometry, and other species are not required.

Appendix References

1. James, T. C., and Klemperer, W., "Line Intensities in the Raman Effect of Σ Diatomic Molecules," Journal of Chemical Physics, Vol. 31, No. 1, 1959, pp. 130-134.
2. Langhoff, S. R., and Davidson, E. R., "Configuration interaction calculations on the nitrogen molecule," Int. J. Quantum Chem. Vol. 8, No. 1 1974, pp. 61-72.
3. Miles, Paul C., "Raman line imaging for spatially and temporally resolved mole fraction measurements in internal combustion engines." Applied Optics, Vol. 38, No. 9,1999, pp 1714-1732.

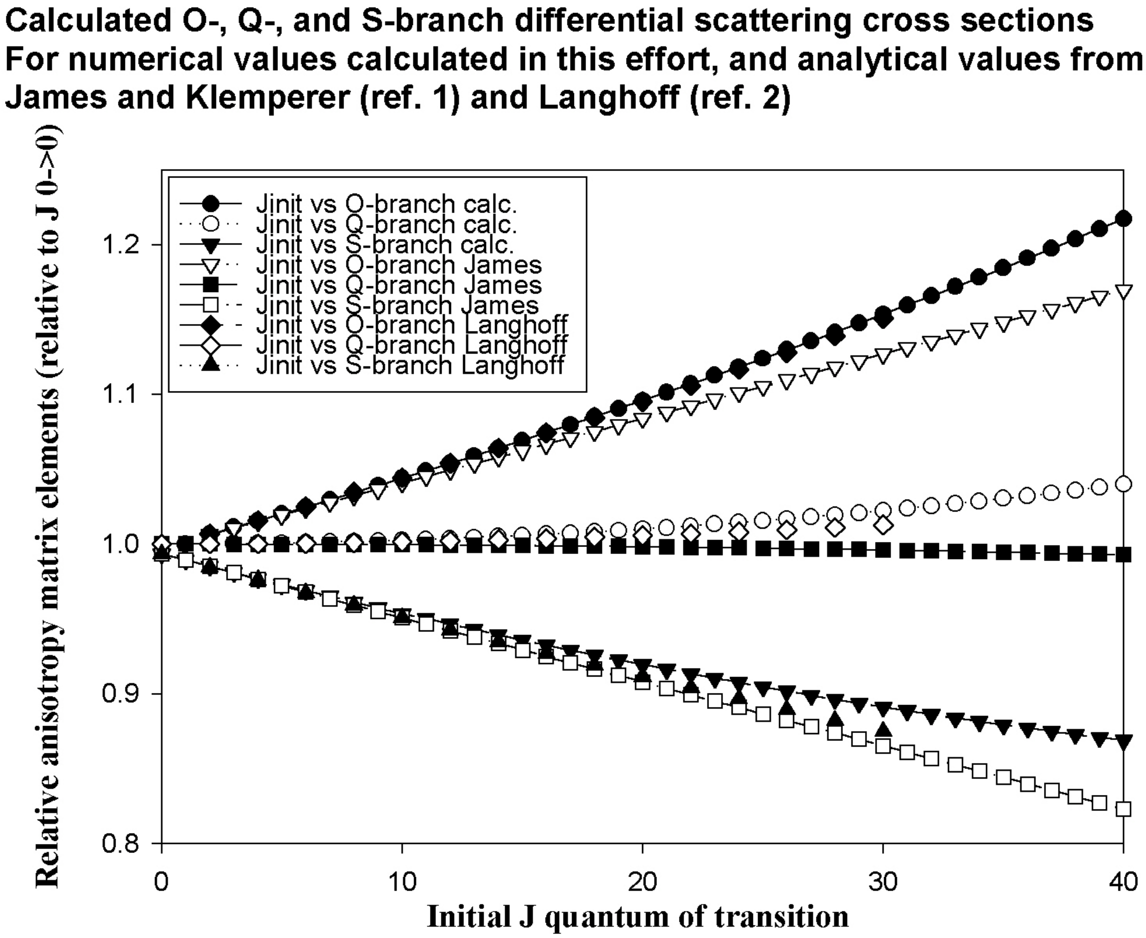

Figure D2 Dependency of parts of the scattering cross section on the rotational state of the molecules.

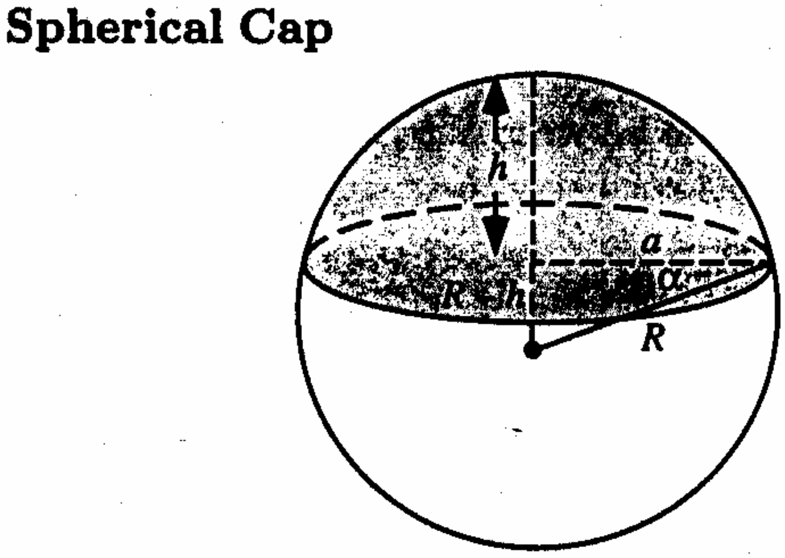

Figure D3 Definition of dimensions of a sphere utilized for solid angle determination.

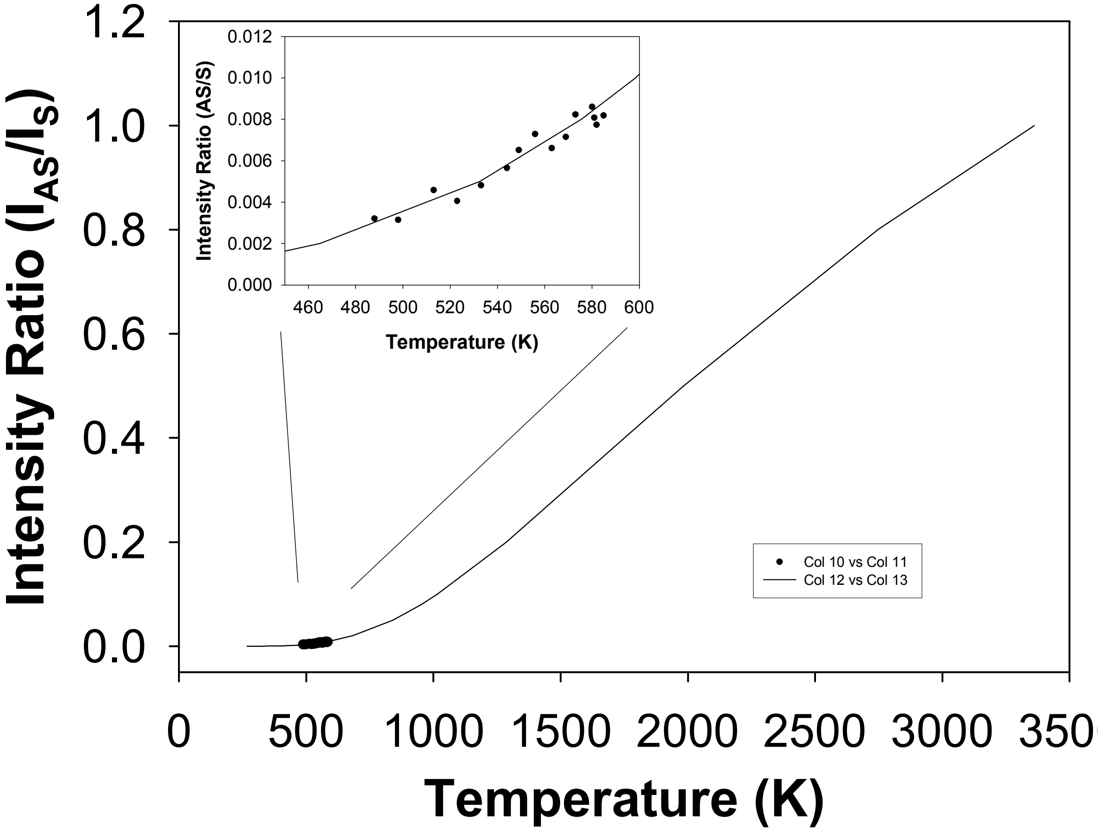

Figure D4 Results of nitrogen Stokes/Anti-Stokes measurements as a function of temperature compared to computational relationship.

References

[1] Wark K. and Warnger C. F., “Air Pollution: Its Origin and Control”, HarperCollins Publishers, New York, p. 372, 1981.

[2] http://www.personal.psu.edu/faculty/c/x/cxm283/research/GTI_Instability.htm, 2004

[3] Wark K. and Warnger C. F., “Air Pollution: Its Origin and Control”, HarperCollins Publishers, New York, p. 456-459, 1981.

[4] Davis, L. B. and Washam, R. M., “Development of a Dry Low NOx Combustor,” ASME Paper No. 89-GT-255, 1989.

[5] Sattelmayer, T. H., Felchlin, M. P., Haumann, J., Hellat, J. and Styner, D., “Second-Generation Low-Emission Combustors for ABB Gas Turbines: Burner Development Tests at Atmospheric Pressure,” ASME Paper No. 90-GT-162, 1990.

[6] Røkke, P.E., Hustad, J.E., Røkke, N.A., and Svendsgaard, O.B., “Technology Update on Gas Turbine Dual Fuel, Dry Low Emission Combustion Systems”, Proceedings of ASME Turbo Expo 2003, Atlanta, GA, ASME GT-2003-38112, June 16-19, 2003.

[7] Nickolaus, D.A., Crocker, D.S., Black, D.L., and Smith, C.E., “Development of a Lean Direct Fuel Injector for Low Emission Aero Gas Turbines”, GT-2002-30409, 2002.

[8] Gupta A.K., Lilley D.G. and Syred N., “Swirl Flows”, Abacus Press, Tunbridge Wells, England, 1984.

[9] Lefebvre, A. W., “Gas Turbine Combustion”, Hemisphere Publishing Corporation, New York, pp.126-135, 1983.

[10] Mellor, A.M., “Gas Turbine Engine Pollution”, Progress in Energy and Combustion Science, Vol. 1, pp. 111-133, 1976.

[11] Lilley, D. G., “Swirl Flows in Combustion: A Review,” AIAA Journal, Vol 15, No. 8, pp. 1063-1078, 1977

[12] Marshall A.W., “Effects of Jet Momentum Distribution Combustion Characteristics in Co-Swirling Flames”, Ph.D.-thesis, University of Maryland, College Park, MD, 1996.

[13] Chigier, N. A., “Gas Dynamics of Swirling Flow in combustion Systems,” Astronautica Acta, Vol 17, pp. 387-395, 1972.

[14] Syred, N. and Beer, J., “Combustion in Swirling Flows: A Review,” Combustion and Flame, vol. 23, pp. 143-201, 1974.

[15] McVey, J.B., Padget, F.C., Rosfjord, T.J., Hu, A.S., Peracchio, A.A., Schlein, B., and Tegel, D.R., “Evaluation of Low- NOx Combustor Concepts for Aeroderivative Gas Turbine Engines”, J. Engineering for Gas turbines and Power, 115, 581-587, 1993.

[16] Snyder, T.S., Rosfjord, T.J., McVey, J.B., and Chiappetta, L.M., “Comparison of Liquid Fuel/Air Mixing and NOx Emissions for a Tangential Entry Nozzle”, ASME, International Gas Turbine and Aeroengine Congress, 94-GT-283, 1994.

[17] Stephens, J.R., Acharya, S., and Gutmark, E.J., “Controlled Swirl-Stabilized Spray Combustor”, AIAA Paper 97-0464, 1997.

[18] Syred, N., Chigier, N., and Beer, J. M., Proceedings of the Combustion Institute, Vol. 13, pp. 617, 1971.

[19] Hall, M. G., “Vortex Breakdown”, Annual Review of Fluid Mechanics, vol. 4, pp. 195-218, 1972.

[20] Chaturvedi, M. C., “Flow Characteristics of Axi-Symmetric Expansion”, ASCE Proceedings of the Hydraulics Division, vol. 89, pp. 61-92, 1963.

[21] Schmidt, S. E. and Hedman, P. O., “CARS Temperature and LDA Velocity Measurements in a Turbulent Swirling Premixed Propane/Air Fueled Model Gas Turbine Combustor”, ASME 95-GT-64, 1995.

[22] Ahmed, S. A., “Velocity Measurements and Turbulence Statistics of a Confined Isothermal Swirling Flow”, Experimental Thermal and Fluid Science, vol. 17, pp. 256-264, 1998.

[23] Aroussi, A., Kucukgokoglan, S., Menacer, M., Pickering, S.J., “PIV Measurements of Swirling Flows From Two Adjacent Burners”, 9th International Symposium on Flow Visualization, Heriot-Watt University, Edinburgh, Scotland 2000.

[24] Nie, J.X., Yeboah, Y.D., Bota, K.B., and Bai, T., “Laser Doppler Velocimetry and Particle Image Velocimetry Measurements of Premixed Methane-Air Flames and their comparisons”, 3RD ASME/JSME Joint Engineering Conference, San Francisco, CA, USA, 1999.

[25] Yeboah, Y.D., Nie, J.X., Bota, K.B., Bai, T., and Ross, H.D., “Particle Image Velocimetry Measurements of Premixed Methane-Air Flames,” The Proceedings of 1998 ASME Fluids Engineering Division Summer Meeting, Washington, DC, FEDSM98-5267, 1-25, 1998.

[26] Yeboah, Y.D., Nie, J.X., Bota, K.B., Bai, T., and Ross, H.D., “Particle Image Velocimetry Measurements of Premixed Methane-Air Flames and its Numerical Modeling,” 1998 AIChE Annual Meeting, Miami, FL, Paper 230-e, 15-20, 1998.

[27] Driscoll, J.F., Sutkus, D.J., Roberts, W.L., Post, M.E., and Goss, L.P., “The Strain Exerted by a Vortex on a Flame Determined from Velocity Field Images”, Combustion Science and Tech., Vol 96, pp.213-229, 1994.

[28] Mungal, M.G., Lourenco, L.M., and Krothapalli, A., “Instantaneous Velocity Measurements in Laminar and Turbulent Premixed Flames Using On-Line PIV”, Combustion Science and Tech., Vol 106, pp. 239, 1995.

[29] Gupta, A. K., Lourenco, L., Linck, M., and Archer, S.: “A New Method to Measure Flowfield in Luminous Spray Flames”, J. Propulsion and Power, Vol. 20, No. 2, March 2004.

[30] IDT, proVISION^{TM,} software release 2.01, Particle Image Velocimetry User Manual, Tallahassee, FL, August 2002.

[31] Archer, S., and Gupta, A. K.: Effect of Swirl on Flow Dynamics in Unconfined and Confined Gaseous Fuel Flames, 42nd AIAA Aerospace Sciences Meeting, Reno, NV, January 5-8, 2004, Paper No. 2004-0813.

[32] Archer, S., and Gupta, A. K.: The Role of Confinement on Flow Dynamics under Fuel Lean Combustion Conditions, IECEC Conference, Providence, RI, August 16-19, 2004.

[33] Archer, S. and Gupta, A. K.: Effect of Swirl and Combustion on Flow Dynamics in Lean Direct Injection Gas Turbine Combustion, 41st AIAA Aerospace Sciences Meeting, Reno, NV, January 6-9, 2003, Paper No. AIAA-2003-1343.

[34] Archer, S. and Gupta, A. K.: Flow and Chemical Behavior of Swirl Stabilized Lean Direct Injection Gaseous Flames, IECEC Conference, Portsmouth, VA, August 17-21, 2003.

[35] Gautam, V. and Gupta, A. K.: Spectroscopic Analysis of Fuel Lean Flames for Propulsion Applications, ASME Power Conference 2004, Baltimore, Maryland, PWR 2004-52074.

[36] Dasch, C. J., "One-dimensional tomography: a comparison of Abel, onion-peeling, and filtered back projection methods", Applied Optics, Vol. 31, pp. 1146, 1992.

[37] Ishiguro, T., Tsuge, S., Furuhata, T., Kitagawa, K. Arai, N., Hasegawa, T., Tanaka, R. and Gupta, A. K.: Homogenization and Stabilization During Combustion of Hydrocarbons with Preheated Air, Proc. 27th Symposium (Intl.) on Combustion, The Combustion Institute, Pittsburgh, PA, 1998, pp. 3205-3213.

[38] Konishi, N., Kitagawa, K., Arai, N. and Gupta, A. K.: Two-Dimensional Spectroscopic Analysis of Spontaneous Emission from a Flame using Highly Preheated Air Combustion, J. Propulsion and Power, Vol. 18, No. 1, January-February, 2002, pp. 199-204.

[39] Kitagawa, K., Shinoda, S., Arai, N., Ishiguro, T., Tsuge, S., Hasegawa, T. and Tanaka, R.: Spectroscopic Observation of Homogenization and Stabilization during Combustion of Hydrocarbons with Pre-Heated Air, Proc. 1st Asia-Pacific Conference on Combustion, Osaka, Japan, 1997, pp. 461-465.

[40] Ishiguro, T., Tsuge, S., Furuhata, T., Kitagawa, K. Arai, N., Hasegawa, T., Tanaka, R. and Gupta, A. K.: Homogenization and Stabilization During Combustion of Hydrocarbons with Preheated Air, Proc. 27th Symposium (Intl.) on Combustion, The Combustion Institute, Pittsburgh, PA, 1998, pp. 3205-3213.

[41] Kunugi M. and Jino H., "Measurements of Fluctuating Flame Temperature", Seventh international Symposium on Combustion, Butterworths, pp. 942-47, 1959.

[42] Gupta, A. K., Beer, J. M., and Swithenbank, J., "Concentric Multi-Annular Swirl Burners: Stability limits and Emission Characteristics", Sixteenth Symposium (International) on Combustion, The Combustion Institute, pp.79-86, 1976.

[43] Heitor, M.V., Taylor, A.M.K.P., and Whitelaw, J.H., "Simultaneous Velocity and Temperature Measurement in a Premixed Flame", Experiments in Fluids, Vol. 3, pp. 323-329, 1985.

[44] Miles, P.C. and Gouldin, F.C., "Determination of the Time Constant of Fine-Wire Thermocouple for Compensated Temperature Measurements in Premixed Turbulent Flames", Combustion Science and Technology, vol. 89, pp. 181-199, 1993.

[45] Ballantyne, A. and Moss J. B., "Fine Wire Thermocouple Measurements of Fluctuation Temperatures", Combustion Science and Technology, Vol. 17, pp. 63-72, 1977.

[46] Archer S.S., "Radial Distribution of Swirl Effects in a Burner on Combustion Characteristics of Premixed Flames", M.S. thesis, University of Maryland, College Park, MD, 2001.

[47] Ramavajjala M.S., "Burner Geometry Effects on the Emissions of a Variable Geometry Swirl Combustor", M.S. thesis, University of Maryland, College Park, MD, 1990.

[48] Raffel, M., Willert, C. E., and Kompenhans, J., "Particle Image Velocimetry", Springer, Berlin, 1998.

[49] Mckenna, S. P. and Mcgillis, W. R., "Performance of Digital Image Velocimetry Processing Techniques", Experiments in Fluids, Vol. 32, pp 106-115, 2002.

[50] Sung, C. J., Kistler, J. S., Nishioka, M., and Law, C. K., Combustion and Flame, Vol. 105, pp. 189 – 200, 1996.

[51] Kuo, K. K., "Principles of Combustion", John Wiley and Sons, New York, 1986.

[52] Gaydon, A.G., "The Spectroscopy of Flames", John Wiley and Sons, New York, pp. 1-9, 159-163, 1974.

[53] Princeton Instruments, Manual Version 2, Revision A, ICCD Detector Operation Manual, July 18 1994.

[54] http://www.flirthermography.com/media/SC3000%20Datasheet.pdf